TESTING ACCURACY AND CONVERGENCE OF GPUSPH FOR FREE-SURFACE FLOWS

A Thesis

by

ERIN ANN ROONEY

Submitted to the Office of Graduate Studies of
Texas A&M University
in partial fulfillment of the requirements for the degree of

MASTER OF SCIENCE

August 2011

Major Subject: Civil Engineering

Testing Accuracy and Convergence of GPUSPH for Free-Surface Flows

TESTING ACCURACY AND CONVERGENCE OF GPUSPH FOR FREE-SURFACE FLOWS

A Thesis

by

ERIN ANN ROONEY

Submitted to the Office of Graduate Studies of
Texas A&M University
in partial fulfillment of the requirements for the degree of

MASTER OF SCIENCE

Approved by:

Chair of Committee,	Jennifer L. Irish
Committee Members,	Robert Weiss
	Hamn-Ching Chen
Head of Department,	John Niedzwecki

August 2011

Major Subject: Civil Engineering

ABSTRACT

Testing Accuracy and Convergence of GPUSPH for Free-Surface Flows.

(August 2011)

Erin Ann Rooney, B.S., Virginia Polytechnic Institute and State University

Chair of Advisory Committee: Dr. Jennifer L. Irish

The effect of vegetation on the dissipation of waves is important in understanding the vegetation's role in protecting coastal communities during extreme events such as hurricanes and tsunamis. Numerical modeling makes it possible to study the flow through vegetation fields, but it is important to understand the flow dynamics around one piece of vegetation and validate the numerical model used, before the dynamics of an entire vegetated patch can be modeled and understood. This project validated GPUSPH, a Lagrangian mesh-free numerical model, by determining the optimal characteristics to obtain accurate simulations for flow through a flume with and without an obstruction.

The validation of GPUSPH and determination of optimal characteristics was accomplished by varying model particle spacing, sub-particle scale (SPS) turbulence inclusion in the conservation of momentum equation, and kernel weighting function for two test cases. The model particle spacing sets the initial distance between the moving grid points, known as particles, in the system. The SPS turbulence term is intended to account for turbulence generated at the sub-particle scale between the particles. The

kernel weighting functions used are the quadratic kernel and the cubic spline kernel. These kernels determine how much influence surrounding particles have on the flow characteristics of an individual particle.

The numerical results of these tests were compared with experimental results to obtain conclusions about the accuracy of these simulations. Based on comparisons with experimental velocities and forces, the optimal particle spacing was found to occur when the number of particles was in the high 100,000s for single precision calculations, or mid-range capabilities, for the hardware used in this project. The sub-particle scale turbulence term was only necessary when there was large-scale turbulence in the system and created less accurate results when there was no large-scale turbulence present. There was no definitive conclusion regarding the best kernel weighting function because neither kernel had overall more accurate results than the other. Based on these conclusions, GPUSPH was shown to be a viable option for modeling free-surface flows for certain conditions concerning the particle spacing and the inclusion of the sub-particle scale turbulence term.

ACKNOWLEDGEMENTS

First, I would like to thank my committee chair, Dr. Jennifer L. Irish, for providing the support and guidance that has taught me to become a better researcher and engineer over the past two years. Her dedication to helping her students improve in all aspects of research including writing, presenting, and analyzing technical problems, does not go unnoticed and is greatly appreciated. I would also like to thank my committee member, Dr. Robert Weiss, for his time, guidance, and blunt honesty that greatly improved the quality of this project. His knowledge of GPUSPH has been an invaluable asset to this research. Additionally, I must thank Dr. Hamn-Ching Chen for serving on my committee, reviewing my research, and providing constructive insights.

I am also grateful to Andrew Muñoz for teaching me the basics of GPUSPH and assisting me with installation and software issues. Thanks also go to my fellow graduate students and friends that have been a constant support system and have made these past two years an eventful and enjoyable experience.

Finally and most importantly, I need to thank my parents, Daniel and Ann Rooney, and the rest of my family for their never-ending support and dedication to providing me with the best education and opportunities to help me grow as a person and as an engineer. I would be nowhere without their love and encouragement throughout the years.

NOMENCLATURE

B	Coefficient in Pressure Equation
c_0	Speed of Sound at Reference Density
C_s	Smagorinsky Constant, 0.12
C_t	Constant, 6.6×10^{-3}
Cg	C For Graphics
CPU	Central Processing Units
CUDA	Compute Unified Device Architecture
D	Boundary Force Coefficient
f_{aj}	Boundary Force of Particle j Exerted on Fluid Particle a
$f(x)$	Value of a Quantity, Such As Density
f_j	Value of a Quantity at Point j
g	Gravitational Acceleration
g_i	i Component of Gravitational Acceleration Vector
GPU	Graphical Processing Units
GPUSPH	Smoothed Particle Hydrodynamics model implemented on GPU
h	Smoothing Length
h_B	Smoothing Length For Boundary Particles
h_F	Smoothing Length For Fluid Particles

h_{BF}	Average Smoothing Length For Boundary and Fluid Particles
H	Characteristic Water Depth
k	SPS Turbulent Kinetic Energy
K	MK Boundary Force Coefficient
LJ	Lennard-Jones Boundary Force Calculation
m_b	Mass of Particle b
MK	Monaghan-Kajtar Boundary Force Calculation
OpenGL	Open Graphics Library
p	Pressure
$p1$	Coefficient, 12
$p2$	Coefficient, 6
q	Ratio of Radial Distance to Smoothing Length
r	Radial Distance
r_0	Initial Particle Spacing
RMS	Root-Mean-Square
S_{ij}	SPS Strain Tensor
SPH	Smoothed Particle Hydrodynamics
SPS	Sub-Particle Scale
t	Time
u	Velocity Vector
u_i	i Component of Velocity Vector

u_{ab}	Velocity Vector from Particle a to Particle b
u_b	Boundary Layer Velocity
v_e	Experimental Value
v_f	Overall Flow Velocity
v_n	Numerical Value
V_j	Volume of Particle at Point j
V_n	Normalized Velocity
$W(x - x_j)$	Weighting Function
W_{ab}	Weighting Function on Particle a from Particle b
x_j	j Component of Location Vector
α_D	Weighting Function Coefficient
β	Ratio of Boundary Particle Spacing to Fluid Particle Spacing
Δl	Particle Spacing
ε	Correction Factor, 0.5
Θ	Diffusion Term
κ	Scaling Factor
μ	Viscosity
ν_t	Turbulent Eddy Viscosity
ρ	Density
ρ_o	Reference Density, 1000 kg m^{-3}

τ_{ij}	Stress Tensor
υ_0	Kinetic Viscosity of Laminar Flow

TABLE OF CONTENTS

Page

LIST OF FIGURES

Page

Page

Page

Page

LIST OF TABLES

Page

Page

Page

1. INTRODUCTION

1.1 Importance of Fluid Flow Modeling

Fluid flows at extreme and small scales have influenced people for millennia, causing flooding due to hurricanes, erosion due to high velocity flows, and changes due to many other events. Scientists and engineers need to understand the mechanics of these flows to determine the causes of these types of events and help communities prepare for the implications from these events. This statement is especially true for coastal communities that often deal with surges and flooding due to extreme events such as hurricanes and tsunamis. There are many factors that affect water levels due to these extreme events including wind fields, land elevation, and natural and manmade coastal protection systems.

One example of a protection system is coastal vegetation that may affect the speed and height of the water flowing landward from the open ocean. Turbulent flows in these vegetation patches are not fully understood and hard to fully analyze with experimental data alone. Numerical models are used to better understand these fluid flow structures, but most of the models currently in use have some type of structured grid that calculates properties from a Eulerian viewpoint with an explicit time step.

This thesis follows the style of the *Journal of Geophysical Research.*

These models may be required to use an unnecessarily small explicit time step to avoid unbounded errors. Instead, an implicit time step calculation allows the model to use larger time steps, producing numerical results faster than if using the explicit time step. This project uses a Lagrangian mesh-free method with an implicit time step called Smoothed Particle Hydrodynamics (SPH) in the numerical model GPUSPH.

1.2 GPUSPH

Based on the Navier-Stokes equations, GPUSPH calculates quantities of the flow using moving grid points, called particles. The quantities are smoothed at each time step based on a kernel weighting function to produce characteristics of the flow including velocity, density, and pressure. The equations and approach of the GPUSPH model will be discussed in depth in Section 2.

1.3 Problem Approach

Before using GPUSPH to study the problem of turbulence in a vegetation field, the model must be tested to ensure that it correctly models the sub-components of this flow. This project will attempt to validate GPUSPH for fluid flow through a flume and around an obstruction by comparing numerical results to experimental results for certain aspects of the flow. A main topic of this project is to understand the changes in numerical output due to differences in initial placement of the particles in the system and various options in calculating the movement of the flow. It is important to understand these changes to know how to best initiate the model and obtain accurate results.

These goals will be accomplished by studying two cases of dam break flow, one case with an obstruction and one case without an obstruction. To study the differences due to various initial setups, the spacing between the particles, the weighting kernel function, and the viscous calculation technique was varied as will be explained in Section 3. The outputs of these cases were compared to experimental data to quantify the influence of these factors.

1.4 Hypothesis

The test cases will be varied in the particle spacings used in the model, the inclusion of a sub-particle scale (SPS) turbulence term, and the weighting kernel function used. Initial assumptions with regard to particle spacing are that smaller particle spacings will produce more accurate results because there will be more particles, which are actually moving grid points, to better fill the system and simulate the flow characteristics. This assumption is expected to be complicated by the single precision capabilities of the hardware used for this project if the particle spacings become too small. Previous literature has shown that computing precision can have an impact on the accuracy of numerical results [*McCarn,* 1992].

The cases that include the SPS turbulence term are expected to be more accurate than the cases without the term because the term is expected to more accurately calculate the turbulence created between the measurable particle spacings by spatially averaging over the sub-particle scale. Averaging over the sub-particle scale provides a closure scheme to more accurately model the smaller-scale turbulence that cannot be resolved by

the particle spacing [*Dalrymple and Rogers,* 2006]. The influence of particle spacing on the SPS turbulence term raises the expectation that the term will have a larger effect on cases with greater particle spacings as compared to cases with smaller particle spacings.

The kernel functions used in the weighting function, the quadratic kernel and the cubic spline kernel, are two formulations used to calculate the presumed same quantities. It is expected that the weighting function should have little effect on the overall results.

1.5 Thesis Content

The format of this thesis includes five sections used to explain and analyze the problem. The first section provides the motivation for the project and an overview of the model and approach. The second section provides a literature review of the SPH field and includes information on the GPUSPH model and its fundamental equations. The third section explains the test cases and the methods used to calculate quantities from the model output, while the fourth section displays and analyzes the results. The final section provides a summary of the conclusions based on this research and suggestions for continuation of these studies.

2. BACKGROUND AND LITERATURE REVIEW

2.1 Introduction

Fluid flow affects many aspects of everyday life, including river flooding, hurricane surge and bridge scour. For centuries, scientists have been trying to analyze and predict flow and its effects through experimental tests and/or simulations. While fluid flow is a complex process that is dependent on many variables, physics-based numerical models are often used to simulate this complexity and attempt to calculate characteristics of the flow. The numerical models are used to create or reproduce simulations of real-world problems at large or small scales and collect simulated data for analysis.

One area of fluid flow research that can be improved through better modeling techniques is the effect of coastal vegetation on the dissipation of incoming waves or currents. Knowing the effects of vegetation provides more accuracy in predicting surge and flooding in coastal communities and habitats during intense events such as hurricanes and tsunamis. Most numerical models currently use some type of structured grid and Eulerian viewpoint such as in Large Eddy Simulation models [*Stoesser et al.*, 2009], but there is an ever present need to improve the techniques used to calculate accurate results. GPUSPH, the model in this study, uses a Lagrangian mesh-free method to study the flow characteristics. The main advantages of this approach are that it allows for a complex geometry and it distributes the moving grid points in relation to the

distribution of mass in the system. These two characteristics of the model produce useful and accurate results.

This subsection provides an overview of the need to refine numerical simulations. Subsection 2.2 presents the fundamental equations of fluid mechanics. Subsection 2.3 then explains the formulation of the Smoothed Particle Hydrodynamics (SPH) model and discusses aspects of the model including weighting functions, viscosity calculations, and issues affecting the boundaries and free-surface. Subsection 2.4 discusses how the SPH model is used on graphical processing units (GPU) to allow higher resolution runs in a reasonable timeframe through the GPUSPH model. Finally, a brief summary of the literature review will be provided in Subsection 2.5.

2.2 Fluid Mechanics

The SPH method is derived from the basic equations of fluid motion including the continuity equation and the conservation of momentum. The continuity equation states that:

$$\frac{\partial \rho}{\partial t} + \nabla \cdot \left(\rho \vec{u} \right) = 0 \tag{2.1}$$

where:

ρ is density

t is time

u is velocity

as discussed by Kundu and Cohen [*Kundu and Cohen*, 2008].

The conservation of momentum shows that:

$$\rho \frac{Du_i}{Dt} = \rho g_i + \frac{\partial \tau_{ij}}{\partial x_j} \tag{2.2}$$

where:

u_i is the i component of the velocity vector

g_i is the i component of the gravitational acceleration vector

τ_{ij} is the stress tensor

x_j is the j component of the location vector

also stated in Kundu and Cohen [*Kundu and Cohen*, 2008].

Additionally, the SPH method depends on the Navier-Stokes equation, the equation of motion for a Newtonian fluid. The Navier-Stokes equation is:

$$\rho \frac{Du_i}{Dt} = -\frac{\partial p}{\partial x_i} + \rho g_i + \frac{\partial}{\partial x_j}\left[2\mu e_{ij} - \frac{2}{3}\mu(\nabla \cdot \vec{u})\delta_{ij}\right] \tag{2.3}$$

where:

p is the pressure

μ is the viscosity

[*Kundu and Cohen*, 2008].

These fundamental fluid equations were converted into the SPH method equations that will be discussed in the next subsection.

2.3 Smoothed Particle Hydrodynamics

SPH is a Lagrangian mesh-free model developed initially for astrophysical uses in the 1970's [*Gingold and Monaghan*, 1977] and later applied to free-surface flows by Monaghan in the early 1990's [*Monaghan*, 1994]. Monaghan [1994] accomplished this application by extending the existing SPH equations to nearly incompressible fluids and incorporating boundaries into the method. His work was discussed and improved upon by many later authors including Hughes and Graham [2010] and Vaughan [2009]. These works in SPH follow the same fundamental principles that will be discussed in this subsection.

2.3.1 SPH Fundamentals and Kernel

The SPH model consists of many moving grid points placed in the computational domain, each possessing quantities including mass, density, pressure, and velocity. Literature on the subject commonly refers to these grid points as particles, which is how we will refer to them to be consistent [*Crespo et al.*, 2008; *De Leffe et al.*, 2010]. The quantities at each of these particles are calculated based on the kernel function

$$f(x) = \sum_j f_j W(x - x_j) V_j \tag{2.4}$$

where:

$f(x)$ is the value of a quantity, such as density

f_j is the value of the quantity at point j

$W(x - x_j)$ is the weighting function

V_j is the volume of the particle at point j

as noted in [*Gomez-Gesteira et al.*, 2010]. The kernel function equation shows that the quantity calculated at a specific particle is influenced by the surrounding particles based on the weighting function.

2.3.2 Weighting Function

There are multiple types of weighting function, but there are seven basic requirements for the weighting function. First, the sum of the weighting function over the domain must equal one to provide unity. Second, the weighting function must provide compact support. This means the weighting kernel should be contained within a radius of κh, where κ is a scaling factor and h is the smoothing length. The function should also be positive at all points within the kernel to ensure a physically significant quantity. A decay requirement is also stated so that the function places more emphasis on the particles toward the center of the kernel. The function should also mimic the Dirac delta function in that the weight at the outer edges of the function should approach zero as the kernel radius increases. Another requirement is that the weighting function is even, meaning the weight is the same for points at the same radial distance from the center. Finally, the weighting function should be smooth enough to avoid numerical instabilities and protect against large errors due to slight changes in particle locations [*liu and liu*, 2010].

Two examples of commonly used weighting functions are the quadratic method and the cubic spline method as discussed in [*Gomez-Gesteira et al.*, 2010]. In the three dimensional domain used for this project, the quadratic method is:

$$W(r,h) = \alpha_D \left[\frac{3}{16} q^2 - \frac{3}{4} q + \frac{3}{4} \right] \tag{2.5}$$

when $0 \le q \le 2$ and where:

h is the smoothing length

and:

$$\alpha_D = \frac{5}{4\pi h^3} \tag{2.6}$$

$$q = \frac{r}{h} \tag{2.7}$$

$$r = \left(x - x_j \right) \tag{2.8}$$

Figure 1 shows an example of the shape of the quadratic weighting function for r ranging from -1 to 1 and $h = 0.5$. In this figure, the abscissa represents the distance from the center of the kernel and the ordinate shows the relative weighting of a particle at this distance.

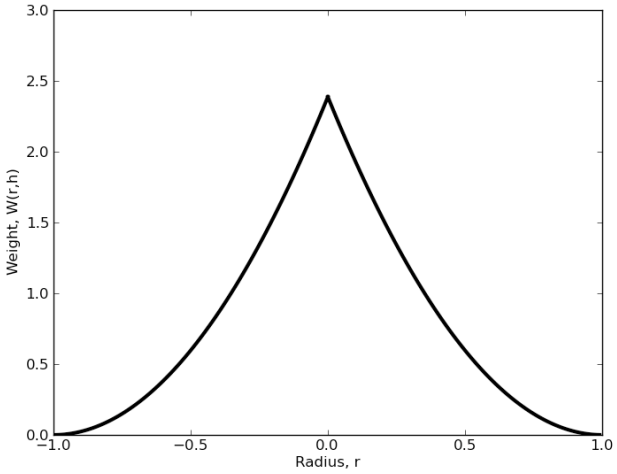

Figure 1. Shape of quadratic weighting function with a smoothing length of 0.5

The cubic spline method represents the weighting function:

$$W(r,h) = \alpha_D \begin{cases} 1 - 1.5q^2 + 0.75q^3 & 0 \le q \le 1 \\ 0.25(2-q)^3 & 1 \le q \le 2 \\ 0 & q \ge 2 \end{cases} \tag{2.9}$$

where:

$$\alpha_D = \frac{1}{\pi h^3} \tag{2.10}$$

Figure 2 shows an example of the cubic spline weighting function for r ranging from -1 to 1 and $h = 0.5$. Again, the abscissa shows the distance from the center of the kernel and the ordinate shows the relative weighting of a particle at this distance.

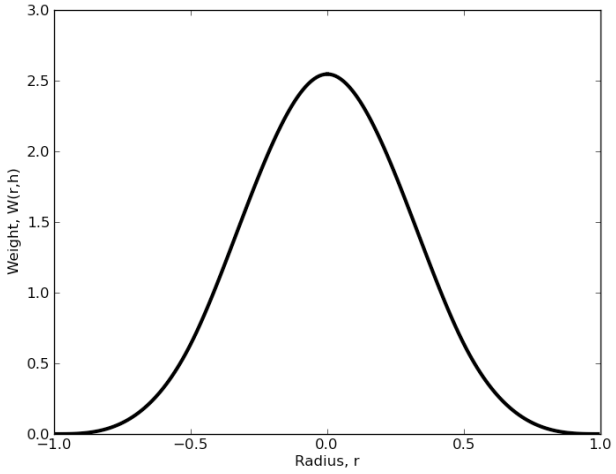

Figure 2. Shape of cubic spline weighting function with a smoothing length of 0.5

2.3.3 Continuity Equation and Equation of State

The basic weighting function above is calculated for each quantity including density, pressure, etc. To obtain initial values of these quantities at each time step, SPH follows the basic laws of fluid motion. The continuity equation ensures the conservation of mass by calculating any changes in density of the weakly compressible fluid by:

$$\frac{d\rho_a}{dt} = \sum_b m_b u_{ab} \nabla_a W_{ab} \tag{2.11}$$

where:

m_b is the mass of particle b

u_{ab} is the velocity vector from particle a to particle b

W_{ab} is the weighting function calculating the influence of particle b on particle a [*Gomez-Gesteira et al.*, 2010].

The density calculated in the continuity equation is then used in the equation of state to calculate the pressure as shown here.

$$p = B\left[\left(\frac{\rho}{\rho_0}\right)^{\gamma} - 1\right] \tag{2.12}$$

where

p is the pressure

and

$$B = \frac{c_0^2 \rho_0}{\gamma} \tag{2.13}$$

$$\gamma = 7$$

$$\rho_0 = 1000 \text{ kg m}^{-3}$$

$$c_0 = \sqrt{\left.\frac{\partial p}{\partial \rho}\right|_{\rho_o}} \tag{2.14}$$

2.3.4 Conservation of Momentum

The conservation of momentum used in the model, which includes a diffusion term is:

$$\frac{D\vec{u}}{Dt} = -\frac{1}{\rho}\nabla p + \vec{g} + \vec{\Theta} \tag{2.15}$$

where:

u is the velocity

t is the time

ρ is the density

p is the pressure

g is the gravitational acceleration

Θ is the diffusion term

Similar to the weighting function, there are different methods to calculate the diffusion term in the momentum conservation equation. Gomez-Gesteira, et. al. [2010] discussed three approaches: artificial viscosity, laminar viscosity, and full viscosity. This current thesis did not use the artificial viscosity approach, but it did utilize and compare the laminar and full viscosity approaches. This comparison was important because the full viscosity approach combines the laminar viscosity approach with a calculation to account for Sub-Particle Scale (SPS) turbulence.

When using the laminar viscosity calculation, the diffusion term can be written as:

$$\vec{\Theta} = \nu_0 \nabla^2 \vec{u} \tag{2.16}$$

where

$$\left(\nu_0 \nabla^2 \vec{u}\right)_a = \sum_b m_b \left(\frac{4\nu_0 \vec{r}_{ab} \nabla_a W_{ab}}{\left(\rho_a + \rho_b\right)\left|\vec{r}_{ab}\right|^2} \right) \vec{u}_{ab} \tag{2.17}$$

where υ_0 is kinetic viscosity of laminar flow.

When adding the SPS term to represent full viscosity, equation 2.16 becomes:

$$\vec{\Theta} = \nu_0 \nabla^2 \vec{u} + \frac{1}{\rho} \nabla \bar{\tau} \tag{2.18}$$

where τ is the turbulent stress tensor. The stress tensor is calculated assuming the Boussinesq hypothesis of eddy viscosity and Favre-averaging. With these assumptions, the tensor τ_{ij} can be calculated using:

$$\frac{\tau_{ij}}{\rho} = \nu_t \left(2S_{ij} - \frac{2}{3} k \delta_{ij} \right) - \frac{2}{3} C_t \Delta l^2 \delta_{ij} \left| S_{ij} \right|^2 \tag{2.19}$$

where the turbulent eddy viscosity (ν_t) is:

$$\nu_t = \left[C_s \Delta l \right]^2 |S| \tag{2.20}$$

where:

k is the SPS turbulent kinetic energy

C_s is the Smagorinsky constant, 0.12

C_t is 6.6 x 10^{-3}

Δl is the particle spacing

$$|S| = \left(2 S_{ij} S_{ij} \right)^{0.5} \tag{2.21}$$

where S_{ij} is the element of the SPS strain tensor [*Gomez-Gesteira, et al.*, 2010].

After these viscosity and turbulence terms are taken into account, the velocities determined from the conservation of momentum equation is then used to calculate particle movement by:

$$\frac{d\vec{r}}{dt} = \vec{u}_a + \varepsilon \sum_b \frac{m_b}{\overline{\rho}_{ab}} \vec{u}_{ba} W_{ab} \tag{2.22}$$

where ε = 0.5, a correction factor, and

$$\overline{\rho}_{ab} = \frac{\rho_a + \rho_b}{2} \tag{2.23}$$

as discussed by Dalrymple and Rogers [2006].

It is important to note that because boundary particles are not part of the modeled fluid, they do not move according to these equations, but they will be discussed in the next subsection [*Dalrymple and Rogers*, 2006; *Gomez-Gesteira et al.*, 2005].

2.3.5 Boundary Particles

Boundary particle forces are implemented to prevent the fluid particles from penetrating the simulated solid walls in the domain. There are two options for calculating the boundary particles in the GPUSPH model, the Lennard-Jones condition and the Monaghan and Kajtar condition, abbreviated LJ and MK, respectively [*Herault et al.*, 2011]. The LJ boundary force is:

$$f(r) = D\left(\left(\frac{r_0}{r}\right)^{p1} - \left(\frac{r_0}{r}\right)^{p2}\right)\frac{\mathbf{r}}{r^2} \tag{2.24}$$

where

$$D = 5gH \tag{2.25}$$

H is a characteristic water depth

r_0 is the initial particle spacing

r is the spacing between the boundary particle and the fluid particle

r is the vector form of r

$p1$ is a coefficient, 12

$p2$ is a coefficient, 6

The force is set to zero if r is greater than r_0 to avoid producing attractive forces to the boundary as discussed by Monaghan [1994].

The LJ calculation of the boundary particle forces can produce an artificial non-zero tangential force on the passing fluid particles as discussed in Monaghan and Kajtar [2009]. The authors introduce the MK method to calculate these forces, producing a radial force for each boundary particle which translates into a net normal force to the boundary plane with a negligible tangential component.

The authors determined that the MK boundary particle force is:

$$f_{aj} = \frac{K}{\beta}\frac{\vec{r}_{aj}}{r_{aj}^2}W\left(r_{aj}/h\right)\frac{2m_j}{m_a + m_j} \tag{2.26}$$

where:

f_{aj} is the boundary force of particle j exerted on fluid particle a

$$K = gH \tag{2.27}$$

β is the ratio of boundary particle spacing to fluid particle spacing

$\boldsymbol{r}_{aj}$ is the vector radius from particle a to particle j

r_{aj} is the magnitude of the radius from particle a to particle j

$W(r_{aj}/h)$ is the weighting function

m_j is the mass of boundary particle j

m_a is the mass of fluid particle a

To ensure that the forces were adequately representing a normal force, the normal forces were compared to the tangential forces of boundary particles in a straight line. Their calculations produced ratios ranging from 1×10^{-8} to 9×10^{-5} for various β values and kernel functions, showing that the force calculation was adequate, especially for β values at 3 or above. Additionally, a numerical two-dimensional tank with a bottom and two sides of boundary particles was created and filled with fluid particles to test the influence of the boundary particle forces. This experiment showed that the fluid particles were repelled to approximately one particle spacing value away from each of the sides, as expected.

2.3.6 Shephard Filtering for Numerical Instabilities at the Free-Surface

In addition to the effects at the bottom and side boundaries, numerical effects on the free-surface boundary of the fluid are also considered. Dalrymple and Rogers [2006] discussed the use of Shephard filtering in the SPH model to account for these numerical instabilities. Densities of particles at the free-surface tend to be artificially skewed due to fewer particles in the top half of each weighting kernel. This slight variation is then incorporated into the calculation of pressure as shown in equation 2.12, unintentionally causing a surface that appears unnaturally rough when using the full viscosity calculation. To solve this problem, a Shephard filtering equation was implemented every 40 time steps to average these variations, producing a smoother and more natural surface. This filtering is quantified as

$$\rho_i = \frac{\sum_j \rho_j W_{ij} V_j}{\sum_j W_{ij} V_j} \tag{2.28}$$

The authors note that due to the proximity of the particles used in the averaging this averaging only removes the artificial numerical non-linear effects and does not remove the real non-linear effects of the surface.

2.3.7 Example Study Completed with SPH for Free-Surface Flows

The SPH method has been studied for fluid flow and analyzed for various free-

surface flow test cases. SPH was used to study green water overtopping on a deck and to validate numerical results against experimental results [*Gomez-Gesteira, et al.,* 2005]. The experiment, originally conducted by Cox and Ortega [*Cox and Ortega*, 2002], involved placing a fixed deck in a wave flume and allowing green water, i.e. unbroken waves, to overtop the deck as shown in Figure 3. The figure shows the elevation and plan view of the experiment, noting the fixed deck near the 8.0 m mark.

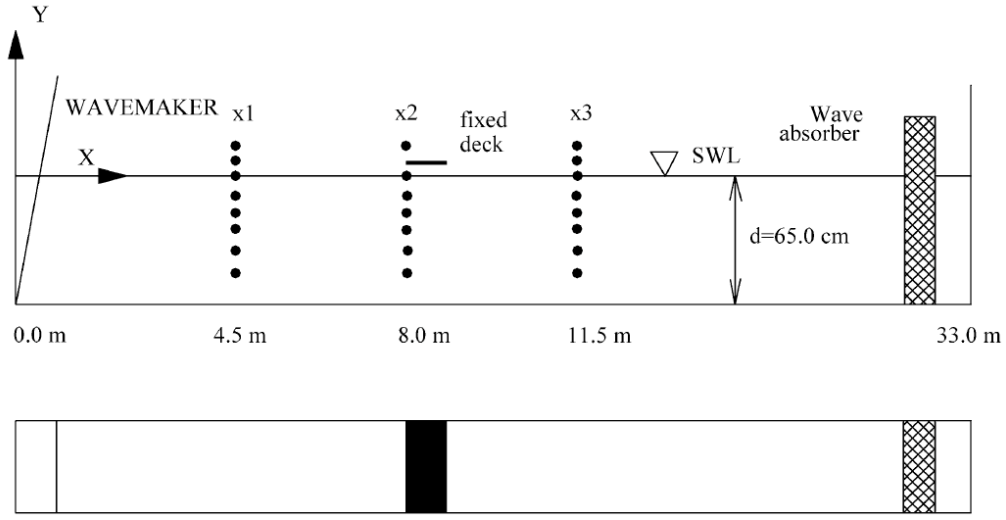

Figure 3. Elevation and plan view of experimental setup of Cox and Ortega, from [*Gomez-Gesteira et al.*, 2005]

Gomez-Gesteira et al. [2005] used a smoothing length for fluid particles of h_F = 4.55 x 10^{-2} m and a smoothing length for boundary particles of h_B = 9.0 x 10^{-3} m. The smoothing length for interactions between the fluid and boundary particles was taken as $h_{BF} = 0.5(h_F+h_B)$. The model used a spline-based kernel function and a two-dimensional particle spacing of 3.5 x 10^{-2}-m. While the fluid particles were allowed to move throughout the system, the boundary particles were stationary during the entire simulation.

Gomez-Gesteira et al. [2005] found that, when comparing the numerical results to the experimental results, the outcomes were similar but often damped in the numerical results. When comparing free-surface elevation for the case without the fixed deck present, as seen in Figure 4, they found that the phase and amplitude of the numerical signal correctly mimicked that of the experimental setup. In this figure, the abscissa shows time in seconds and the ordinate axis shows the surface elevation in meters. The first wave was found to be slightly delayed in the numerical system and the highest wave height was somewhat damped as determined by comparing the numerical results (heavy line) and the experimental results (light line).

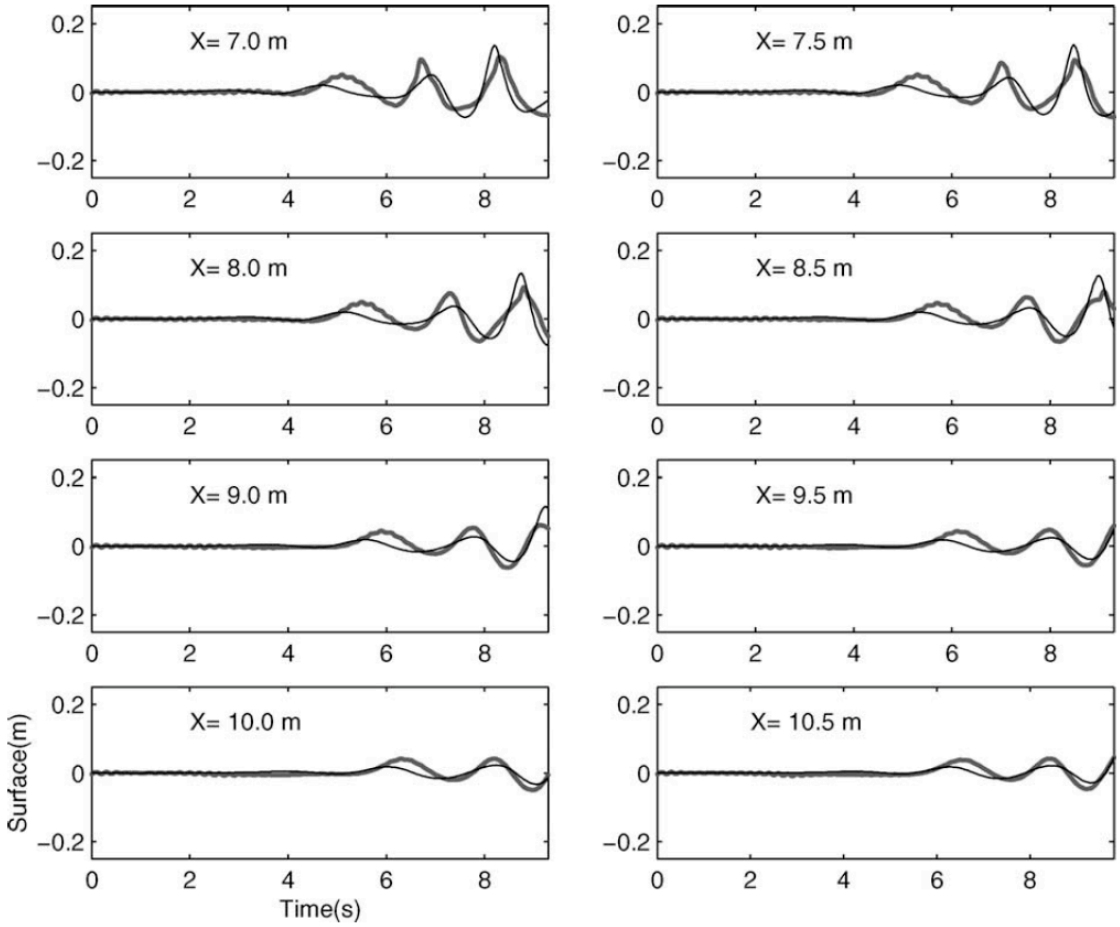

Figure 4. Free-surface measurements in absence of deck; comparison between numerical signal (heavy solid line) and experimental signal (light solid line), from [*Gomez-Gesteira et al.*, 2005]

Additionally, when comparing velocity profiles for both the cases including and not including the fixed deck, maximum velocities were slightly less in the numerical cases. This is shown by comparing the experimental results on the left side in Figure 5 and the numerical results on the right side in Figure 5. Each of these plots show velocity in meters per second on the abscissa and water height in meters on the ordinate. The

authors attributed this dampening to the averaging of the values due to the kernel function. The particle spacing could also contribute to this dampening by not providing enough moving grid points to accurately capture the flow.

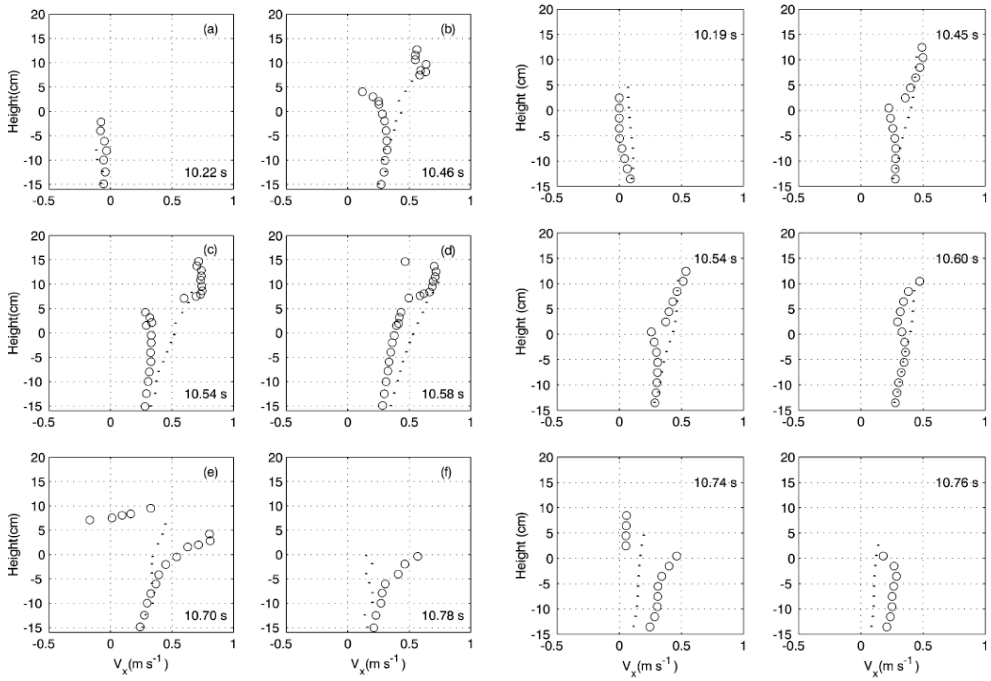

Figure 5. Vertical variation in experimental (left side) and numerical (right side) horizontal velocity. Open circles represent data with deck, dots represent data without deck, from [*Gomez-Gesteira et al.*, 2005]

2.4 GPUSPH

As higher resolution runs were required for more accurate results, the SPH models tended to require extensive amounts of computing power and time. To combat this problem, GPUSPH, nee GPU-SPHysics, was implemented by calculating the SPH equations on graphical processing units (GPU) on NVIDIA cards using Compute Unified Device Architecture (CUDA).

The parallel processing structure of a GPU makes it well suited for the SPH problem, when compared to the traditional sequential structure of a central processing unit (CPU). Before the use of GPU for SPH, the model was run in a sequential form on CPU, meaning the calculations were completed one at a time. Instead, GPU are composed of many cores that allow for multiple calculations of the same type at a time, which increases the resolution capabilities of the model and decreases the time required to complete the runs. Previously, extensive parallel processing power was limited to high end massive computers usually found in government and academic facilities, but GPU have become widely available in recent years due to the demand for better graphics, especially in the gaming industry [*Kirk and Hwu*, 2010].

The first implementations of SPH on GPU used Open Graphics Library (OpenGL) and C for graphics (Cg) that required an understanding of the GPU architecture and of how to convert between graphics and mathematical operations. Since

those attempts, CUDA, a programming language, was released that allows programmers to utilize the processing power of the GPU using the more commonly known C/C++ programming language. CUDA also allows the programmer to call the GPU to execute calculations better suited to the parallel processing environment and to call the CPU for more sequentially suited tasks [*Harada et al.*, 2007; *Herault et al.*, 2010].

Herault et al. [2010] discussed the computing logistics in detail and compared processing times of the SPH model on CPU versus GPU. The authors noted that for one particular setup, they were able to use more than 100 times more particles using GPU instead of a single CPU due to the parallel processing power and memory of the GPU. In addition to finding that the GPU is able to implement more particles into the system, the authors also calculated speed-ups for various components of the SPH modeling process on GPU, as opposed to CPU, as ranging from 4.4 to 207 times faster.

Even though GPUSPH has the ability to implement the SPH model at higher resolutions, these runs can still last for days or months depending on many factors including the setup, data collection rate, and number of particles present. Often the setup and data collection rate are determined by the problem, but the number of particles present in the system is set by the user. Fewer particles in the system would allow for faster processing, but it is important to have an adequate number of particles to obtain

accurate results. This study used the GPUSPH model to determine a method for setting the optimal number of particles in the system.

2.5 Summary of Literature Review

This literature review provided a brief overview of the need to improve numerical modeling and continue work in the fluid modeling field. The Lagrangian mesh-free SPH method of modeling free-surface flows was explained using the pertinent equations of the approach. The fundamental idea of the method is that the characteristics such as density, pressure, and velocity at each particle are averaged in a weighted manner within the kernel function. The weighting function can vary, but there are seven basic requirements that all weighting functions must fulfill as discussed in Subsection 2.3.2, where two examples are provided. To calculate the characteristics used in the kernel function, the particles in the system follow the basic fluid equations including the continuity equation, the equation of state, and the conservation of momentum equation discussed in Subsections 2.3.3 and 2.3.4. Subsection 2.3.5 discussed the equations that affect the boundary particles and prevent fluid particles from penetrating the boundaries.

After discussing the governing equations of SPH, the concept of Shephard filtering to prevent unnatural pressures and densities at the free-surface particles was introduced. Lastly in the SPH subsection, an example was provided proving that SPH is

a viable numerical modeling option.

Subsection 2.4 introduced the concept of parallel processing using GPU to create GPUSPH. The parallel processing of GPUSPH allows the SPH model to run with better resolution in less time using the CUDA architecture. With the immense computing power and time required to run the SPH model, it is important to find the optimal particle spacing that uses the least time and produces accurate results. This study provides a framework for identifying this optimization to solve complex fluid flow problems in a reasonable amount of time.

3. TEST CASES AND MEASUREMENT METHODS

3.1 Introduction

This subsection will discuss the cases used to test the GPUSPH model and the methods used to post-process the data. In order to understand the effects of vegetation on free-surface flows, the flow characteristics around a single piece of vegetation must be understood. To accurately use GPUSPH to study the flow around a vegetative piece, the model must be validated for this case and for flow through a flume without vegetation.

To validate the model, there are two test cases used in this work that simulate a dam break type flow involving a block of water retained at one end of a flume or tank and then instantaneously released to flow throughout the container. For these cases, referred to as DamBreak 1 and DamBreak 2, data was collected and compared to numerical results to draw conclusions on the accuracy of the GPUSPH model and its sensitivity to various changes in the setup. All simulations ran on one of four single precision Tesla C1060 cards that has 240 processor cores and 4 GB of dedicated memory [*NVIDIA*, 2010].

3.2 Test Case: DamBreak 1

The first case was modeled based on a physical experiment by Yeh and Petroff [*Raad*] at the University of Washington in 2003. Their experiment simulated a dam

break by suddenly releasing water held by a plate and allowing the water to reach an obstruction in the tank, as shown in the plan view in Figure 6. They recorded the force of the water on the obstruction and the velocity of the water at a point 14.6 cm in front of the obstruction. Gomez-Gesteira and Dalrymple [2004] also simulated this experiment using SPH on CPU for a 0.02-m particle spacing.

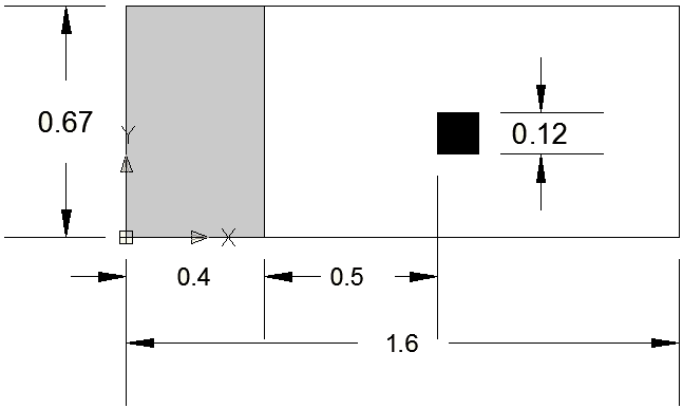

Figure 6. Plan view of DamBreak 1 setup in meters. Modified from [*Gomez-Gesteira, 2004*].

The GPUSPH setup for this research copies the experimental setup and consists of an open top flume that is 1.6 m long, 0.67 m wide, and 0.4 m deep. The four sides and bottom of the flume are filled with boundary particles using the LJ boundary particle forces as discussed in Section 2. A 0.12 m long by 0.12 m wide by 0.4 m tall closed top square cylinder obstruction is placed in the tank with its plan view center 0.96 m from the front edge of the box and 0.30 m from one of the side edges of the box. The six faces of this obstruction are also filled with boundary particles. Initially, water was

filled from 0.0 m to 0.4 m lengthwise as indicated by the gray shading in the figure, filling the width and height of the box in this area. Additionally, there is a thin layer of water approximately 0.01 m deep in the remaining area of the setup to simulate the residual water from the physical experiment. There is no barrier holding back the water, causing it to instantaneously begin flowing towards the obstruction at initiation of the model.

The DamBreak 1 case was implemented for three scenarios and 18 particle spacings for a total of 54 simulations as outlined in Table 1 and Table 2. The scenarios varied based on the type of kernel function used in the weighted approximation of quantities. The scenarios were also varied in the inclusion of the Sub-Particle Scale (SPS) Turbulence term in the momentum equation.

SPH literature often discusses cases in terms of number of particles instead of the particle spacing that is discussed in this paper. Table 3 provides a listing of the number of fluid particles and the number of total particles, fluid and boundary, in the system for each particle spacing to help readers compare these results to other publications.

Table 1. Description of scenarios used for comparisons

	Kernel Weighting Function	Sub-Particle Scale (SPS) Inclusion
Scenario 1	Quadratic	Yes
Scenario 2	Quadratic	No
Scenario 3	Cubic Spline	Yes

Table 2. Description of particle spacing cases for DamBreak 1

	Particle Spacing (m)					
Scenario 1	3.5×10^{-3}	4×10^{-3}	5×10^{-3}	6×10^{-3}	7×10^{-3}	8×10^{-3}
Scenario 2						
Scenario 3						
Scenario 1	9×10^{-3}	1.0×10^{-2}	1.1×10^{-2}	1.2×10^{-2}	1.3×10^{-2}	1.4×10^{-2}
Scenario 2						
Scenario 3						
Scenario 1	1.5×10^{-2}	1.6×10^{-2}	1.7×10^{-2}	1.8×10^{-2}	1.9×10^{-2}	2.0×10^{-2}
Scenario 2						
Scenario 3						

Table 3. Number of total and fluid particles for each particle spacing setup for DamBreak 1

Particle Spacing (m)	Number of Particles	Number of Fluid Particles	Particle Spacing (m)	Number of Particles	Number of Fluid Particles
3.5×10^{-3}	2,870,570	2,617,200	1.2×10^{-2}	86,888	65,652
4×10^{-3}	1,931,748	1,739,420	1.3×10^{-2}	68,944	50,840
5×10^{-3}	1,048,619	923,898	1.4×10^{-2}	56,581	41,043
6×10^{-3}	592,880	507,540	1.5×10^{-2}	46,969	33,416
7×10^{-3}	389,434	326,232	1.6×10^{-2}	38,480	26,808
8×10^{-3}	260,143	212,617	1.7×10^{-2}	34,138	23,496
9×10^{-3}	191,842	153,820	1.8×10^{-2}	29,896	20,428
1.0×10^{-2}	147,137	115,859	1.9×10^{-2}	26,312	17,692
1.1×10^{-2}	109,927	84,651	2.0×10^{-2}	23,059	15,247

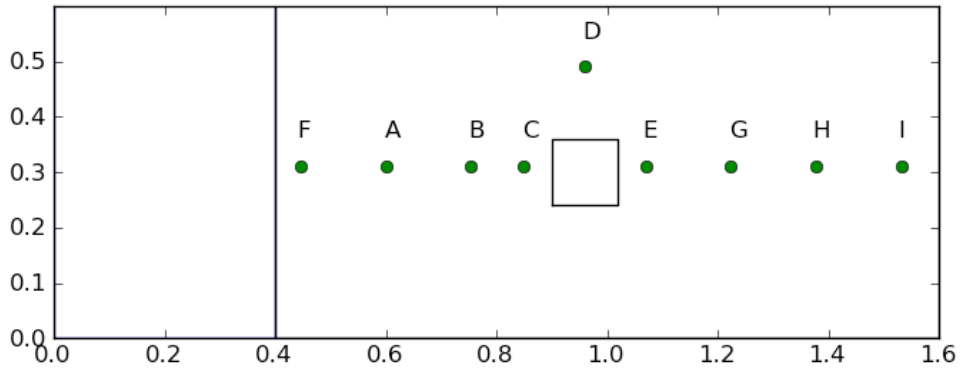

Figure 7. Locations of velocity calculations in DamBreak 1 (in meters)

Model output was saved at 100 Hz for 3 seconds as a text file for each recording time. The text file contained the parameters position (x, y, z), particle ID, velocity (u, v, w), mass, density, pressure, and vorticity (x, y, z) for each particle. Post-processing included calculating velocity values at the specific locations shown in Figure 7 in the fluid using the kernel function. The kernel functions used in post-processing were kept the same as the kernel functions used in the model for each scenario, quadratic or cubic spline.

Force on the obstruction in the direction of flow (x-direction) was calculated using the pressure values of the particles directly in front of and behind the obstruction. Blocks of 3 particle spacings by 3 particle spacings in the y, z plane and 4 particle spacings in the x-direction, which is the direction of flow, were created on the fluid sides of the front and back planes of the obstruction. The pressure values of the particles were averaged within the blocks and multiplied by the 3 by 3 particle spacing area of the

block to produce a force value. These forces were then added to generate an overall force value in the x-direction.

3.3 Test Case: DamBreak 2

A newer version of GPUSPH was released, allowing us to model the second test case that we were unable to model in the older version of GPUSPH. The newer version of GPUSPH includes an option of substituting particleless planes for the boundary particle filled walls. Because the walls no longer contain particles, the model is able to implement more fluid particles for the given memory available. Since the second experiment was conducted in a much larger flume than the first experiment, we required more fluid particles to produce meaningful results.

The setup for this case was modeled based on an experiment done by Arnason et al. [2009]. The experiment was conducted in a flume 16.6 m long, 1.6 m wide, and 0.45 m deep, with a bottom of boundary particles using the MK boundary force calculation. The front, back, and sides of the flume were planes without particles. There was no obstruction in the flume for this case. The flume was filled with fluid particles up to a 0.02 m depth from x = 5.9 m to x = 16.6 m and up to a 0.10 m or 0.15 m depth from x = 0.0 m to x = 5.9 m, depending on the case. A side view of this setup is demonstrated in Figure 8.

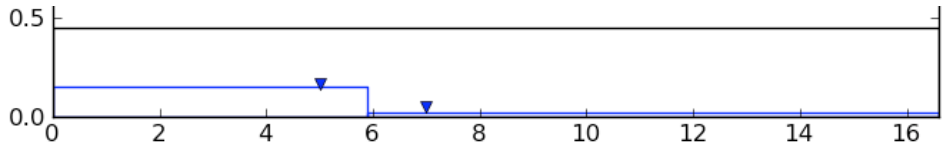

Figure 8. Side view of DamBreak 2 for 0.15 m initial higher free-surface elevation with vertical exaggeration (in meters)

Table 4. Description of particle spacing cases for DamBreak 2

Initial Higher Water Depth (m)	Scenario	Particle Spacing (m)				
0.15	1	6.0×10^{-3}	7.5×10^{-3}	1.00×10^{-2}	1.25×10^{-2}	1.50×10^{-2}
	2					
	3					
0.10	1	6.0×10^{-3}	7.5×10^{-3}	1.00×10^{-2}	1.25×10^{-2}	1.50×10^{-2}
	2					
	3					

Similar to DamBreak 1, DamBreak 2 was completed for the three scenarios detailed in Table 1 for various particle spacings and initial higher free-surface elevations as outlined in Table 4. To provide data for comparison to other work in the SPH field, a conversion table between particle spacing and number of particles in the system has been provided in Table 5.

Table 5. Number of total and fluid particles for each particle spacing setup for DamBreak 2

Initial Higher Free-Surface Elevation (m)	Particle Spacing (m)	Number of Particles	Number of Fluid Particles
0.10	6.0×10^{-3}	2,663,767	2,263,185
0.10	7.5×10^{-3}	1,402,134	1,145,250
0.10	1.00×10^{-2}	618,581	473,605
0.10	1.25×10^{-2}	328,449	235,468
0.10	1.50×10^{-2}	212,467	145,845
0.15	6.0×10^{-3}	3,548,467	3,103,650
0.15	7.5×10^{-3}	1,842,294	1,557,900
0.15	1.00×10^{-2}	759,941	603,185
0.15	1.25×10^{-2}	419,073	316,652
0.15	1.50×10^{-2}	275,347	200,865

Experimental data available in [*Arnason et al.*, 2009] that will be compared in this project includes the depth averaged x-direction velocity at a point 5.2 m downstream of the meeting between the higher and lower free-surface elevations. There is also a velocity profile with depth at the same location available for the 0.15-m initial higher free-surface elevation. The depth averaged x-direction velocity was calculated by taking the mean of the x-direction velocities of the particles contained within a cylindrical column centered at the measurement point. The column was specified with a radius of 3 times the particle spacing in order to capture enough particles to create an accurate mean of the data. The velocity profile was calculated by implementing the weighting function on the x-direction velocity values at the points of experimental measurement in the depth of the fluid using each scenario's respective kernel function.

Numerical data for this setup was collected at 10 Hz. As will be seen in Section 4, once the bore reaches the measurement point, the flow direction velocity stays relatively stable for many seconds. To compare the outputs for various cases, the mean of this relatively stable velocity was computed over a six second period behind the bore for the numerical and experimental data. The method provides one velocity value per case to analyze against the experimental data.

The data collected from these two setups were analyzed based on a variety of factors including percent errors and general flow shape. The numerical output and how well it compares to the experimental data will be discussed in Section 4.

4. RESULTS

4.1 Introduction

This subsection contains the numerical results from the GPUSPH model and compares these results to the experimental results from Yeh and Petroff and Arnason et al. In addition to the available data in these two papers, other characteristics of the numerical results will be analyzed to find conclusions about the GPUSPH model's convergence with respect to particle spacing, weighting function kernel, and inclusion of the SPS turbulence term.

The results are organized by test case, with DamBreak 1 appearing first and DamBreak 2 appearing second. For most aspects of the test cases that will be compared, the analysis will first discuss the effect of particle spacing using only Scenario 1, including the quadratic kernel and SPS turbulence term. The analysis will then include a comparison of Scenarios 1 and 2, using the quadratic kernel with and without the SPS turbulence term, to determine the effect of the SPS turbulence term on the numerical results. Finally, Scenarios 1 and 3, using the SPS turbulence term with the quadratic or cubic spline kernels, will be compared to determine the importance of the kernel type in the model results.

The DamBreak 1 analysis will include a comparison of the numerical data to the available experimental velocity and force data. Even though there is no experimental data available of the time required for the initial bore to reflect off the back wall of the

tank, numerical results of this value will be compared with each other. Additionally, the overall structure of the 9 x 10^{-3}-m particle spacing flow field will be studied at three different time steps in the simulation.

The DamBreak 2 analysis will contain a comparison of the numerical data to the experimental data of overall flow in the system. Additionally, the effect of the initial particle placement will be discussed as it relates to the velocity of the bore. After the overall velocity has been analyzed, the numerical boundary layer velocity will be compared to the experimental boundary layer velocity. This section will then end with a summary of the results.

4.2 Test Case: DamBreak 1

4.2.1 Experimental Velocity Results Comparisons

As discussed in Section 3, Yeh and Petroff recorded the velocity in the direction of flow at a point 0.354 m downstream of the water release gate, centered with respect to the obstruction, shown in Figure 6. Their velocity data points tended to occur in two distinct groups with respect to time. The group within the range of 0.0 s to 0.7 s clearly shows the maximum velocity measurement when the bore reached the measurement point and the subsequent deceleration of the water. The second group of data points occurs after 0.8 s when the velocity values are relatively low. The most important part of this available data is the first set of data points because it includes the peak velocity value and demonstrates how the velocity dissipates with time just after the peak. For this reason, we will only consider the first set of data points.

The velocity at this point of comparison in the numerical results was calculated in post-processing based on the same weighting function method used in the GPUSPH model for each time step. The time values of the numerical results were shifted so that the peak velocity value occurs at time t = 0.0 s as it does in the experimental results. A 0.04 s moving time average was applied to numerical velocity values to smooth the curve and provide better comparisons with the results. The 0.04 s average was chosen because it adequately removed the artificial noise of the time series while retaining the characteristic shape and peak of the data.

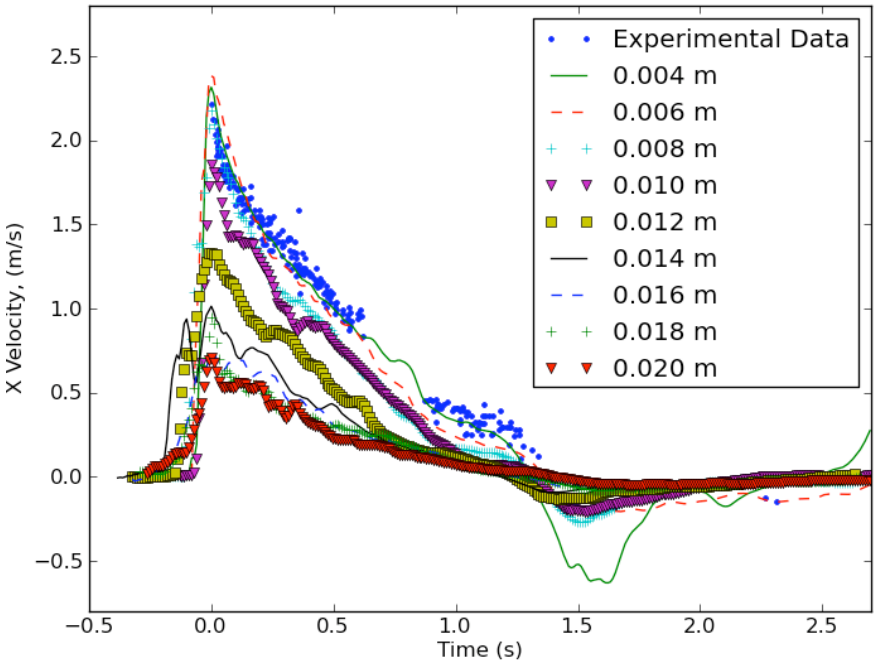

Figure 9. Velocity time series in the direction of flow for selected Scenario 1 (quadratic kernel, SPS term) cases

Figure 9 is the velocity time series for half of the particle spacings for the Scenario 1 test case. The abscissa contains time in seconds with respect to the time of peak velocity and the ordinate axis is the velocity in the direction of flow. The plot shows the trend that cases with larger particle spacings tend to produce less accurate results, as evidenced by the low velocity values for spacings of 1.3 x 10^{-2}-m and greater in the figure. While this figure only includes results from Scenario 1, there is a similar trend in the results from Scenarios 2 and 3 as will be discussed later. While the details of this trend will be discussed further below, this figure agrees with our overall expectation that smaller particle spacings will produce more accurate results than larger particle spacings.

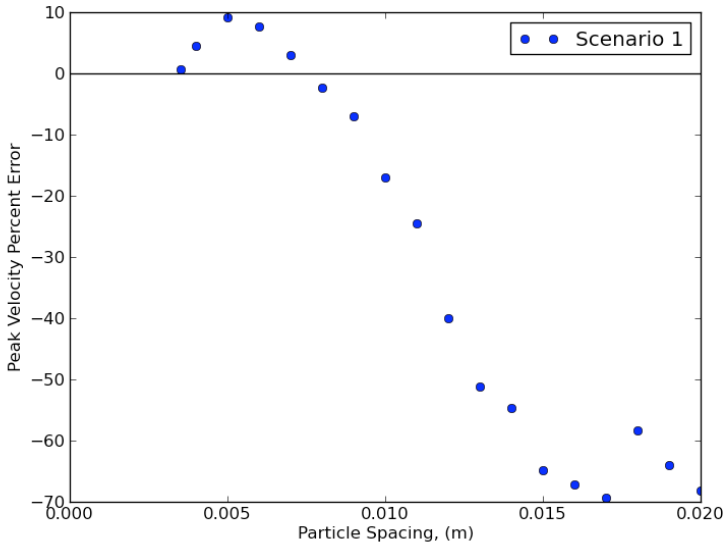

Figure 10. Peak velocity percent error as a function of particle spacing for Scenario 1 (quadratic kernel, SPS term)

To analyze the accuracy of the numerical results, peak velocity values were compared to the peak velocity value of the experimental results using the percent error calculation:

$$error = \frac{v_n - v_e}{v_e} \times 100 \tag{4.1}$$

where:

v_n is the numerical value

v_e is the experimental value

Table 6. Peak velocity percent error for Scenario 1

Scenario 1 (Quadratic Kernel, SPS term)					
Particle Spacing (m)	Peak Velocity Value (m/s)	Percent Error	Particle Spacing (m)	Peak Velocity Value (m/s)	Percent Error
3.5×10^{-3}	2.23	0.73	1.2×10^{-2}	1.33	-39.92
4×10^{-3}	2.31	4.52	1.3×10^{-2}	1.08	-51.23
5×10^{-3}	2.41	9.14	1.4×10^{-2}	1.00	-54.59
6×10^{-3}	2.38	7.64	1.5×10^{-2}	0.78	-64.82
7×10^{-3}	2.28	3.07	1.6×10^{-2}	0.73	-67.11
8×10^{-3}	2.16	-2.28	1.7×10^{-2}	0.68	-69.38
9×10^{-3}	2.06	-6.96	1.8×10^{-2}	0.92	-58.31
1.0×10^{-2}	1.84	-16.93	1.9×10^{-2}	0.79	-64.06
1.1×10^{-2}	1.67	-24.47	2.0×10^{-2}	0.70	-68.16

Figure 10 and Table 6 show the percent error of the peak velocity numerical results as a function of particle spacing. The particle spacing is indicated on the abscissa and the ordinate shows the peak velocity percent error. Positive percent errors reflect

numerical results that are less than the peak experimental result. This figure shows that for larger particle spacings, there is an overall trend of increasing accuracy as particle spacing is decreased. As the particle spacing decreases into the median to high resolute range, the numerical results change from under predicting the peak velocity to over predicting the value, passing through the correct value, before trending again toward the measured result. While the results from the 7×10^{-3}-m and 8×10^{-3}-m spacing case are within approximately 3% of the experimental value, a smaller particle spacing of 5×10^{-3}-m over predicts the value by approximately 9% of the experimental result. For the most resolute cases of 3.5×10^{-3}-m and 4×10^{-3}-m particle spacings, the peak velocity result trends again to the experimental result.

This hook shape in the range of low particle spacings is expected and probably due to the single precision of the Tesla cards used for these simulations. Single precision calculations require the numerical values to be rounded to fit into the allotted memory available. While rounding these values usually do not create major numerical errors, the rounding process can become significant if there are enough calculations in the process. McCarn and Carr [1992] supports this claim by demonstrating that the use of single or double precision can have a significant impact on the accuracy of an iterative process. For example, in their study, for a particular sequence of iterative equations, the absolute errors were 0.144×10^{-2} for single precision and 0.408×10^{-11} for double precision. For the current work, more particles in the system require the model to perform more calculations, which is why it seems that there is some otherwise unexpected error, particularly around the 5×10^{-3}-m particle spacing.

Figure 11 compares the peak velocity percent errors for Scenarios 1 and 2, which represent the cases with and without the SPS turbulence term, respectively. Table 7 shows the values for the Scenario 2 results. Except for the particle spacing 6 x 10^{-3}-m, the results for these two cases are extremely similar. The results are almost identical at larger particle spacings and diverge slightly in the more resolute cases. This divergence trend is unexpected since it was assumed that a sub-particle scale term would have more effect when the sub-particle scale is larger as it is in scenarios with larger particle spacings. Regardless of this assumption, the overall results are not much different between the two scenarios showing that the SPS turbulence term does not have much influence in calculating the peak velocity value at this point.

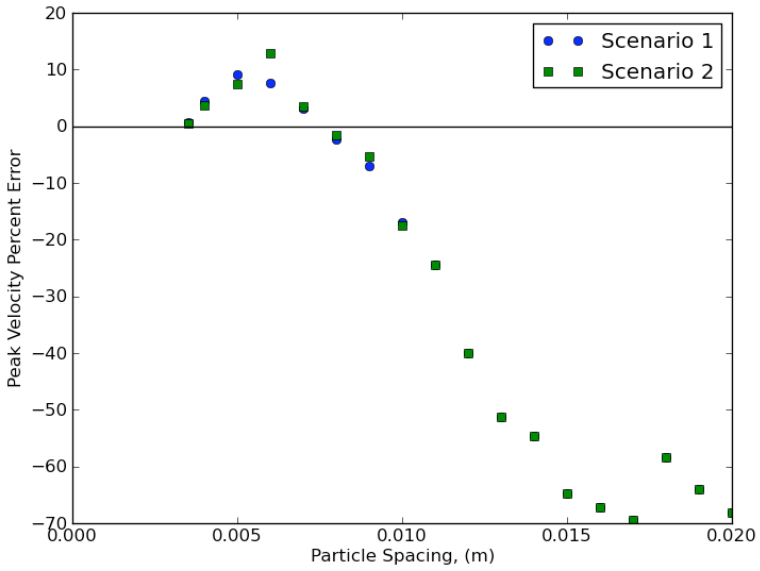

Figure 11. Peak velocity percent error as a function of particle spacing for Scenarios 1 and 2 using quadratic kernel and including or excluding the SPS turbulence term, respectively

Table 7. Peak velocity percent error for Scenario 2

Scenario 2 (Quadratic Kernel, No SPS term)					
Particle Spacing (m)	Peak Velocity Value (m/s)	Percent Error	Particle Spacing (m)	Peak Velocity Value (m/s)	Percent Error
3.5×10^{-3}	2.22	0.49	1.2×10^{-2}	1.33	-39.92
4×10^{-3}	2.30	3.76	1.3×10^{-2}	1.08	-51.24
5×10^{-3}	2.38	7.49	1.4×10^{-2}	1.00	-54.64
6×10^{-3}	2.50	12.87	1.5×10^{-2}	0.78	-64.82
7×10^{-3}	2.29	3.56	1.6×10^{-2}	0.73	-67.11
8×10^{-3}	2.18	-1.49	1.7×10^{-2}	0.68	-69.39
9×10^{-3}	2.09	-5.33	1.8×10^{-2}	0.92	-58.31
1.0×10^{-2}	1.83	-17.47	1.9×10^{-2}	0.79	-64.06
1.1×10^{-2}	1.67	-24.47	2.0×10^{-2}	0.70	-68.16

This similarity of results is probably due to lack of turbulence in the flow at the time the peak velocity is recorded. The SPS turbulence term should not have much effect if there is no sub-particle scale turbulence to calculate. Any contribution of sub-particle scale turbulence to the velocity caused by the bore is probably at relatively small scales compared to the overall velocity of the flow, causing it to be masked. The results in this figure confirm our expectations of the SPS turbulence term at this point in the flow.

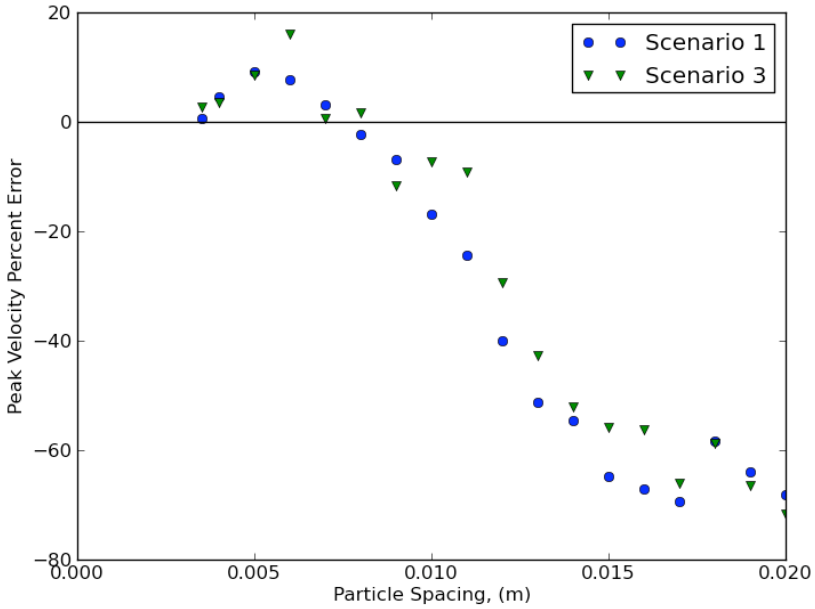

Figure 12. Peak velocity percent error as a function of particle spacing for Scenarios 1 and 3 using the SPS turbulence term and the quadratic or cubic spline kernels, respectively

Table 8. Peak velocity percent error for Scenario 3

Scenario 3 (Cubic Spline Kernel, SPS term)					
Particle Spacing (m)	Peak Velocity Value (m/s)	Percent Error	Particle Spacing (m)	Peak Velocity Value (m/s)	Percent Error
3.5×10^{-3}	2.27	2.74	1.2×10^{-2}	1.56	-29.36
4×10^{-3}	2.29	3.46	1.3×10^{-2}	1.27	-42.74
5×10^{-3}	2.40	8.56	1.4×10^{-2}	1.06	-51.99
6×10^{-3}	2.57	15.99	1.5×10^{-2}	0.98	-55.84
7×10^{-3}	2.23	0.66	1.6×10^{-2}	0.97	-56.16
8×10^{-3}	2.25	1.62	1.7×10^{-2}	0.75	-65.98
9×10^{-3}	1.95	-11.63	1.8×10^{-2}	0.91	-58.65
1.0×10^{-2}	2.05	-7.37	1.9×10^{-2}	0.74	-66.40
1.1×10^{-2}	2.01	-9.22	2.0×10^{-2}	0.63	-71.60

The cubic spline case's more variable behavior could be due to the greater importance its kernel function places on velocity values further from the center of the weighting kernel. As shown in Figure 1 and Figure 2, the quadratic weighting kernel function places high importance on the centermost velocity value and quickly decreases importance of values with increasing distance from the center of the kernel. The cubic spline weighting kernel function also places primary importance on the centermost velocity value, but it decreases importance more gradually with distance from the center of the kernel. The cubic spline function allows more particles to have a heavier influence on the calculated value in the weighting calculation as compared to the quadratic calculation.

Since the overall size of the weighting kernel function is larger with greater particle spacings, it is expected that the cubic spline kernel results are placing a greater emphasis on more area of the flow than the quadratic kernel results, particularly at greater particle spacings. Figure 12 and Table 8 supports this assumption, as the differences between the Scenario 1 and Scenario 3 results tend to be greater in the area of larger particle spacings when compared to the most resolute cases. The differences for the most resolute cases of 3.5×10^{-3}-m, 4×10^{-3}-m, and 5×10^{-3}-m particle spacings are minimal.

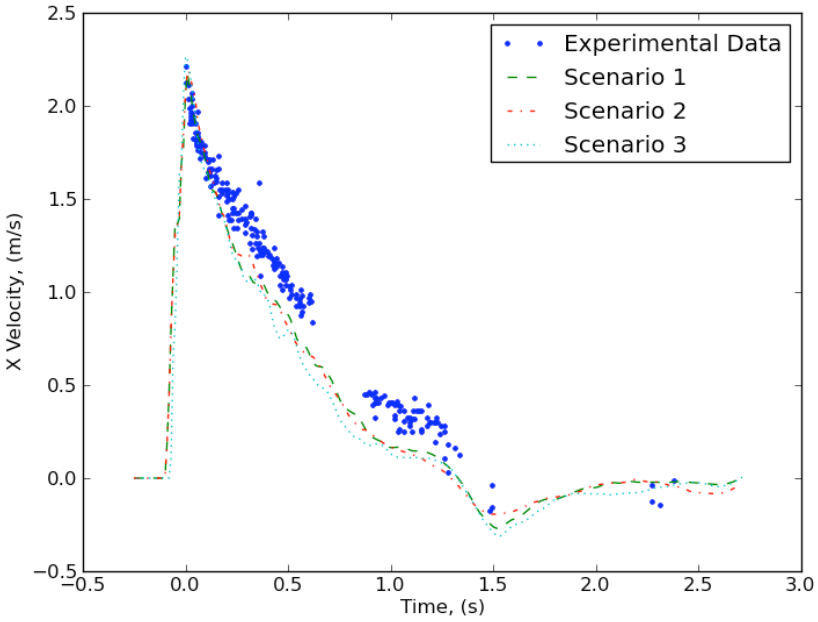

Figure 13. Velocity time series of Scenarios 1, 2, 3, and experimental results for particle spacing 8 x 10^{-3}-m

Despite the differences in results concerning the inclusion of the SPS term and the different weighting function kernels, all three scenarios show similar results for the 7 x 10^{-3}-m and 8 x 10^{-3}-m particle spacing cases. Figure 13 shows the velocity time series of the three scenarios and the time series of the experimental data for the 8 x 10^{-3}-m particle spacing. While the peak experimental velocity value matches well with the peak numerical velocity values, the overall velocity results are visibly less accurate than the peak velocity results. For this case, after the peak velocity is reached, the experimental and numerical results tend to decay at different rates.

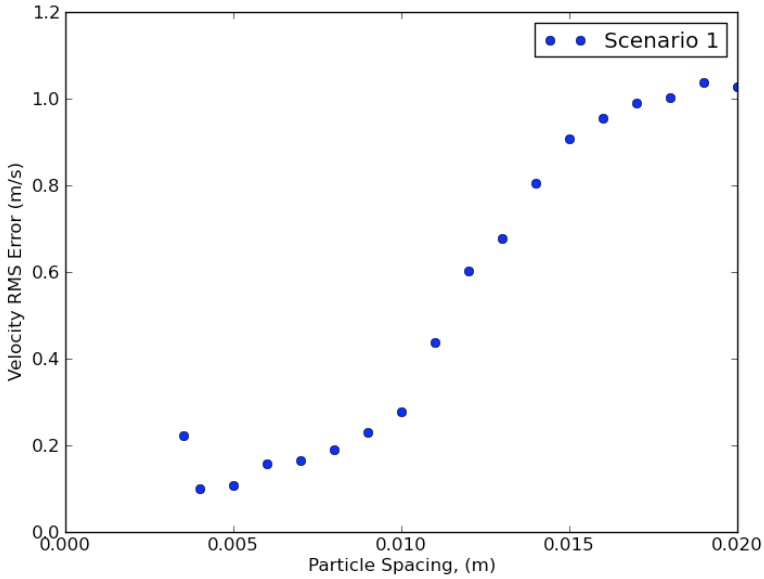

Figure 14. RMS error for velocity value as a function of particle spacing for Scenario 1 (quadratic kernel, SPS term)

To examine the overall velocity values within the range of the experimental results, a root-mean-square (RMS) error analysis was completed comparing the numerical velocity values with the experimental velocity values. As seen in Figure 14 with the RMS Error on the ordinate axis and in Table 9, for Scenario 1, the slope of the RMS error curve is less steep between 4 x 10^{-3}-m and 1.0 x 10^{-2}-m particle spacing than the slope for particle spacings above 1.0 x 10^{-2}-m. The most resolute case of 3.5 x 10^{-3}-m particle spacing counters the general trend of the plot by increasing in RMS error when compared to nearby less resolute cases.

Table 9. RMS error values for velocity for Scenario 1

Scenario 1 (Quadratic Kernel, SPS term)			
Particle Spacing (m)	RMS error (m/s)	Particle Spacing (m)	RMS error (m/s)
3.5×10^{-3}	0.22	1.2×10^{-2}	0.60
4×10^{-3}	0.10	1.3×10^{-2}	0.68
5×10^{-3}	0.11	1.4×10^{-2}	0.80
6×10^{-3}	0.16	1.5×10^{-2}	0.91
7×10^{-3}	0.17	1.6×10^{-2}	0.95
8×10^{-3}	0.19	1.7×10^{-2}	0.99
9×10^{-3}	0.23	1.8×10^{-2}	1.00
1.0×10^{-2}	0.28	1.9×10^{-2}	1.04
1.1×10^{-2}	0.44	2.0×10^{-2}	1.03

Much of this RMS error may be related to the variable error within the experimental results. To determine if experimental variability had much influence in the error of the numerical results, a curve was created by completing a 0.04 s moving time average on the experimental results. The 0.04 s moving time average was chosen to be consistent with the smoothing previously implemented on the numerical results. An RMS analysis comparing the line created from the experimental data to the raw experimental data showed a 0.39 m/s variation in the experimental results. The results for all the particle spacings less than 1.0×10^{-2}-m fall below the 0.39 m/s variation mark, making the actual error for these numerical results indistinguishable from the variation of the experimental results.

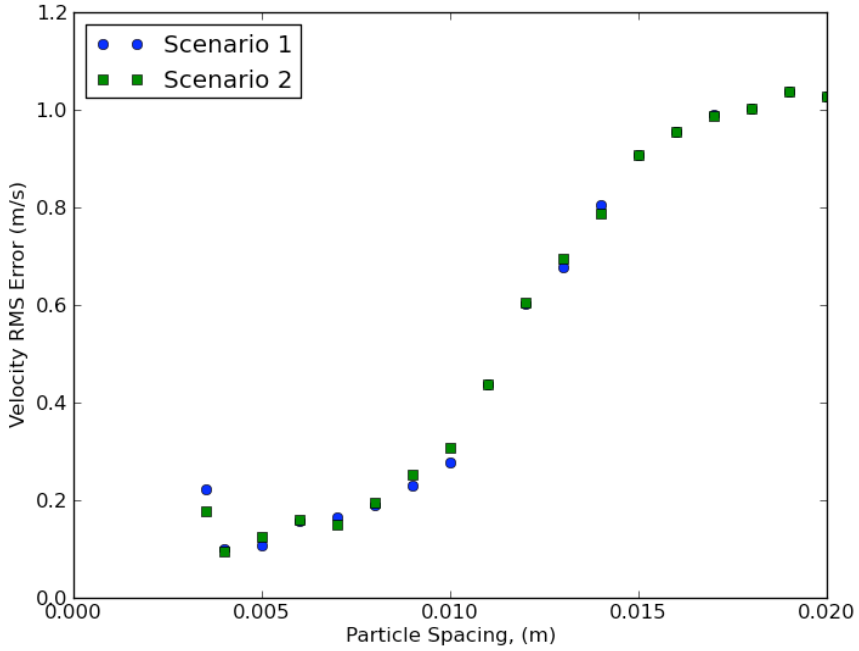

Figure 15. RMS error for velocity value as a function of particle spacing for Scenarios 1 and 2 using quadratic kernel and including or excluding the SPS turbulence term, respectively

Table 10. RMS error values for velocity for Scenario 2

Scenario 2 (Quadratic Kernel, No SPS term)			
Particle Spacing (m)	RMS error (m/s)	Particle Spacing (m)	RMS error (m/s)
3.5×10^{-3}	0.18	1.2×10^{-2}	0.61
4×10^{-3}	0.09	1.3×10^{-2}	0.70
5×10^{-3}	0.13	1.4×10^{-2}	0.79
6×10^{-3}	0.16	1.5×10^{-2}	0.91
7×10^{-3}	0.15	1.6×10^{-2}	0.95
8×10^{-3}	0.20	1.7×10^{-2}	0.99
9×10^{-3}	0.25	1.8×10^{-2}	1.00
1.0×10^{-2}	0.31	1.9×10^{-2}	1.04
1.1×10^{-2}	0.44	2.0×10^{-2}	1.03

Again as seen in Figure 15 and Table 10, the results for both Scenarios 1 and 2 are extremely similar, showing that the inclusion of the SPS turbulence term is not important when concerned with the magnitude of this velocity. The measurement point is not yet affected by the turbulence that will be produced behind the obstruction after these experimental values were taken. This means that, similar to the peak velocity value analysis, there should be little or no difference between the Scenario 1 and 2 cases.

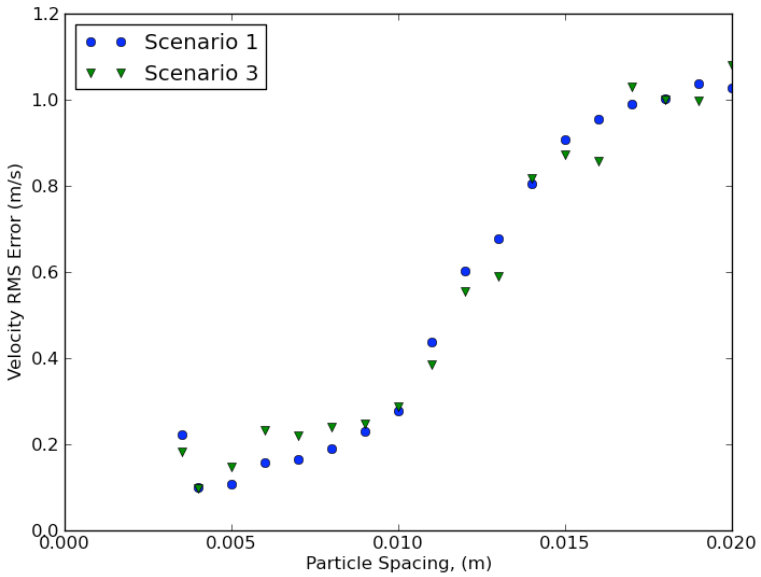

Figure 16. RMS error for velocity value as a function of particle spacing for Scenarios 1 and 3 using the SPS turbulence term and the quadratic or cubic spline kernels, respectively

Table 11. RMS error values for velocity for Scenario 3

Scenario 3 (Cubic Spline Kernel, SPS term)			
Particle Spacing (m)	RMS error (m/s)	Particle Spacing (m)	RMS error (m/s)
3.5×10^{-3}	0.18	1.2×10^{-2}	0.56
4×10^{-3}	0.10	1.3×10^{-2}	0.59
5×10^{-3}	0.15	1.4×10^{-2}	0.82
6×10^{-3}	0.23	1.5×10^{-2}	0.87
7×10^{-3}	0.22	1.6×10^{-2}	0.86
8×10^{-3}	0.24	1.7×10^{-2}	1.03
9×10^{-3}	0.25	1.8×10^{-2}	1.00
1.0×10^{-2}	0.29	1.9×10^{-2}	0.99
1.1×10^{-2}	0.39	2.0×10^{-2}	1.08

Figure 16 compares the RMS error for Scenarios 1 and 3, representing the quadratic and cubic spline kernels, respectively. Additionally, Table 11 shows the values for plotted for Scenario 3. For larger particle spacings, the cubic spline kernel calculation curve tends to be more erratic than the curve for the quadratic calculation. Between 6×10^{-3}-m and 1.0×10^{-2}-m particle spacings, the cubic spline curve tends to be less steep than the quadratic curve. As stated above, RMS errors below 0.39 m/s are within the variation of the experimental data itself and can be considered sufficient. Overall, there are no major differences between the shapes and magnitudes of the values produced by the quadratic and cubic spline kernels.

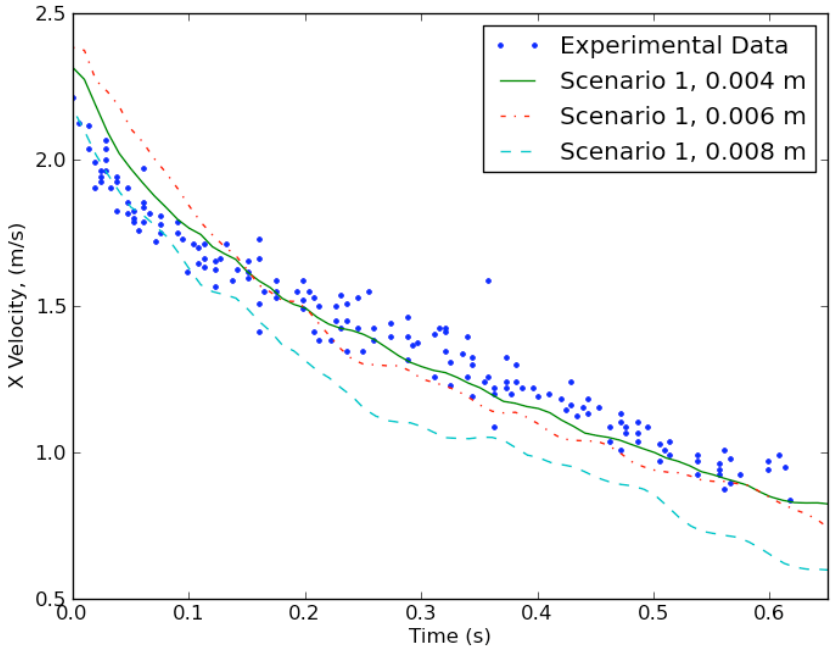

Figure 17. Velocity time series with experimental data for select particle spacings in Scenario 1 (quadratic kernel, SPS term)

Figure 17 shows the velocity time series with the experimental results for select high to medium resolution Scenario 1 cases, including the 4 x 10^{-3}-m, 6 x 10^{-3}-m, and 8 x 10^{-3}-m particle spacings. This figure demonstrates why the previous analysis shows that the RMS error versus particle spacing curve tends to plateau or have a gradual slope at low particle spacings. While each of these three time series intersects with the experimental data at some point, none have the correct peak and slope to more accurately mimic the data. This causes each time series to have similar RMS errors, but different velocity values. The importance of this distinction for GPUSPH cases will vary depending on the primary focus of the model and the level of accuracy required for each specific case.

Comparisons of the numerical results to the available experimental velocity data show that the DamBreak 1 setup can be modeled with some accuracy using particular particle spacings. This statement is especially true for particle spacings near 8×10^{-3}-m when considering peak velocity and overall curve fit. This data also shows that the inclusion of the SPS turbulence term does not affect the velocity results by any significant measure up to 0.6 s into the simulation. The SPS turbulence term is not expected to be significant in this time frame at this location because the flow has not yet felt the effects of turbulence created by flowing around the obstruction.

Comparing the kernel calculations for the data shows that the quadratic kernel produces a more predictable relationship between the numerical data and particle spacing than the erratic correlation between the data and particle spacing with the cubic spline kernel. It is easier to interpolate expected numerical results for the data using the quadratic kernel than for the data using the cubic spline kernel. This is most likely due to the steeper slope of the quadratic weighting kernel that places the most emphasis on the values in the center of the weighting kernel and quickly decreases weight with distance from the center. The cubic spline kernel has a more gradual slope allowing particles within a wider range of radii to have more influence on the velocity value. This larger range of influence contributes greater variation into the weighting function that produces the more erratic correlations seen earlier.

4.2.2 Experimental Force Results Comparisons

In addition to velocity data, the force on the obstruction in the direction of flow was recorded. Using the method to calculate force on the wall discussed in Section 3, the force time series for various Scenario 1 particle spacings is shown in Figure 18. In the figure, time in seconds is recorded on the abscissa and the force value is noted on the ordinate. This figure shows a general trend of increasing accuracy with decreasing particle spacing until the most resolute run in this plot. The 3.5 x 10^{-3}-m particle spacing results have areas of high error that can be attributed to the single precision of the model.

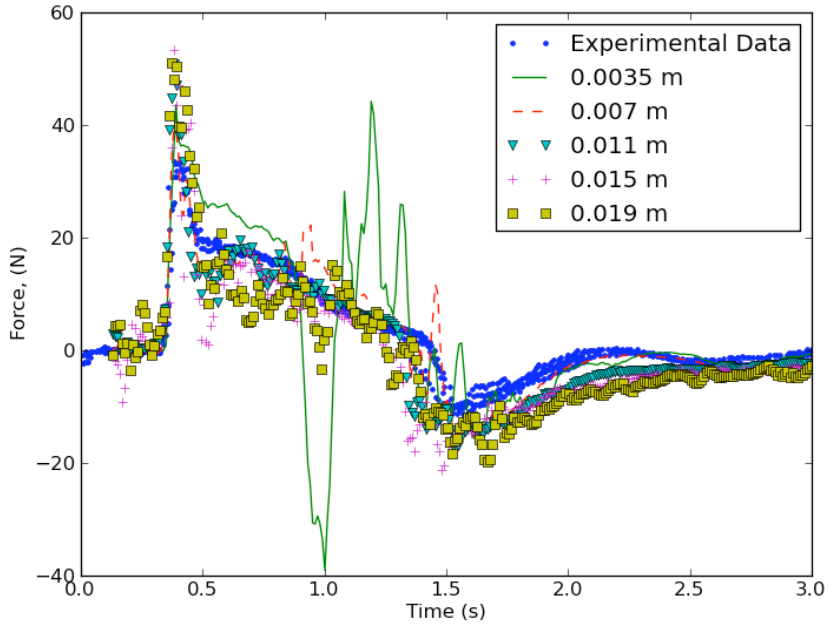

Figure 18. Time series of force in the direction of flow on the obstruction for Scenario 1 (quadratic kernel, SPS term)

To further evaluate this data, a peak force analysis was completed in the same manner as the peak velocity analysis. Figure 19 shows the percent error of the peak force value for the three scenarios with respect to particle spacing. This figure confirms that there is a general trend of more accurate results with smaller particle spacings but the results are not definitive. The percent error varies greatly with respect to scenario and particle spacing. Additionally, the resulting errors are high, with most of the data producing errors of greater than 20%. While this figure seems to show that the GPUSPH model is not adequate to model the force on the obstruction, these issues may not be a failure of the model. Instead, the erroneous data may be caused by the location where the force is being calculated and the influence of the boundary particles of the obstruction.

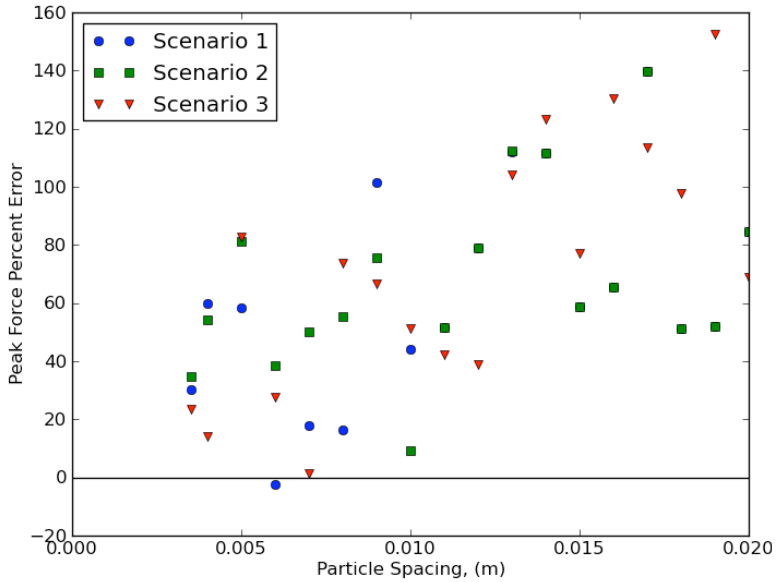

Figure 19. Peak force percent error as a function of particle spacing for Scenarios 1, 2, and 3

Table 12. Peak force values and percent error for Scenarios 1, 2, and 3

Scenario 1 (Quadratic Kernel, SPS term)					
Particle Spacing (m)	Peak Force Value (N)	Percent Error	Particle Spacing (m)	Peak Force Value (N)	Percent Error
3.5×10^{-3}	43.59	30.10	1.2×10^{-2}	59.98	78.99
4×10^{-3}	53.52	59.71	1.3×10^{-2}	71.10	112.18
5×10^{-3}	52.08	58.41	1.4×10^{-2}	70.94	111.71
6×10^{-3}	32.66	-2.53	1.5×10^{-2}	53.24	58.89
7×10^{-3}	39.45	17.72	1.6×10^{-2}	55.46	65.50
8×10^{-3}	39.06	16.55	1.7×10^{-2}	80.34	139.74
9×10^{-3}	67.46	101.32	1.8×10^{-2}	50.63	51.10
1.0×10^{-2}	48.32	44.19	1.9×10^{-2}	50.96	52.07
1.1×10^{-2}	50.76	51.47	2.0×10^{-2}	61.83	84.52
Scenario 2 (Quadratic Kernel, No SPS term)					
Particle Spacing (m)	Peak Force Value (N)	Percent Error	Particle Spacing (m)	Peak Force Value (N)	Percent Error
3.5×10^{-3}	45.12	36.65	1.2×10^{-2}	59.98	78.99
4×10^{-3}	51.65	54.13	1.3×10^{-2}	71.12	112.25
5×10^{-3}	60.78	81.40	1.4×10^{-2}	70.94	111.71
6×10^{-3}	46.38	38.42	1.5×10^{-2}	53.24	58.89
7×10^{-3}	50.35	50.26	1.6×10^{-2}	55.46	65.50
8×10^{-3}	52.10	55.47	1.7×10^{-2}	80.34	139.74
9×10^{-3}	58.82	75.54	1.8×10^{-2}	50.63	51.10
1.0×10^{-2}	36.61	9.25	1.9×10^{-2}	50.96	52.07
1.1×10^{-2}	50.76	51.47	2.0×10^{-2}	61.83	84.52
Scenario 3 (Cubic Spline Kernel, SPS term)					
Particle Spacing (m)	Peak Force Value (N)	Percent Error	Particle Spacing (m)	Peak Force Value (N)	Percent Error
3.5×10^{-3}	41.33	23.35	1.2×10^{-2}	46.50	38.77
4×10^{-3}	38.29	14.28	1.3×10^{-2}	68.42	104.17
5×10^{-3}	61.24	82.75	1.4×10^{-2}	74.76	123.11
6×10^{-3}	42.73	27.53	1.5×10^{-2}	59.35	77.12
7×10^{-3}	34.01	1.48	1.6×10^{-2}	77.22	130.46
8×10^{-3}	58.21	73.71	1.7×10^{-2}	71.49	113.36
9×10^{-3}	55.78	66.46	1.8×10^{-2}	66.28	97.78
1.0×10^{-2}	50.73	51.38	1.9×10^{-2}	84.65	152.63
1.1×10^{-2}	47.62	42.11	2.0×10^{-2}	56.53	68.71

As discussed in Section 2, the boundary particles project an outward force on the fluid to prevent the fluid particles from penetrating the boundaries. This force may be inducing extra artificial pressure on the fluid at the boundary, causing the unusually high force values seen in Table 12 and Figure 19 with the particle spacing on the abscissa and peak force percent error on the ordinate. As shown in the figure, most of the values have percent error values above 20%. To test this artificial induced force phenomenon, the same analysis was completed at 0.06-m in front of and behind the obstruction in the direction of flow. This distance is still close to the obstruction, but it is outside the largest kernel radius length from the boundary for this analysis.

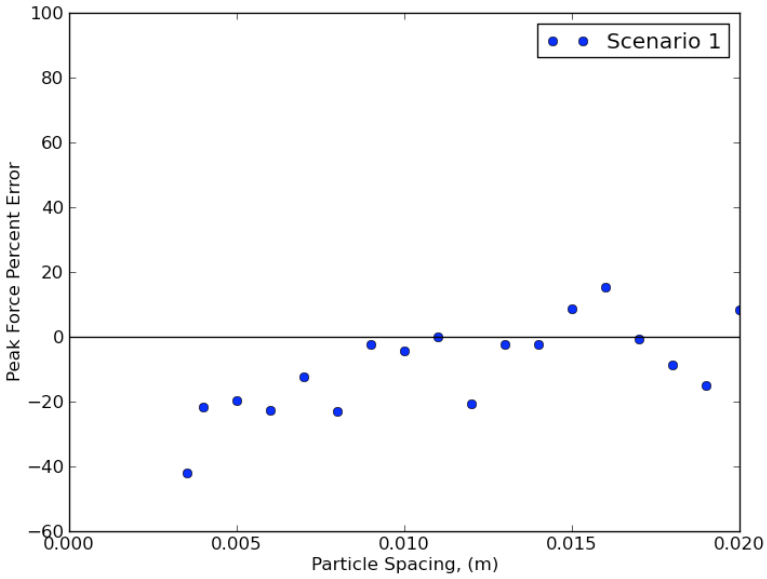

Figure 20. Peak force percent error versus particle spacing for Scenario 1 (quadratic kernel, SPS term) at 0.06 m away from obstruction wall

Table 13. Peak force value and percent error for Scenario 1 at 0.06 m away from obstruction wall

Scenario 1 (Quadratic Kernel, SPS term)					
Particle Spacing (m)	Peak Force Value (N)	Percent Error	Particle Spacing (m)	Peak Force Value (N)	Percent Error
3.5×10^{-3}	19.39	-42.13	1.2×10^{-2}	26.57	-20.71
4×10^{-3}	26.25	-21.66	1.3×10^{-2}	32.70	-2.41
5×10^{-3}	26.93	-19.65	1.4×10^{-2}	32.68	-2.47
6×10^{-3}	25.89	-22.74	1.5×10^{-2}	36.42	8.68
7×10^{-3}	29.42	-12.21	1.6×10^{-2}	38.63	15.30
8×10^{-3}	25.78	-23.07	1.7×10^{-2}	33.26	-0.76
9×10^{-3}	32.74	-2.31	1.8×10^{-2}	30.61	-8.64
1.0×10^{-2}	32.09	-4.24	1.9×10^{-2}	28.47	-15.04
1.1×10^{-2}	33.55	0.13	2.0×10^{-2}	36.30	8.32

Figure 20 and Table 13 shows the peak force percent error as a function of particle spacing for Scenario 1 at 0.06 m away in front of and behind the obstruction in the direction of flow. This Scenario 1 data is much more consistent with the experimental data than the data calculated at the wall, with the largest error being 42.1% compared to approximately 140% in the data calculated at the obstruction. To better discuss the ability of GPUSPH to accurately model flow, the force data analysis is completed using the data calculated away from the obstruction to avoid direct artificial interactions with the boundary particle forces.

Further analysis of Figure 20 shows that there seems to be a general trend of decreasing peak force with decreasing particle spacing in Scenario 1. Even with this trend, the best fitting data tends to occur between particle spacings 9×10^{-3}-m and 1.4×10^{-2}-m. 9 of the 18 cases (50.0%) fall within 10% of the correct peak value and 14 of the

18 (77.8%) cases fall within 20% of the correct value. Excluding the 3.5 x 10^{-3}-m particle spacing, all of the cases in Scenario 1 fall within 23.1% of the experimental peak value. The 3.5 x 10^{-3}-m particle spacing error is 42.1%, which may be attributed to the numerical error due to the single precision capabilities of the model. For particle spacings 8 x 10^{-3}-m and less, the errors are greater and negative, meaning the numerical values underestimate the peak force. These errors are also an indication that the single precision nature of the model may be erroneously rounding values within the calculations, producing less accurate results than cases with slightly larger particle spacings. The results from this figure show that the experimental peak force value can be generated using GPUSPH within an amount of certainty for most of these particle spacings, but the best results occur at particle spacings 9 x 10^{-3}-m and greater.

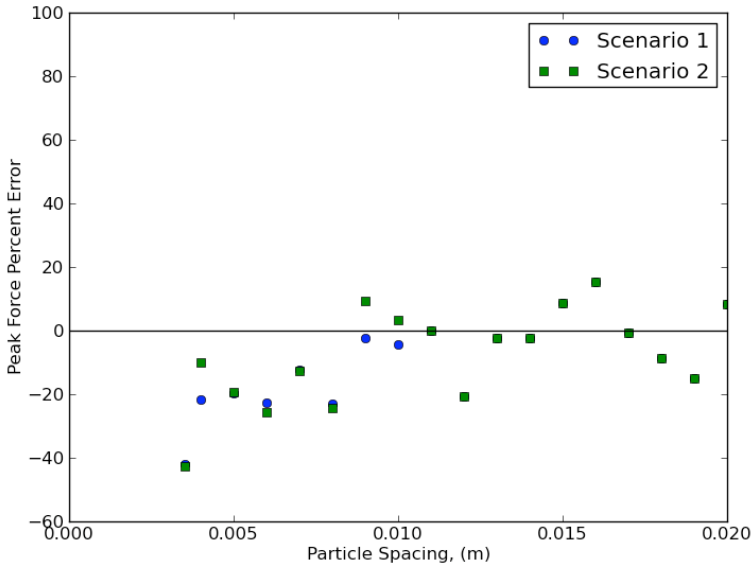

Figure 21. Peak force percent error versus particle spacing for Scenarios 1 and 2 using quadratic kernel and including or excluding the SPS turbulence term, respectively, at 0.06 m away from obstruction wall

Table 14. Peak force values and percent error for Scenario 2

Scenario 2 (Quadratic Kernel, No SPS term)					
Particle Spacing (m)	Peak Force Value (N)	Percent Error	Particle Spacing (m)	Peak Force Value (N)	Percent Error
3.5×10^{-3}	19.23	-42.63	1.2×10^{-2}	26.57	-20.71
4×10^{-3}	30.13	-10.08	1.3×10^{-2}	32.70	-2.41
5×10^{-3}	26.99	-19.47	1.4×10^{-2}	32.68	-2.47
6×10^{-3}	24.90	-25.70	1.5×10^{-2}	36.42	8.68
7×10^{-3}	29.21	-12.82	1.6×10^{-2}	38.63	15.30
8×10^{-3}	25.40	-24.21	1.7×10^{-2}	33.26	-0.76
9×10^{-3}	36.64	9.35	1.8×10^{-2}	30.61	-8.64
1.0×10^{-2}	34.68	3.49	1.9×10^{-2}	28.47	-15.04
1.1×10^{-2}	33.55	0.13	2.0×10^{-2}	36.30	8.32

Figure 21 shows the same analysis for both Scenarios 1 and 2, which vary in the use of the SPS turbulence term. Table 14 shows the peak force values and percent error for Scenario 2. For 15 of the 18 cases (83.3%), the results for Scenarios 1 and 2 are within 3% error of each other. This is particularly true for less resolute cases, where 100% of the cases greater than 1.0×10^{-2}-m particle spacing are identical to two decimal places. All of the results for each particle spacing are within 12% of each other, with the largest differences at 4×10^{-3}-m and 9×10^{-3}-m particle spacings. Similar to the results from the peak velocity analysis, the peak force analysis results show that there is not a significant difference between results from Scenario 1 and results from Scenario 2 at this time in the simulation. Like the peak velocity, the peak force is recorded before any significant turbulence would be expected to have developed in the system, causing the SPS turbulence term to be insignificant at this point.

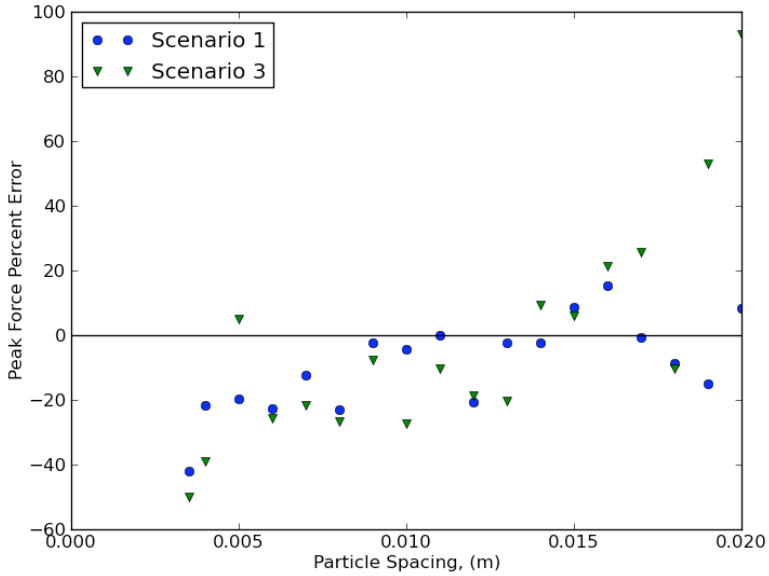

Figure 22. Peak force percent error versus particle spacing for Scenarios 1 and 3 using the SPS turbulence term and the quadratic or cubic spline kernels, respectively, at 0.06 m away from obstruction wall

Table 15. Peak force values and percent error for Scenario 3 at 0.06 m away from obstruction wall

Scenario 3 (Cubic Spline Kernel, SPS term)					
Particle Spacing (m)	Peak Force Value (N)	Percent Error	Particle Spacing (m)	Peak Force Value (N)	Percent Error
3.5×10^{-3}	16.80	-49.86	1.2×10^{-2}	27.30	-18.54
4×10^{-3}	20.42	-39.07	1.3×10^{-2}	26.72	-20.25
5×10^{-3}	35.13	4.84	1.4×10^{-2}	36.61	9.25
6×10^{-3}	24.89	-25.73	1.5×10^{-2}	35.47	5.86
7×10^{-3}	26.25	-21.65	1.6×10^{-2}	40.60	21.17
8×10^{-3}	24.62	-26.54	1.7×10^{-2}	42.06	25.52
9×10^{-3}	30.93	-7.67	1.8×10^{-2}	30.06	-10.29
1.0×10^{-2}	24.40	-27.19	1.9×10^{-2}	51.26	52.98
1.1×10^{-2}	30.07	-10.26	2.0×10^{-2}	64.71	93.12

Figure 22 shows the peak force percent error with particle spacing for Scenarios 1 and 3 at 0.06 m away from the wall. Table 15 shows the peak force values and percent errors for Scenario 3. The results of the cases using the cubic spline weighting kernel in Scenario 3 tend to be more erroneous than the results of the cases using the quadratic kernel in Scenario 1, with the largest error being 93.1% at 2.0×10^{-2}-m particle spacing. Only 4 of the 18 Scenario 3 cases (22.2%) are within 10% of the experimental peak force compared to 50.0% of the cases in Scenario 1. Additionally, only 7 of the 18 Scenario 3 cases (38.9%) are within 20% of the experimental peak force compared to 77.8% of the cases in Scenario 1. Eight of the 18 Scenario 3 cases (44.4%) have more than 25% error, which is much worse than Scenario 1 with one case greater than 25% error. This comparison shows that the implementation of the quadratic kernel is better in predicting the peak force on the obstruction than the cubic spline kernel.

Additionally, an RMS analysis was completed on the force using the entire time series of data. An RMS analysis was completed on a 0.04 s moving time average of the experimental data, producing an error of 1.50 N. This number will be used for comparison with the numerical results.

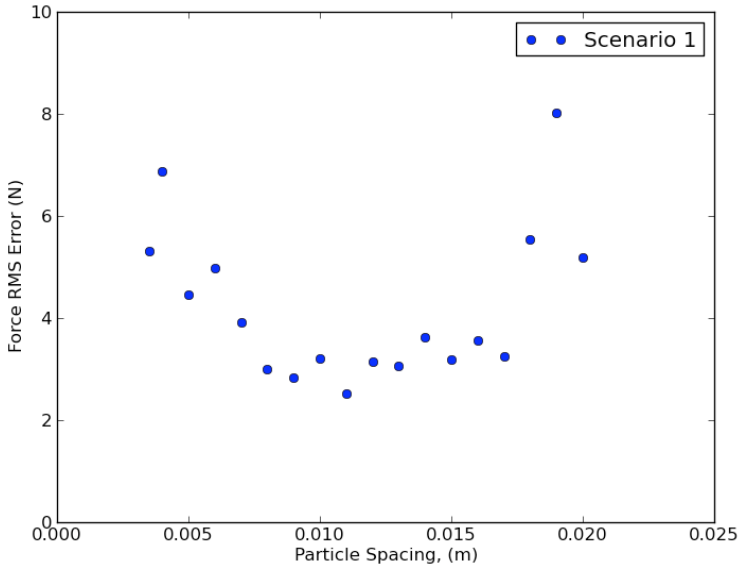

Figure 23. Force RMS analysis error for force data with respect to particle spacing for Scenario 1 (quadratic kernel, SPS term)

Table 16. Force RMS analysis error for force data for Scenario 1

Scenario 1 (Quadratic Kernel, SPS term)			
Particle Spacing (m)	RMS error (N)	Particle Spacing (m)	RMS error (N)
3.5×10^{-3}	5.32	1.2×10^{-2}	3.14
4×10^{-3}	6.88	1.3×10^{-2}	3.06
5×10^{-3}	4.46	1.4×10^{-2}	3.62
6×10^{-3}	4.98	1.5×10^{-2}	3.19
7×10^{-3}	3.92	1.6×10^{-2}	3.56
8×10^{-3}	3.02	1.7×10^{-2}	3.25
9×10^{-3}	2.84	1.8×10^{-2}	5.53
1.0×10^{-2}	3.22	1.9×10^{-2}	8.03
1.1×10^{-2}	2.52	2.0×10^{-2}	5.20

Figure 23 and Table 16 shows the results of the RMS analysis on Scenario 1 with respect to particle spacing. The particle spacing is represented on the abscissa and the

RMS error value is noted on the ordinate axis. The figure shows that the overall error ranges from 2.8 N to 7.4 N, which is higher than the 1.5 N experimental error. The plot shows that particle spacings in the range of 8×10^{-3}-m to 1.7×10^{-2}-m tend to have the most accurate results with 9 of these 10 cases having RMS errors of less than 4.0 N. Viewing the force time series for various Scenario 1 cases in Figure 24 shows that there is a distinct difference in how these errors are achieved for different particle spacings.

The errors are primarily caused by two phenomenon, over or underestimating the peak force and artificial sub-peaks in the time series data. Figure 24 shows the force time series for each of the particle spacings with time on the abscissa and force value on the ordinate axis. As seen in the figure, the general shape of the force time series varies with particle spacing. In Figure 24(a), for the most resolute cases, even after the 0.04 s moving time average has been applied like in the velocity time series analysis, there are many instances of unusually high force values after approximately 0.75 s. These erroneous peaks sometimes have errors as high as 40 N, which produces the high RMS analysis errors. Figure 24 (b) shows the force time series for the median particle spacings, which were the most accurate according to the RMS error analysis. These lines are noticeably less erratic, but they tend to have sustained errors both higher than and lower than the experimental results at different times. The lack of artificial peaks in this data gives it a more accurate fit with the experimental data. Figure 24 (c) shows the force time series for particle spacings 1.3×10^{-2}-m to 1.6×10^{-2}-m, which was the range that had decent results, but not as accurate as the results shown in Figure 24 (b). The error in the results in Figure 24 (c) primarily comes from the underestimation of the

force in the time range of 0.6 s to 0.8 s and the error before the initial peak between 0.2 s to 0.4 s. Finally, the least resolute cases in Figure 24 (d) show that while the lines are more erratic than the lines in Figure 24 (b) and (c), the magnitudes of the spikes tend to stay smaller than the peaks in Figure 24 (a). Additionally, these cases also have a significant error between 2 s to 4 s, which is before the initial peak.

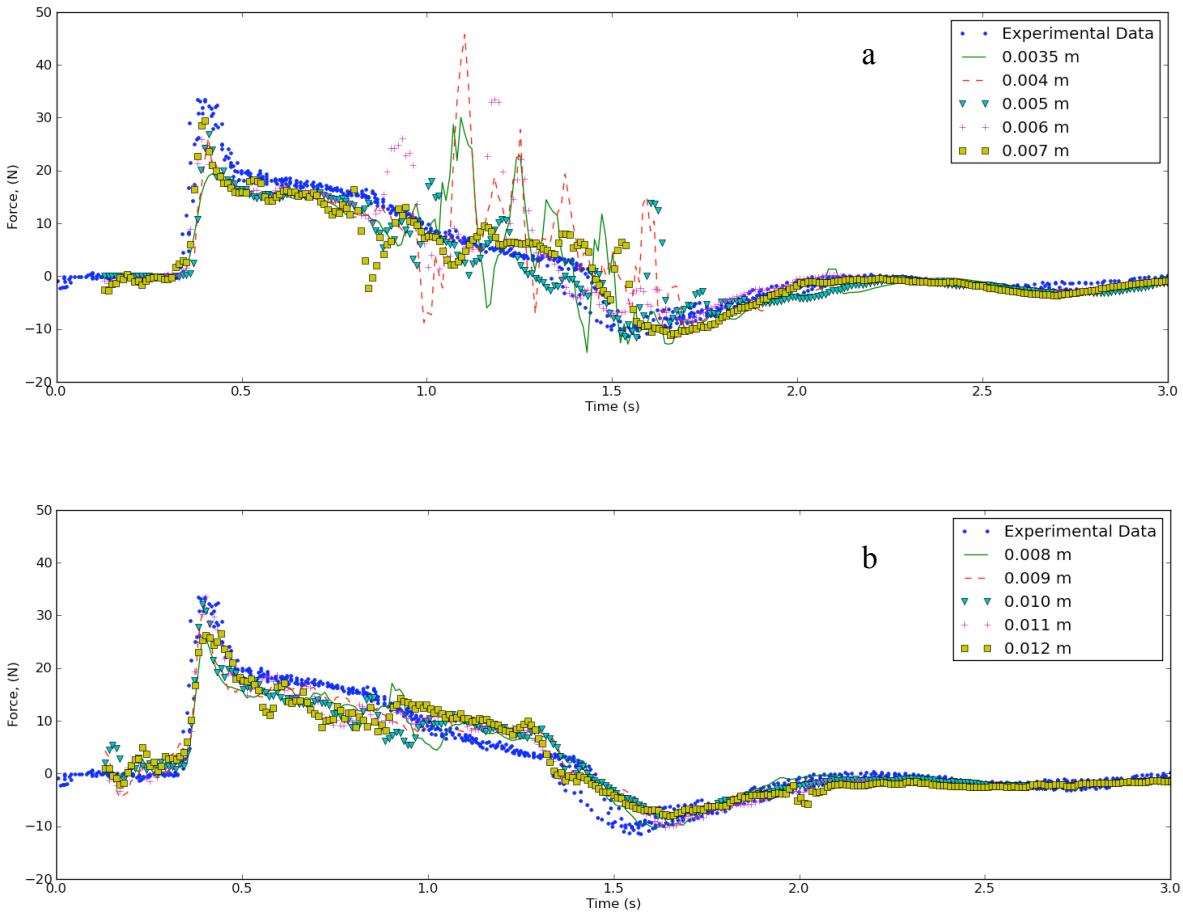

Figure 24. Force time series for Scenario 1 (quadratic kernel, SPS term) after 0.04 s moving average at 0.06 m away from obstruction wall

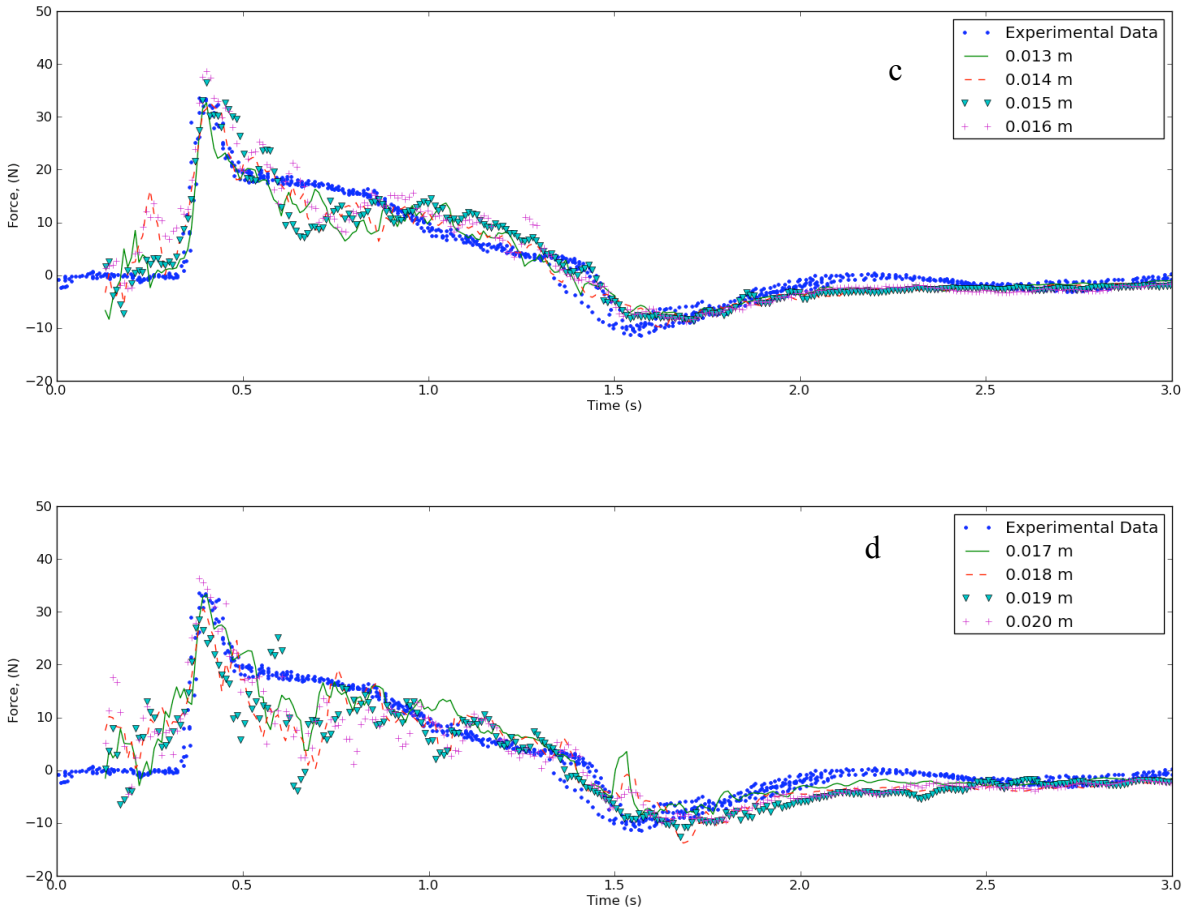

Figure 24. continued

Figure 23 and Figure 24 show that the middle resolutions between particle spacings 8 x 10^{-3}-m and 1.3 x 10^{-2}-m for Scenario 1 have the most accurate results with respect to the force data. The excessive spikes in data found in the most resolute cases are most likely due to the errors in calculation due to the single precision nature of the model. The calculations completed for small particle spacings can often produce values that are too small to be accurately taken into account due to the single precision nature of

the model. The collective result of these rounding errors can produce the artificial spikes found in Figure 24 (a). The larger particle spacings tend to have erroneous results because there are not enough grid points to accurately capture the fluid flow.

Figure 25 shows the RMS analysis error for the cases in Scenarios 1 and 2. Table 17 shows the RMS analysis error values for Scenario 2. The RMS error curve with respect to particle spacing for Scenario 2 follows a similar pattern to the same curve for Scenario 1. The error for the largest and smallest particle spacings tends to be highest, while particle spacings in the middle range tend to plateau at the lower RMS error values. Similar to what has been noted in other analyses, the difference in values between Scenario 1 and Scenario 2 is low, especially for the higher particle spacings in this figure. All Scenarios 1 and 2 cases at 1.0×10^{-2}-m particle spacing and larger produce errors that are with 0.25 N of each other for each particle spacing. 4 of the 5 (80%) cases at 7×10^{-3}-m particle spacing or less have differences of greater than 1.25 N. Based on this figure, the SPS turbulence term tends to have a greater effect at smaller particle spacings than at larger particle spacings, but viewing the force time series will explain why this trend occurs.

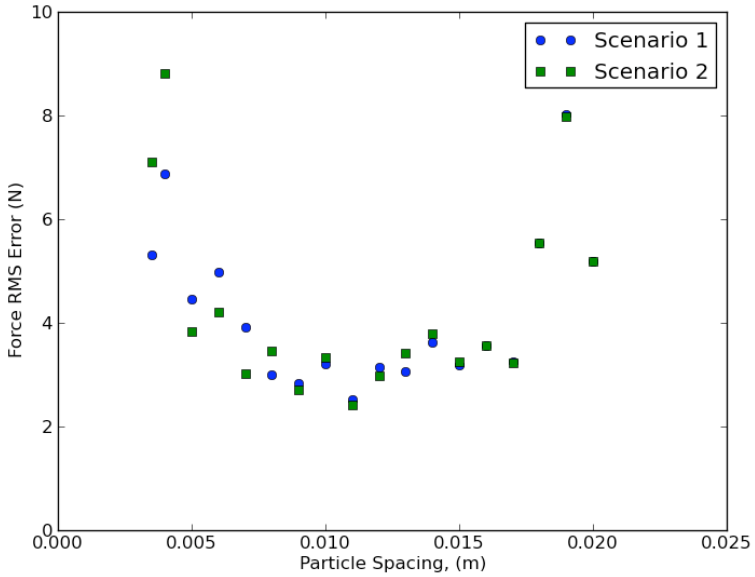

Figure 25. RMS analysis error for force data with respect to particle spacing for Scenarios 1 and 2 using quadratic kernel and including or excluding the SPS turbulence term, respectively

Table 17. RMS error for force data for Scenario 2

Scenario 2 (Quadratic Kernel, No SPS term)			
Particle Spacing (m)	RMS error (N)	Particle Spacing (m)	RMS error (N)
3.5×10^{-3}	7.10	1.2×10^{-2}	2.97
4×10^{-3}	8.81	1.3×10^{-2}	3.41
5×10^{-3}	3.84	1.4×10^{-2}	3.78
6×10^{-3}	4.20	1.5×10^{-2}	3.25
7×10^{-3}	3.02	1.6×10^{-2}	3.56
8×10^{-3}	3.46	1.7×10^{-2}	3.23
9×10^{-3}	2.70	1.8×10^{-2}	5.53
1.0×10^{-2}	3.33	1.9×10^{-2}	7.98
1.1×10^{-2}	2.42	2.0×10^{-2}	5.20

Figure 26 shows the force time series for each of the Scenario 2 locations after the 0.04 s moving time average for the data taken at 0.06 m away from the obstruction.

Figure 26 (a) shows an interesting difference when compared with Figure 24 (a). While both scenarios show high artificial spikes in the data for particle spacings 3.5 x 10^{-3}-m and 4 x 10^{-3}-m, the peaks for the 5 x 10^{-3}-m, 6 x 10^{-3}-m, and 7 x 10^{-3}-m particle spacing cases are significantly subdued in Scenario 2. This shows that for these three cases, the SPS turbulence term is increasing the erratic behavior of the model and producing more erroneous results. Additionally, for the 3.5 x 10^{-3}-m and 4 x 10^{-3}-m particle spacings, the results show that while the magnitude of the artificial spikes in Scenario 2 are slightly less, the spikes are sustained longer without crossing the experimental values line. This is evidenced by the smaller spikes within the larger spike structure for the 3.5 x 10^{-3}-m case in the range of 1.25 s to 1.35 s. A similar trend occurs for the 4 x 10^{-3}-m particle spacing case.

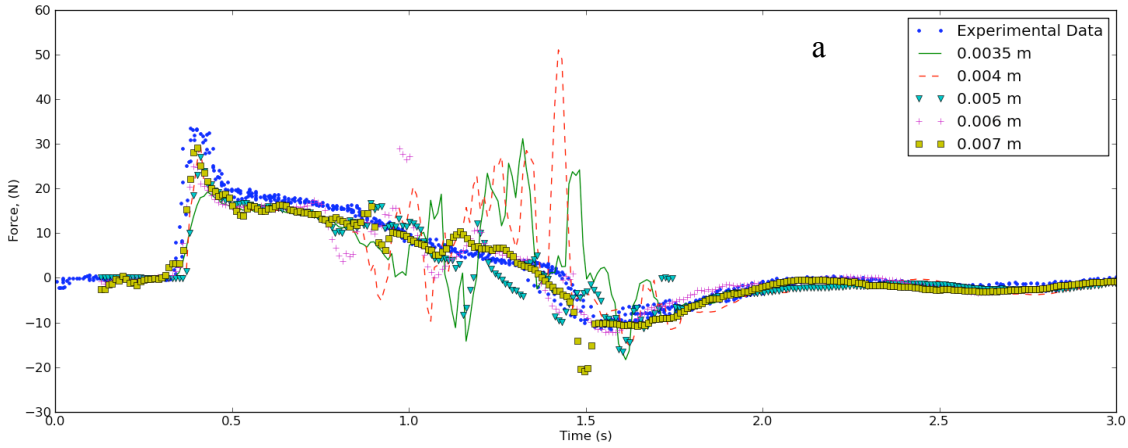

Figure 26. Force time series for Scenario 2 (quadratic kernel, no SPS turbulence term) after 0.04 s moving average at 0.06 m away from obstruction

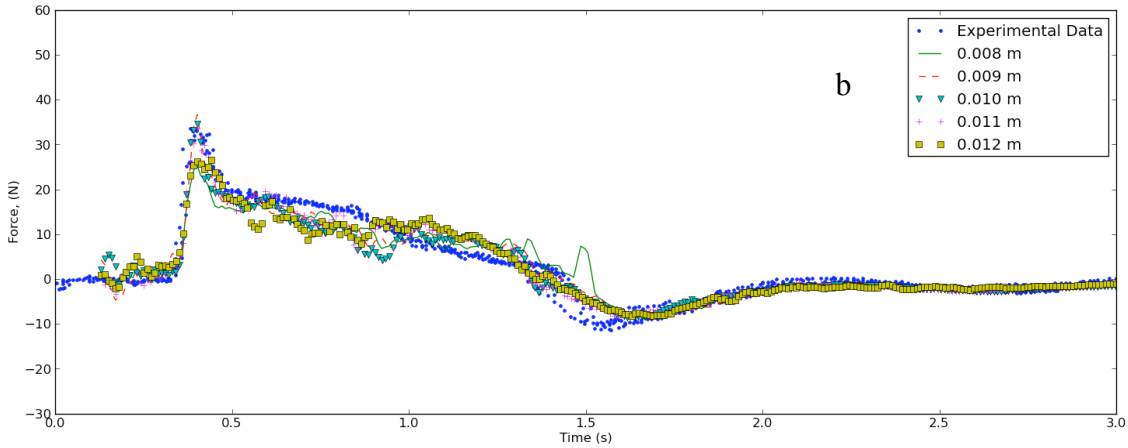

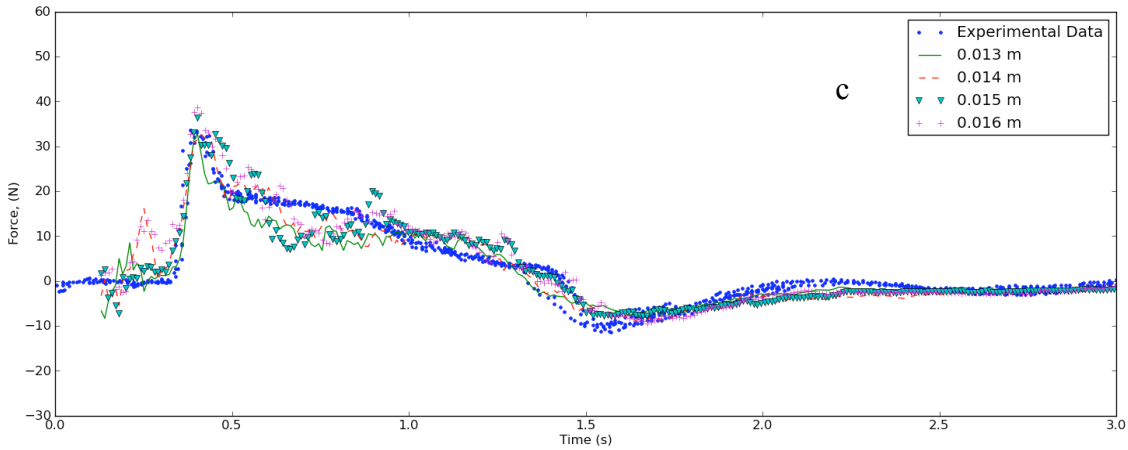

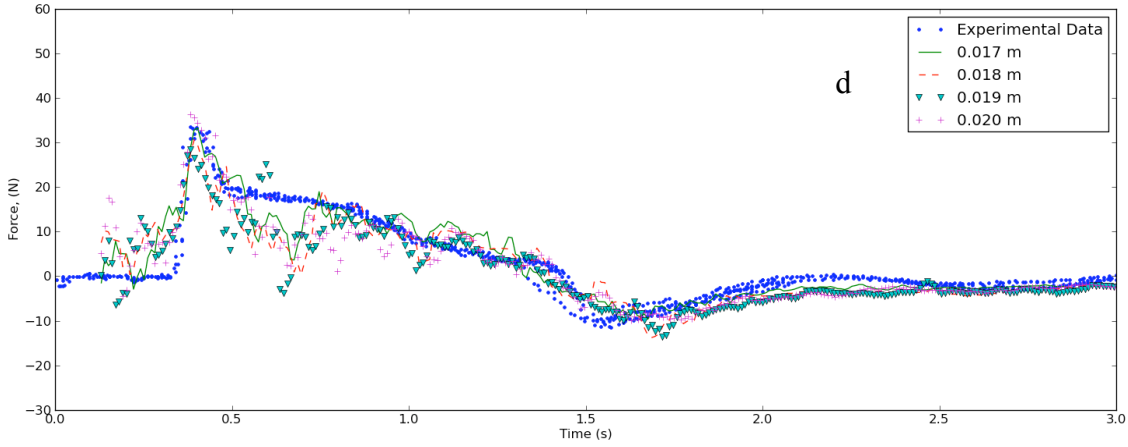

Figure 26. continued

Also important to note when viewing these time series is that the main differences between the Scenario 1 and Scenario 2 cases tend to occur in the time range after the flow has reached the back side of the obstruction. This shows that the SPS turbulence term primarily affects the flow when it is deforming around and behind the obstruction. This result is expected since there is not much turbulence relative to the speed and size of the bore before it reaches the obstruction. The difference between Scenarios 1 and 2 has not been seen yet in the previous analysis in this paper because the analysis was completed on data collected in front of the obstruction including the velocity time series and the peak force values.

While the most resolute cases showcase the influence of the SPS turbulence term, the magnitude of this influence is not seen in the other cases. When comparing Figure 24 (b) and Figure 26 (b), the Scenario 1 and Scenario 2 time series are similar except for a few additional spikes in the Scenario 2 8 x 10^{-3}-m particle spacing case. Additionally, the particle spacings represented in Figure 24 (c) and (d) and Figure 26 (c) and (d) show similar force time series, which corresponds to the results noted in Figure 25 that these cases have similar RMS analysis error results. The SPS turbulence term does not influence these cases much because there were no major artificial spikes in the data to exaggerate.

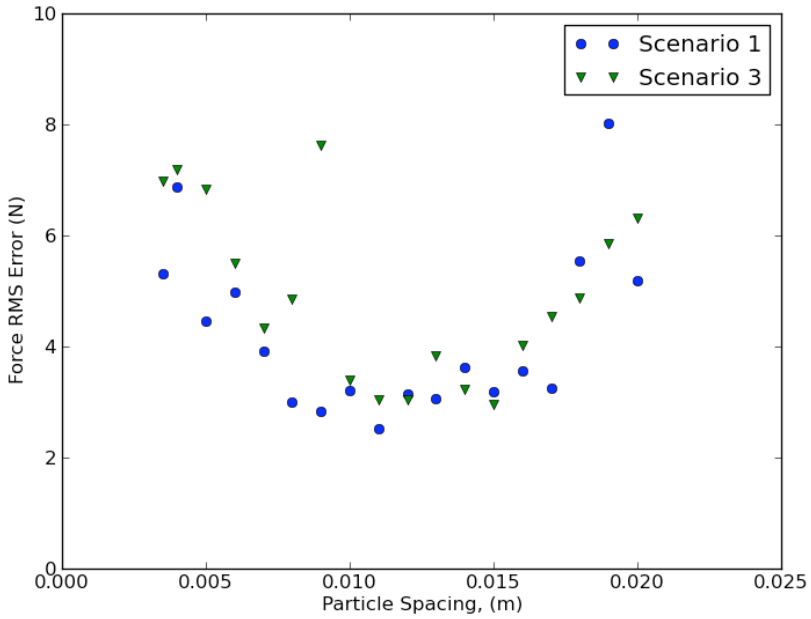

Figure 27. RMS analysis error for force data with respect to particle spacing for Scenarios 1 and 3 using the SPS turbulence term and the quadratic or cubic spline kernels, respectively

Table 18. RMS analysis error for force data for Scenario 3

Scenario 3 (Cubic Spline Kernel, SPS term)			
Particle Spacing (m)	RMS error (N)	Particle Spacing (m)	RMS error (N)
3.5×10^{-3}	6.98	1.2×10^{-2}	3.03
4×10^{-3}	7.19	1.3×10^{-2}	3.84
5×10^{-3}	6.82	1.4×10^{-2}	3.23
6×10^{-3}	5.50	1.5×10^{-2}	2.95
7×10^{-3}	4.33	1.6×10^{-2}	4.02
8×10^{-3}	4.85	1.7×10^{-2}	4.54
9×10^{-3}	7.63	1.8×10^{-2}	4.87
1.0×10^{-2}	3.39	1.9×10^{-2}	5.86
1.1×10^{-2}	3.04	2.0×10^{-2}	6.30

Figure 27 shows the RMS analysis error for Scenarios 1 and 3. Table 18 shows the RMS analysis error results for Scenario 3. Eleven of the 18 particle spacings

(61.1%) produce errors within 0.5 N of each other. The largest differences occur at particle spacings 5 x 10^{-3}-m, 9 x 10^{-3}-m, and 1.9 x 10^{-2}-m, where the RMS error differences between Scenarios 1 and 3 are greater than 2 N. The spacings of these largest differences are interesting in that they include high, medium, and low resolution cases. Comparing the force time series of Scenario 3 in Figure 28 to the time series of Scenario 1 in Figure 24 shows why there are these large differences at seemingly random particle spacings.

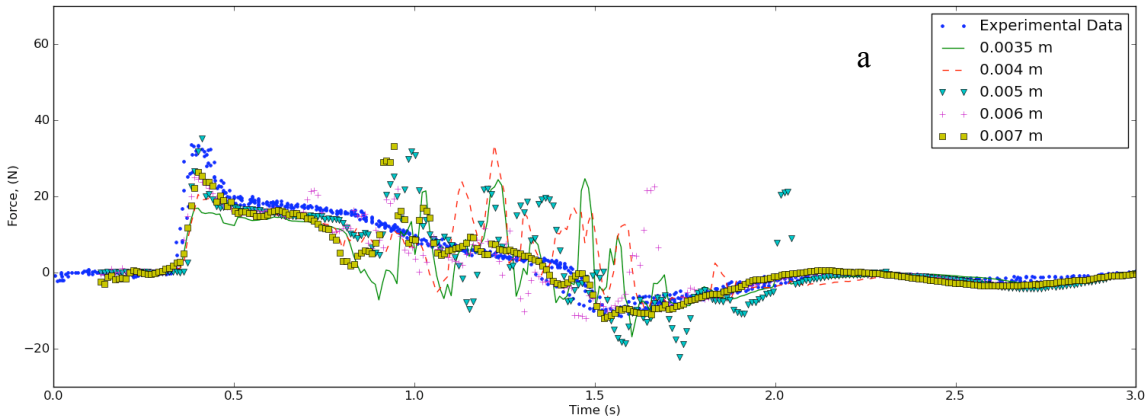

Figure 28. Force time series for Scenario 3 (cubic spline kernel, SPS turbulence term) after 0.04 s moving average at 0.06 m away from obstruction

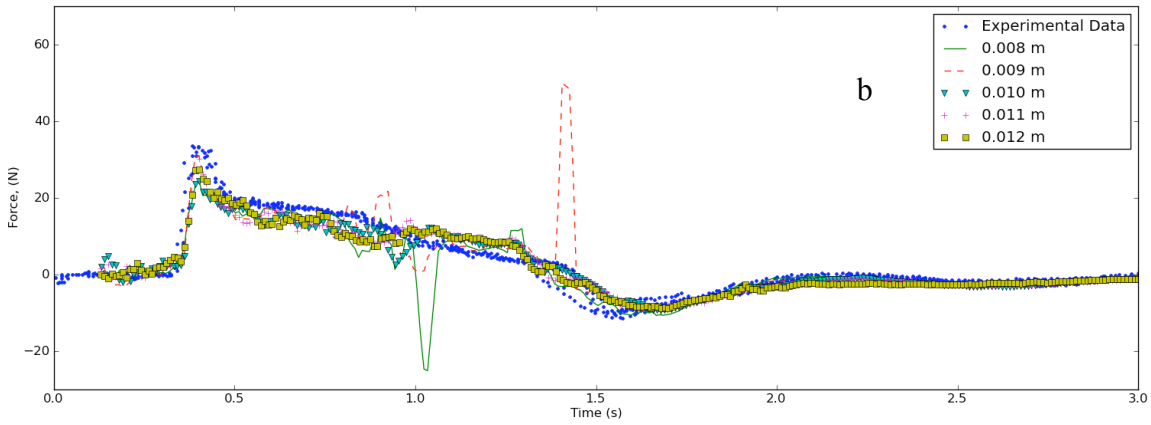

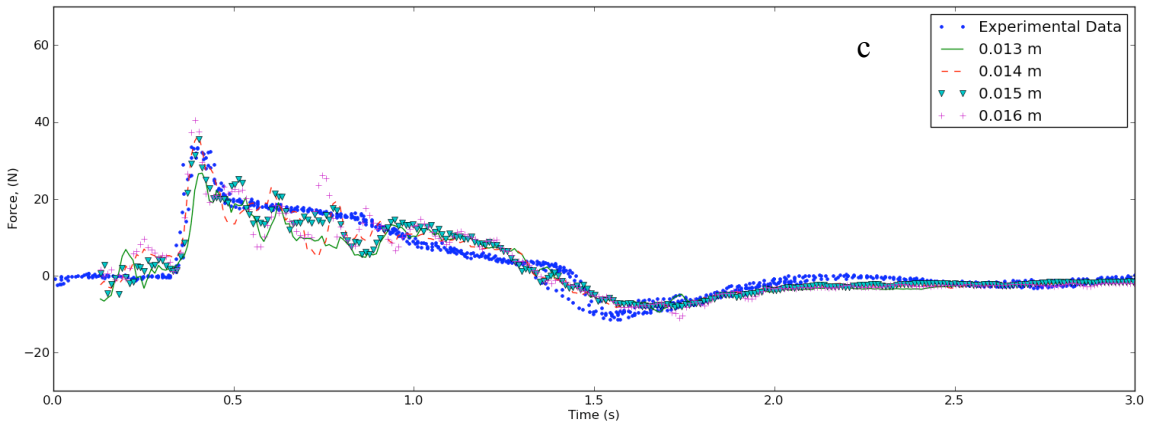

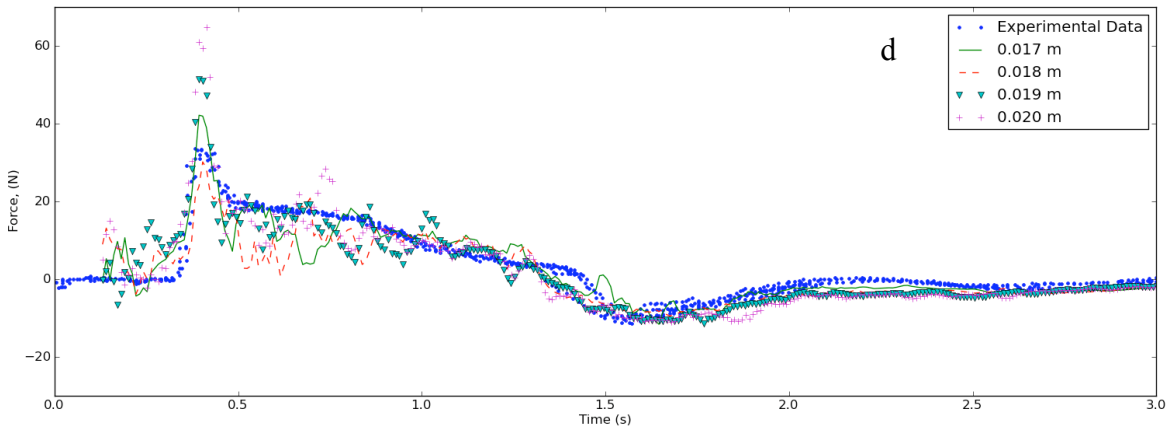

Figure 28. continued

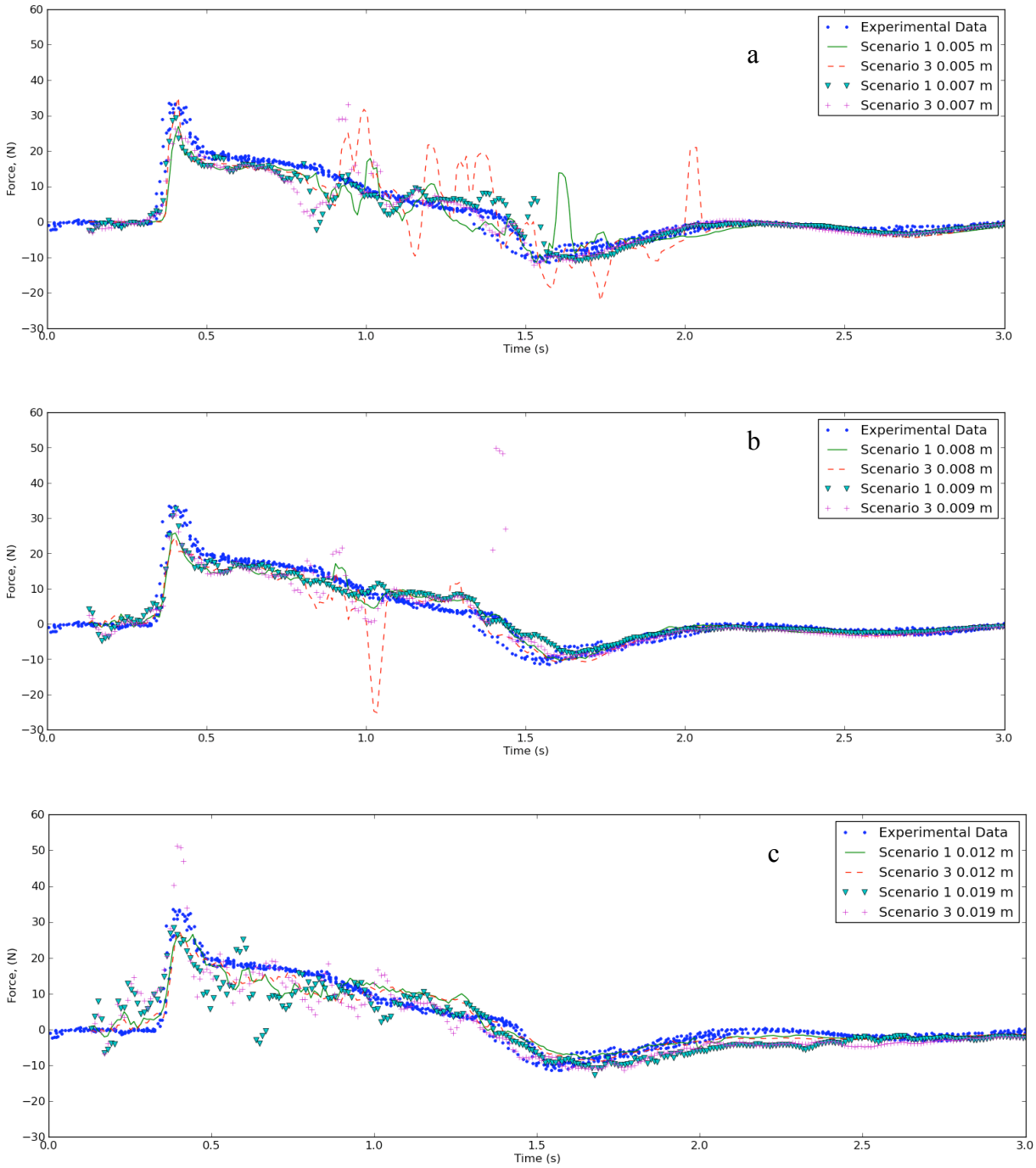

Figure 29. Force time series for selected Scenario 1 and Scenario 3 cases, using the SPS turbulence term and the quadratic or cubic spline kernel, respectively

Comparing Figure 24 (a) and Figure 28 (a) shows that for the most resolute cases, Scenario 1 tends to better capture the shape and magnitude of the peak force. This statement is particularly true for particle spacing 7 x 10^{-3}-m, as compared in Figure 29 (a). In the time when the flow is wrapping around the obstruction and causing artificial spikes in the data, the magnitude of these spikes tends to be decreased in Scenario 3 while the number of spikes does not significantly change. Another difference is that Scenario 3 tends to continue having more erratic behavior after approximately 1.7 s that is not present in the Scenario 1 results. Figure 24 (b) and Figure 28 (b) show that for median resolute cases, Scenario 3 tends to produce data that better follows the experimental data, which is especially true in particle spacing 1.2 x 10^{-2}-m, as shown in Figure 29 (c). The main issue with the data in Scenario 3 is the seemingly random spikes of force as shown in the 8 x 10^{-3}-m and 9 x 10^{-3}-m particle spacing cases in Figure 29 (b). Figure 24 (c) and Figure 28 (c) also show that Scenario 1 has a better shape fit to the experimental data near the peak velocity, while Scenario 3 has a better shape just before and after the peak velocity. When comparing Figure 24 (d) and Figure 28 (d), the Scenario 3 peak force results are much higher, but the rest of the time series contains errors that are comparable between the two scenarios, except for particle spacing 1.9 x 10^{-2}-m as discussed earlier.

The overall comparison between Scenarios 1 and 3 show that overall the cubic spline kernel tends to subdue the artificial spiked values in the numerical results, except for random large spikes such as in particle spacing 9 x 10^{-3}-m or in the 5 x 10^{-3}-m spacing near 2.0 s. These large spikes can be explained as they relate to the weighting

function kernel. Because the cubic spline method decreases weight more slowly from the center of the kernel, one rogue high value will have a less influence on the particle value because it will be averaged with other values in the area. If there is a particle with an artificially high value at or near the center of the kernel, the value of the quantity at that particle point will spike unnaturally high. These unnaturally high values will then be incorporated into other calculations, such as the force discussed here.

4.2.3 Non-experimental Data Comparisons

In addition to the analysis completed with the existing experimental data, there are other characteristics of the flow that can be explored and compared with respect to particle spacing, weighting function kernel, and inclusion of the SPS term. For this section of the analysis, the time will not be adjusted, as it was previously to match the peaks of the experimental and numerical data. By not adjusting the time, bore speed and time for return flow to initiate can be compared in addition to comparing peak velocity and other flow characteristics throughout the system.

The velocity was calculated at each time step in the center of the pathway between the obstruction and the sidewall at system coordinates of (0.96 m, 0.49 m, 0.026 m), noted as location D in Figure 7. The velocity data at this position provides information to compare concerning the initial flow, return flow, and the time difference between the initial and return flow. After the 0.04 s moving time average was applied to the velocity time series, the value and time of maximum velocity and the value and time of minimum velocity, representing the maximum return flow velocity, were recorded.

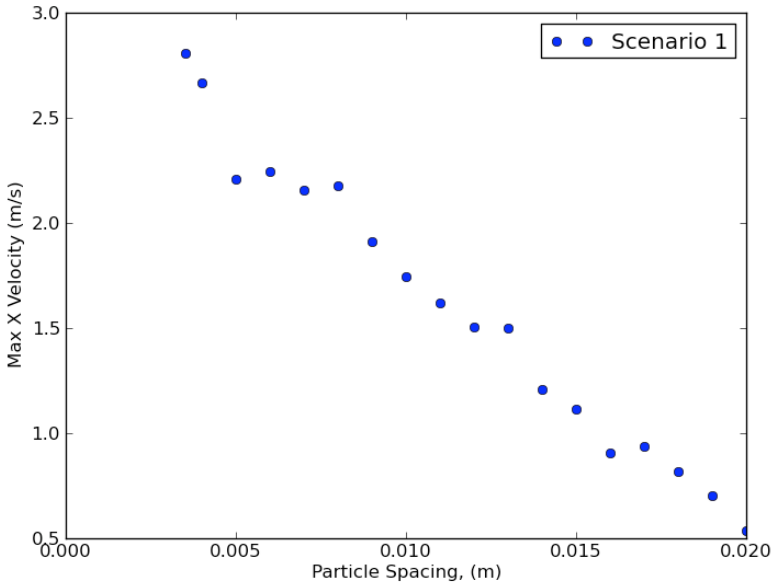

Figure 30. Maximum velocity at location D for Scenario 1 (quadratic kernel, SPS term) as a function of particle spacing

Table 19. Maximum velocity values at location D for Scenario 1

Scenario 1 (Quadratic Kernel, SPS term)			
Particle Spacing (m)	Maximum Velocity (m/s)	Particle Spacing (m)	Maximum Velocity (m/s)
3.5×10^{-3}	2.81	1.2×10^{-2}	1.51
4×10^{-3}	2.67	1.3×10^{-2}	1.50
5×10^{-3}	2.21	1.4×10^{-2}	1.21
6×10^{-3}	2.24	1.5×10^{-2}	1.12
7×10^{-3}	2.15	1.6×10^{-2}	0.90
8×10^{-3}	2.18	1.7×10^{-2}	0.94
9×10^{-3}	1.91	1.8×10^{-2}	0.82
1.0×10^{-2}	1.74	1.9×10^{-2}	0.70
1.1×10^{-2}	1.62	2.0×10^{-2}	0.54

The maximum forward velocity was plotted against particle spacing in Figure 30 and listed in Table 19. The figure notes the particle spacing on the abscissa and the maximum velocity in the direction of flow of the ordinate. The velocity trend shows a clear decrease in maximum forward velocity with increasing particle spacing. The distinct decrease may be related to the extra boundary effects on the flow due to the narrow path between the obstruction and the sidewall. When a larger particle spacing is implemented, the kernel radius of each particle is larger. This means that the direct boundary force presence is incorporated into particle calculations further from the walls for larger particle spacings, which could slow the flow. Another reason the flows could be slower for greater particle spacings is that these flows might not have enough of the moving particle grid points to accurately capture the flow structure through the channel. Figure 31, Figure 32, Table 20, and Table 21. Maximum velocity at location D for Scenario 3 show similar trends for Scenarios 2 and 3.

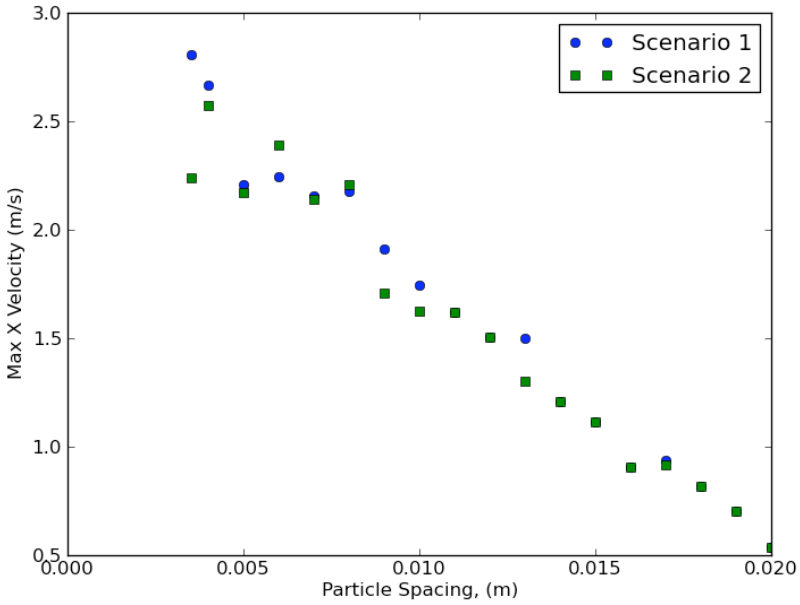

Figure 31. Maximum velocity at location D for Scenarios 1 and 2 using quadratic kernel and including or excluding the SPS turbulence term, respectively, as a function of particle spacing

Table 20. Maximum velocity at location D for Scenario 2

Scenario 2 (Quadratic Kernel, No SPS term)			
Particle Spacing (m)	Maximum Velocity (m/s)	Particle Spacing (m)	Maximum Velocity (m/s)
3.5×10^{-3}	2.24	1.2×10^{-2}	1.51
4×10^{-3}	2.57	1.3×10^{-2}	1.30
5×10^{-3}	2.17	1.4×10^{-2}	1.21
6×10^{-3}	2.39	1.5×10^{-2}	1.12
7×10^{-3}	2.14	1.6×10^{-2}	0.90
8×10^{-3}	2.21	1.7×10^{-2}	0.92
9×10^{-3}	1.71	1.8×10^{-2}	0.82
1.0×10^{-2}	1.63	1.9×10^{-2}	0.70
1.1×10^{-2}	1.62	2.0×10^{-2}	0.54

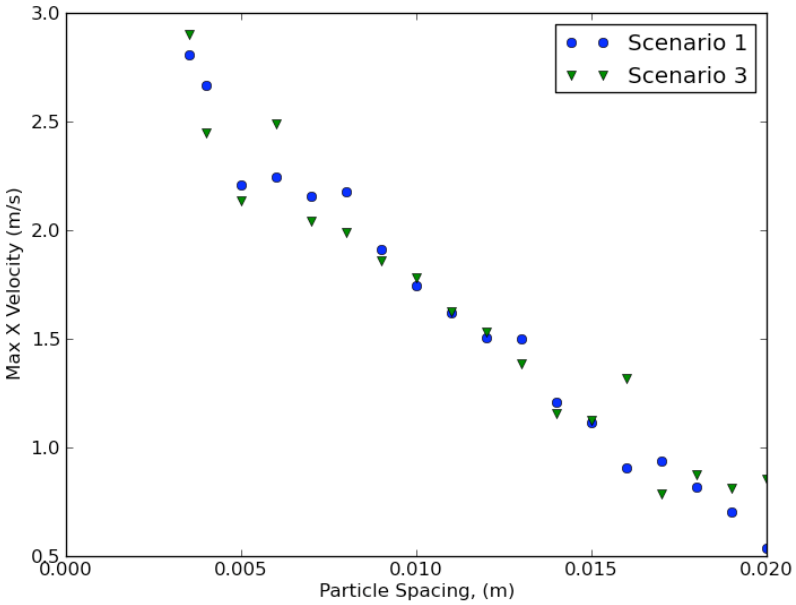

Figure 32. Maximum velocity at location D for Scenarios 1 and 3 using the SPS turbulence term and the quadratic or cubic spline kernels, respectively, as a function of particle spacing

Table 21. Maximum velocity at location D for Scenario 3

Scenario 3 (Cubic Spline Kernel, SPS term)			
Particle Spacing (m)	Maximum Velocity (m/s)	Particle Spacing (m)	Maximum Velocity (m/s)
3.5×10^{-3}	2.90	1.2×10^{-2}	1.53
4×10^{-3}	2.45	1.3×10^{-2}	1.39
5×10^{-3}	2.14	1.4×10^{-2}	1.16
6×10^{-3}	2.49	1.5×10^{-2}	1.13
7×10^{-3}	2.04	1.6×10^{-2}	1.32
8×10^{-3}	1.99	1.7×10^{-2}	0.79
9×10^{-3}	1.86	1.8×10^{-2}	0.87
1.0×10^{-2}	1.78	1.9×10^{-2}	0.81
1.1×10^{-2}	1.63	2.0×10^{-2}	0.85

The time difference was calculated and plotted versus particle spacing in Figure 33 and Table 22 for Scenario 1. The figure contains the particle spacing on the abscissa and the time difference in seconds on the ordinate. While there is a distinct trend of a faster return flow for smaller particle spacings, this trend is not as smooth as previous trends discussed concerning particle spacing. One familiar trend that does appear in this data is the negative slope line when moving from 3.5×10^{-3}-m to 4×10^{-3}-m and 5×10^{-3}-m before increasing to a plateau in the range of 7×10^{-3}-m and 9×10^{-3}-m, if the extraneous 8×10^{-3}-m point is not included. This trend is similar to the peak velocity curve and RMS error analysis when comparing numerical results to the available experimental velocity data. The results in this figure at lower resolutions tend to be erratic, showing that these particle spacings may be too large to provide meaningful results and that there are not enough particles in the system to fully capture the more turbulent flow behind the obstruction even with the inclusion of the SPS turbulence term.

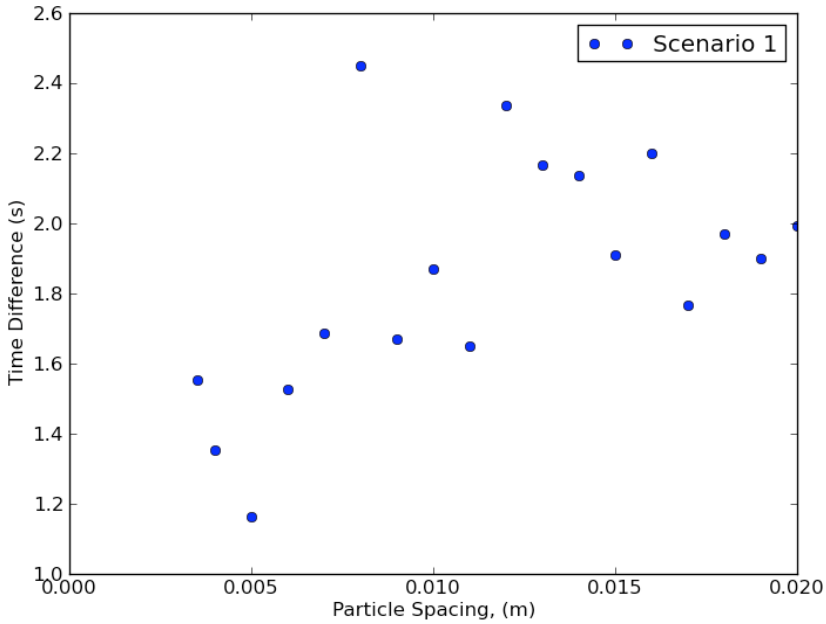

Figure 33. Time difference between maximum forward flow and maximum return flow at location D for Scenario 1 (quadratic kernel, SPS term) versus particle spacing

Table 22. Time difference between maximum forward and return flows at location D for Scenario 1

Scenario 1 (Quadratic Kernel, SPS term)			
Particle Spacing (m)	Time Difference (s)	Particle Spacing (m)	Time Difference (s)
3.5×10^{-3}	1.55	1.2×10^{-2}	2.34
4×10^{-3}	1.35	1.3×10^{-2}	2.17
5×10^{-3}	1.16	1.4×10^{-2}	2.14
6×10^{-3}	1.53	1.5×10^{-2}	1.91
7×10^{-3}	1.69	1.6×10^{-2}	2.20
8×10^{-3}	2.45	1.7×10^{-2}	1.77
9×10^{-3}	1.67	1.8×10^{-2}	1.97
1.0×10^{-2}	1.87	1.9×10^{-2}	1.90
1.1×10^{-2}	1.65	2.0×10^{-2}	1.99

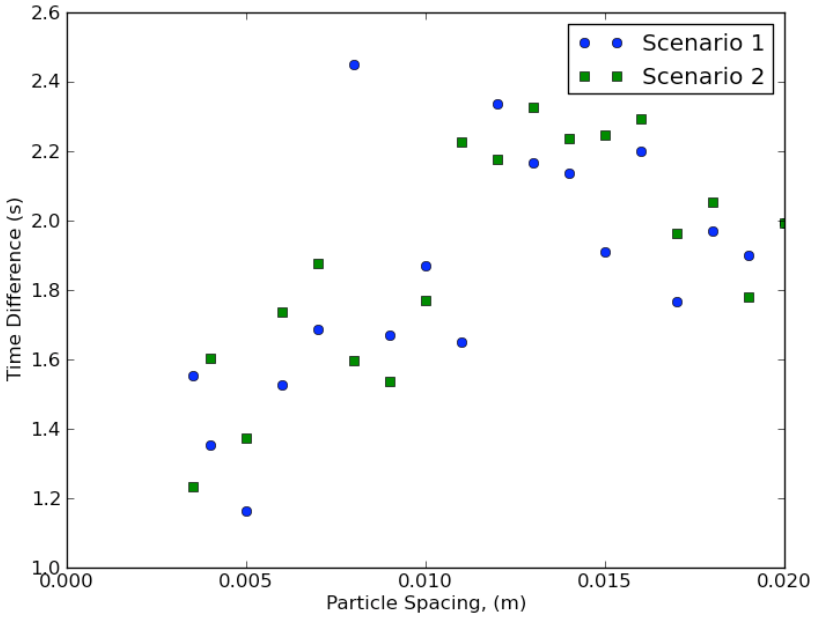

Figure 34. Time difference between maximum forward flow and maximum return flow at location D for Scenarios 1 and 2 using quadratic kernel and including or excluding the SPS turbulence term, respectively, versus particle spacing

Table 23. Time difference between maximum forward and return flows at location D for Scenario 2

Scenario 2 (Quadratic Kernel, No SPS term)			
Particle Spacing (m)	Time Difference (s)	Particle Spacing (m)	Time Difference (s)
3.5×10^{-3}	1.23	1.2×10^{-2}	2.18
4×10^{-3}	1.60	1.3×10^{-2}	2.33
5×10^{-3}	1.37	1.4×10^{-2}	2.24
6×10^{-3}	1.74	1.5×10^{-2}	2.25
7×10^{-3}	1.88	1.6×10^{-2}	2.29
8×10^{-3}	1.60	1.7×10^{-2}	1.96
9×10^{-3}	1.54	1.8×10^{-2}	2.05
1.0×10^{-2}	1.77	1.9×10^{-2}	1.78
1.1×10^{-2}	2.23	2.0×10^{-2}	1.99

Figure 34 shows the same plot comparing Scenarios 1 and 2 and Table 23 contains the time difference values for Scenario 2. For particle spacings 1.1 x 10^{-2}-m to 1.8 x 10^{-2}-m, the result for Scenario 1, which includes the SPS turbulence term, are lower than the results for Scenario 2, except for particle spacing 1.2 x 10^{-2}-m. This may be an indication that the SPS turbulence term is influencing the highly turbulent flow behind the obstruction. While there is no experimental data to compare to these results, it is assumed that the data in the range of particle spacings less than 1.0 x 10^{-2}-m are more accurate than the data in the range of particle spacings above 1.0 x 10^{-2}-m. This assumption is based on the previously discussed results on the comparisons of velocity and force data in the system to experimental results. If it is assumed that the data in the range of spacings less than 1.0 x 10^{-2}-m is relatively correct, then the data for larger particle spacings in Scenario 1 is more accurate than the data in Scenario 2. The SPS term is including the turbulence at the sub-particle scale in the momentum calculation to provide relatively more accurate numerical results.

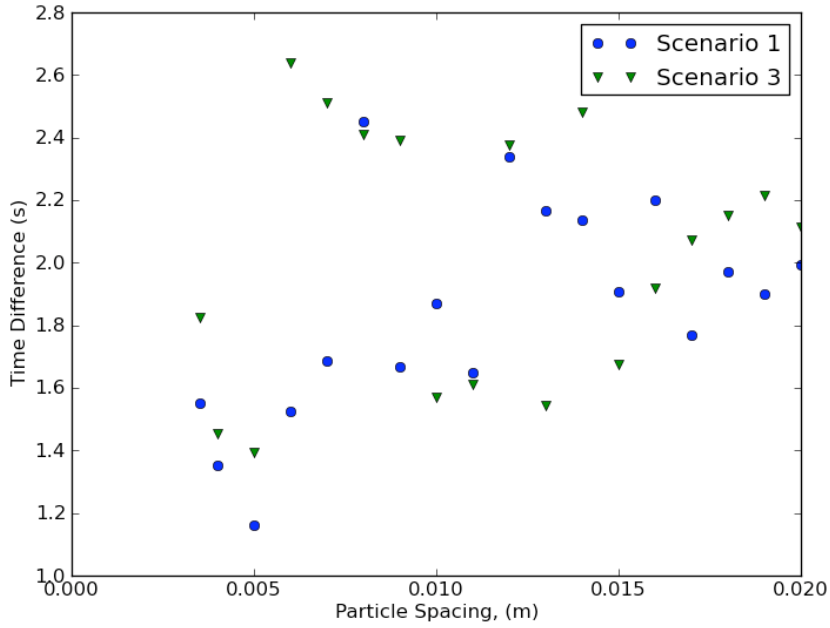

Figure 35. Time difference between maximum forward flow and maximum return flow at location D for Scenarios 1 and 3 using the SPS turbulence term and the quadratic or cubic spline kernels, respectively, versus particle spacing

Figure 35 shows the time difference between maximum forward and return flows versus particle spacing for Scenarios 1 and 3, with the values for Scenario 3 shown in Table 24. As seen in the previous analysis, the Scenario 3 results for the cubic spline kernel tend to be more erratic than the Scenario 1 results for the quadratic kernel. This is particularly true in the drastic difference in time difference between particle spacings 3.5 x 10^{-3}-m to 5 x 10^{-3}-m and 6 x 10^{-3}-m to 9 x 10^{-3}-m. Then the data again drastically changes to a lower time difference for particle spacings 1.0 x 10^{-2}-m and 1.1 x 10^{-2}-m. The results for Scenario 3 are too varying to draw any reasonable conclusions concerning the actual flow conditions from this data. This conclusion is to be expected

based on the erratic behavior of Scenario 3 results previously seen in the analysis compounded by the already erratic nature of these results in Scenario 1.

Table 24. Time between maximum forward and return flows at location D for Scenario 3

Scenario 3 (Cubic Spline Kernel, SPS term)			
Particle Spacing (m)	Time Difference (s)	Particle Spacing (m)	Time Difference (s)
3.5×10^{-3}	1.82	1.2×10^{-2}	2.38
4×10^{-3}	1.45	1.3×10^{-2}	1.54
5×10^{-3}	1.39	1.4×10^{-2}	2.48
6×10^{-3}	2.64	1.5×10^{-2}	1.67
7×10^{-3}	2.51	1.6×10^{-2}	1.92
8×10^{-3}	2.41	1.7×10^{-2}	2.07
9×10^{-3}	2.39	1.8×10^{-2}	2.15
1.0×10^{-2}	1.57	1.9×10^{-2}	2.21
1.1×10^{-2}	1.61	2.0×10^{-2}	2.12

Another measure used to analyze the flow was to view velocity plots of the setup to study the general structure of the flow. Images were compared at three stages in the flow for the 9×10^{-3}-m particle spacing using a plan view pseudo color velocity plot taken at a height of 0.026 m from the bed. Three-dimensional plots were also drawn for these three stages.

Figure 36 shows the plan view velocity plots for Scenarios 1, 2, and 3 at t = 0.77 s. This is the time when the bore has passed the obstruction and is filling the back section of the tank with water. This figure shows that there is no significant difference in the flow structure or magnitude at this time. When comparing Scenarios 1 and 2, the influence of the SPS turbulence term is minimal if existent at all. As evidenced by

earlier comparisons in the velocity and force analyses, there is not much turbulence present in the system yet at this time for most of the flow. Without this turbulence presence, the SPS turbulence term is not needed to calculate any sub-particle scale phenomena. Comparing Scenarios 1 and 3 show that the difference in weighting kernel calculations is not important at this stage in the flow either.

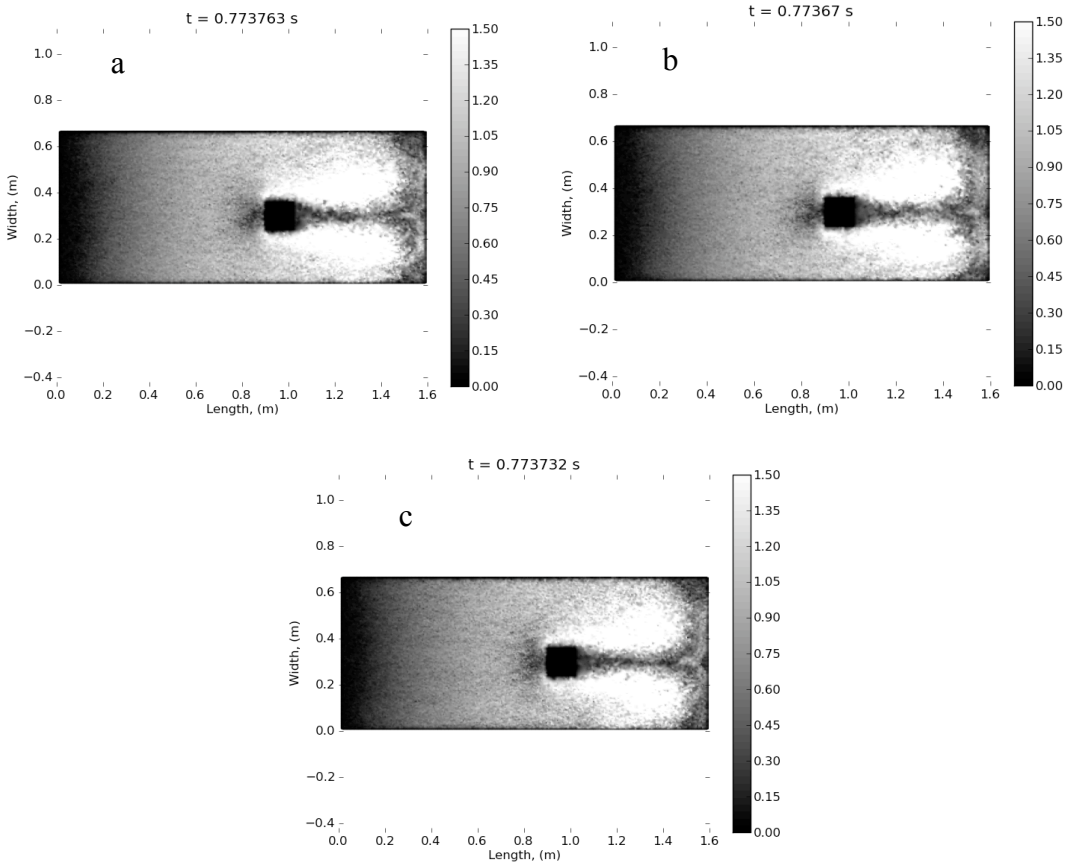

Figure 36. Plan views of velocity at t = 0.77 s for (a) Scenario 1 (quadratic kernel, SPS term), (b) Scenario 2 (quadratic kernel, no SPS turbulence term), and (c) Scenario 3 (cubic spline kernel, SPS turbulence term)

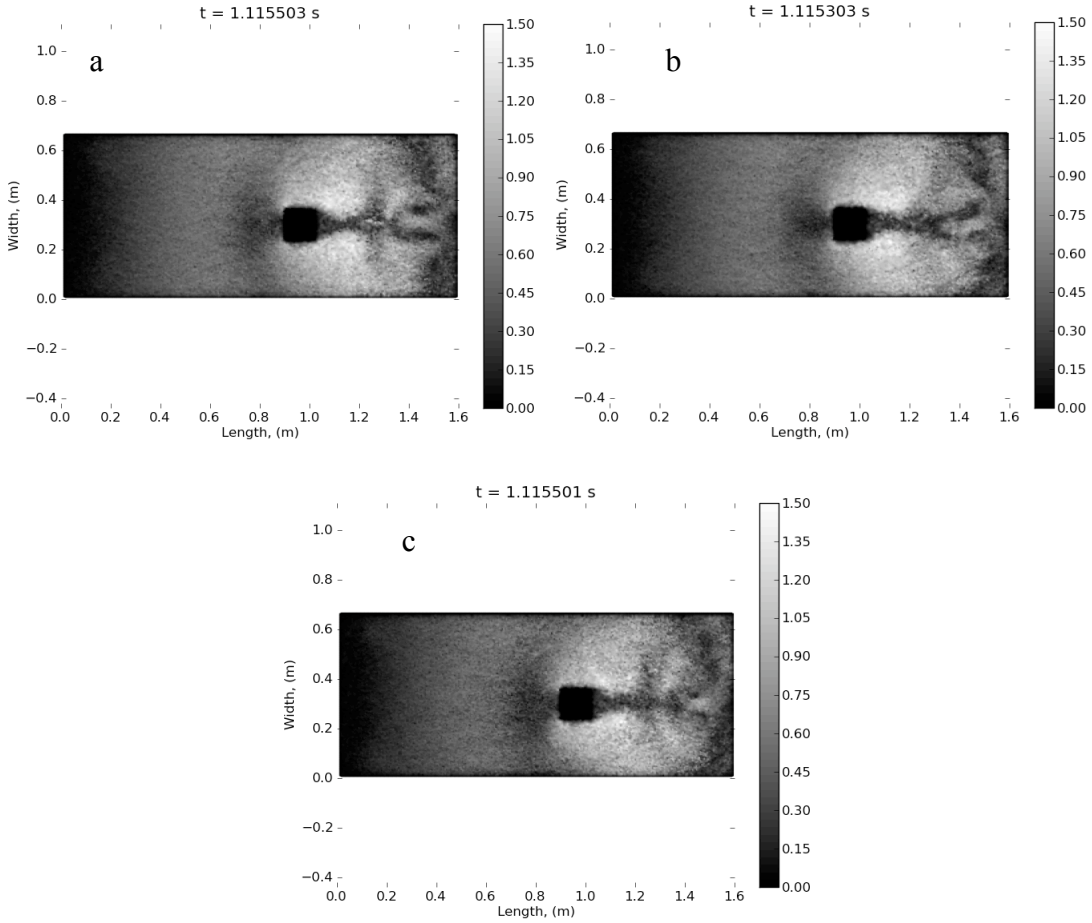

Figure 37. Plan views of velocity at t = 1.1 s for (a) Scenario 1 (quadratic kernel, SPS term), (b) Scenario 2 (quadratic kernel, no SPS turbulence term), and (c) Scenario 3 (cubic spline kernel, SPS turbulence term)

Figure 37 shows the same plots for t = 1.1 s where differences between the scenarios are present. At this time, the initial bore has passed the obstruction, reached the back wall and is beginning the return flow process. In the plan views of Scenarios 1 and 2, a clear difference with the SPS turbulence term is visible behind the obstruction in the range of 1.2 m to 1.6 m lengthwise. Two symmetrical whirlpools are seen forming

in the Scenario 1 case, which includes the SPS turbulence term, that are not as prevalent in the Scenario 2 case, which does not include the SPS turbulence term. These show that that the SPS turbulence term is calculating sub-particle scale turbulence that contributes to these structures. These structures also create a low velocity line across much of the width of the tank at approximately 1.3 m in the lengthwise direction. In the Scenario 2 case, this low velocity line is not as noticeable, showing that in the absence of the eddy structures, the flow is allowed to move faster in the reverse direction of overall flow after reaching the back wall instead of becoming involved with the turbulent structures. This faster return flow is verified in Figure 34 that shows the return time for the Scenario 2 case is less than the return time for the Scenario 1 case at point D for the 9×10^{-3}-m particle spacing case.

To account for these flow structures due to the SPS turbulence term, [*Pope*, 2010] explains the energy cascade concept. The energy cascade for eddy formation states that energy in larger eddies is transferred to the smaller eddies within the larger eddies, which is then transferred to even smaller eddies and so on until the energy dissipates from the system. The lack of flow structures in Scenario 2 of Figure 37 are caused by the inability of the energy of the larger structures to transfer to smaller structures that may be at the sub-particle scale. The whirlpool structures dissipate; transferring this excess energy in to the overall return flow instead of continuing the eddy process at smaller scales.

This whirlpool structure is also different when comparing Scenarios 1 and 3. In Scenario 3, the overall whirlpool structure is present, but the distinction between the

structures and the rest of the flow is less apparent than in the Scenario 1 case. This blending of the velocity values in the flow is probably due to the cubic spline kernel function that places higher weights on values further from the center of the kernel than in the quadratic kernel. With these higher weights further from the center, adjacent velocity values tend to blend, rather than forming the distinct differences as seen in Scenario 1.

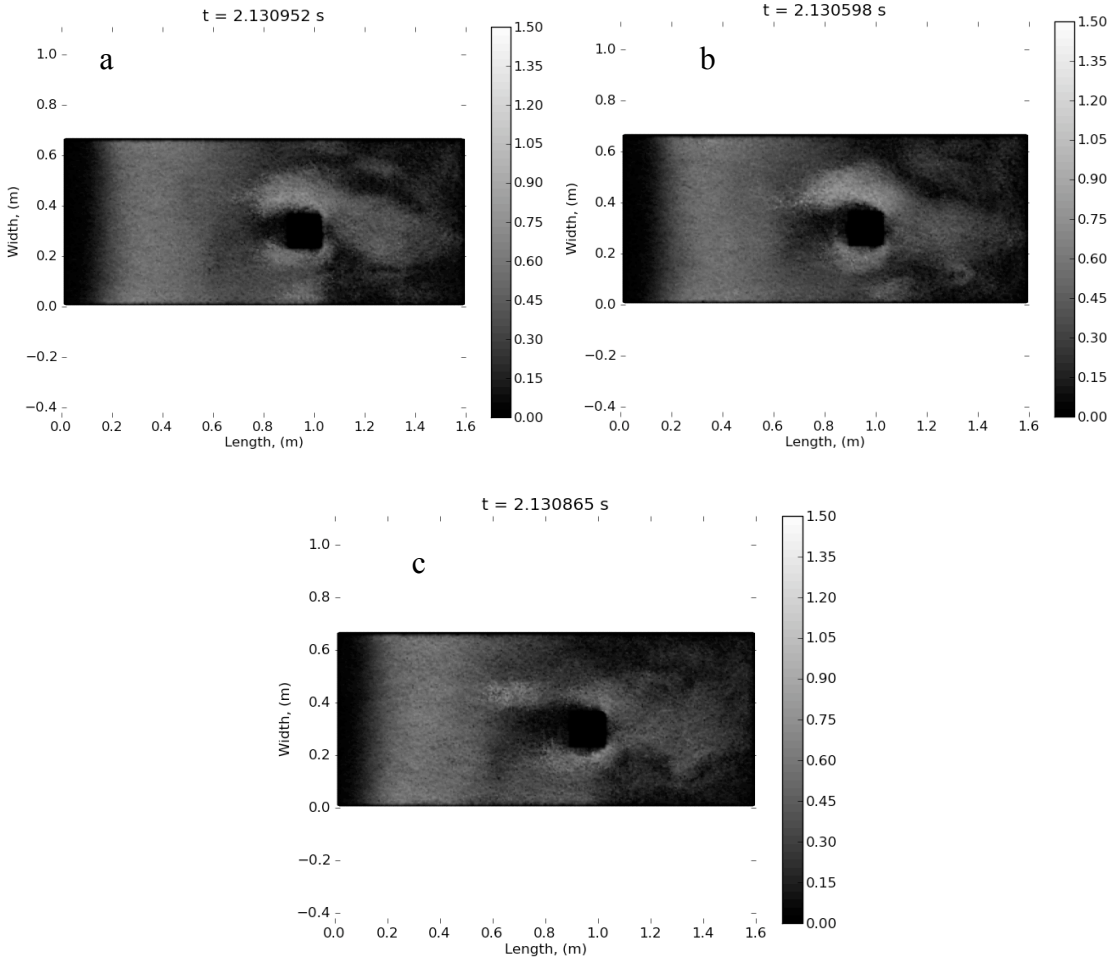

Figure 38. Plan views of velocity at t = 2.1 s for (a) Scenario 1(quadratic kernel, SPS term), (b) Scenario 2 (quadratic kernel, no SPS turbulence term), and (c) Scenario 3 (cubic spline kernel, SPS turbulence term)

Figure 38 shows the plan view and three-dimensional plots at t = 2.1 s when the return flow bore has passed the obstruction and the water is rushing toward the other side. Comparing Scenarios 1 and 2, it can be seen that the flows again have similar characteristics since there are no longer whirlpool structures near the back wall. The main difference between these scenarios is the magnitude of the flow and the distance the flow has travelled. The flow in Scenario 2 has a wider area with high velocity magnitude and has flowed farther in the return direction compared to the flow in Scenario 1. These characteristics can be related back to the turbulent energy dissipation discussed above. The sub-particle scale turbulent structures of the Scenario 1 flow were able to dissipate energy from the flow that was not taken from the Scenario 2 flow, causing faster velocities in Scenario 2.

A comparison of Scenarios 1 and 3 again show the lack of definite features in the Scenario 3 case. While the general flow velocity appears to be of the same order of magnitude, the distinct higher velocity structure seen on the side of the obstruction in Scenario 1 is much less clear in Scenario 3. As explained earlier, this lack of distinction is primarily due to the relatively higher weighting of values away from the center of the cubic spline kernel as compared to the weighting in the quadratic kernel.

4.2.4 Conclusions from DamBreak 1

This study was intended to find the differences and implications of changing the particle spacing, inclusion of the SPS turbulence term, and weighting kernel function. With regards to the particle spacing, the comparisons to the experimental velocity and

force data show that the most accurate particle spacings tend to be in the range of 8 x 10^{-3}-m and 1.1 x 10^{-2}-m. Analysis of the comparison with the experimental velocity data tends toward the lower end of that range, while the force analysis tends toward the higher end of the range and possibly a few larger particle spacings. The most resolute cases tend to have errors due to compiled rounding errors induced by the single precision nature of the machine used to run GPUSPH. The least resolute cases tend to have the most error due to the lack of particles to fill the simulation to accurately capture the flow motion.

The SPS turbulence term was proven to have no significant effect before the flow reached behind the obstruction. Once the flow reached the back wall and began the return flow a significant effect due to the term was visible in the whirlpool structures formed in this area. For the 9 x 10^{-3}-m particle spacing case shown, the sub-particle scale turbulence term in Scenario 1 made the formation of smaller eddies possible, which could absorb turbulent energy from the larger whirlpool structures. The lack of the sub-particle scale turbulence in Scenario 2 caused the excess energy to be transferred back into the system creating a faster return flow.

The cubic spline kernel function tends to blend adjacent values more than the quadratic kernel function due to the different kernel function shapes. The implications of the statement can be seen in the images in Figure 37 and Figure 38, as discussed above. The Scenario 3 images tend to be more blended than the Scenario 1 images for the same flow structures.

4.3 Test Case: DamBreak 2

The second test case was completed on the newer version of GPUSPH to include planes in the code. For this case, planes were used to specify the four sidewalls and boundary particles were used to specify the bottom of the flume. Using the side planes allowed for more fluid particles in the system, providing the ability to test smaller particle spacings than if the sides contained boundary particles.

4.3.1 Results for 0.10-m Initial Free-Surface Elevation Case

The first set of numerical experiments within DamBreak 2 was completed using an initial high water level of 0.10-m and a low water level of 0.02-m. Details about the setup of this case were discussed in Section 3. Figure 39 shows the velocity time series collected for these runs for various particle spacings. Qualitatively, the graph indicates that there is a significant impact of particle spacing on the numerical results. These impacts will be quantified and analyzed based on velocity values.

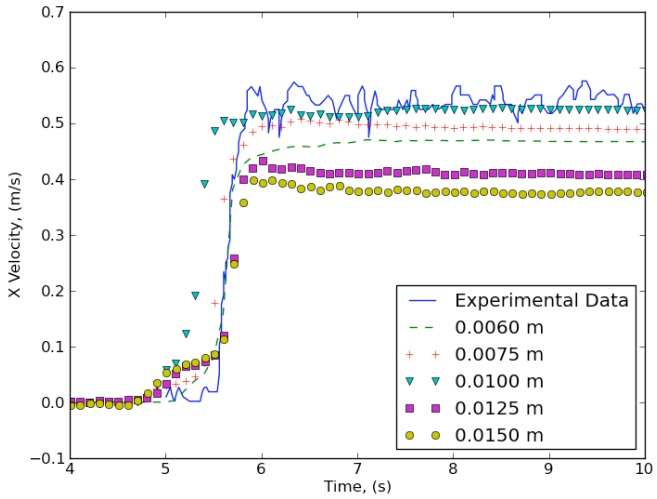

Figure 39. Velocity time series of Scenario 1 (quadratic kernel, SPS term) 0.10-m initial free-surface elevation tests for various particle spacings

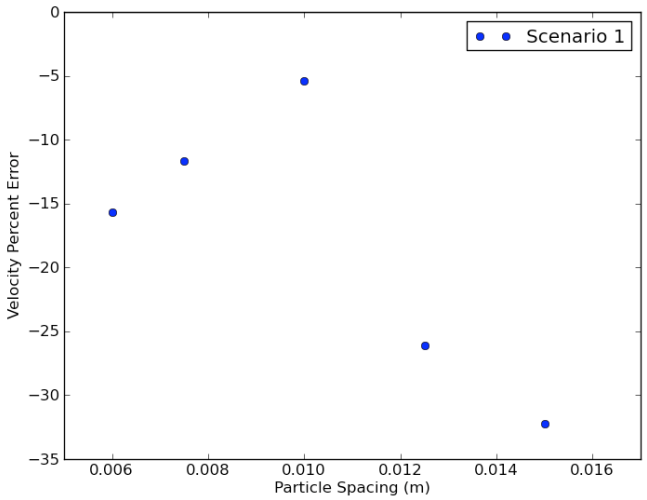

Figure 40. Velocity percent error versus particle spacing for Scenario 1 (quadratic kernel, SPS term)

Table 25. Velocity percent error for Scenario 1

Scenario 1 (Quadratic Kernel, SPS term)		
Particle Spacing (m)	Velocity Value (m/s)	Percent Error
6.0×10^{-3}	0.47	-15.69
7.5×10^{-3}	0.49	-11.67
1.00×10^{-2}	0.52	-5.43
1.25×10^{-2}	0.41	-26.11
1.50×10^{-2}	0.38	-32.22

A way to determine the accuracy of the numerical data with respect to the experimental data is to compute the percent error of the mean velocity in the timeframe that it plateaus after 7.0 s. Figure 40 and Table 25 shows the results of this calculation for Scenario 1 with particle spacing on the abscissa and velocity percent error on the ordinate. The figure shows that the 1.00×10^{-2}-m particle spacing is the most accurate of these cases with decreasing accuracy as the particle spacing diverges from this case.

Another distinguishing aspect of Figure 40 is that the smallest three particle spacings and the largest two particle spacings form two distinct linear trends in terms of percent error. The smallest particle spacings have errors of 5.4%, 11.7%, and 15.7% and the larger particle spacings have errors of 26.1% and 32.2%. This distinct difference can be due to the many reasons discussed in DamBreak 1, including numerical precision. Another possible reason for this error is the initial placement of particles in the system.

Figure 41 shows a side view of the particle positions for the five particle spacing cases at 0.1 s, the first output time. While these points are identified as the "particle" positions, it is important to remember that these points are actually moving grid points in

the domain. Because of the nature of the particle spacings, there can only be a discrete number of particle layers in the initial setup. This discrete number means that the top particles may be below or above the actual value designated as the free-surface elevation, depending on the particle spacing size.

Figure 41 shows that while the free-surface elevation behind the dam hovers around 0.10-m as expected, it is difficult to accurately capture the lower free-surface elevation in front of the dam. This was not a problem in DamBreak 1, since the water in front of the dam was only residual water and could be modeled with one layer of particles for most particle spacings or two layers for the smallest particle spacings. For DamBreak 2, the modeling of the lower free-surface elevation is especially problematic for the two largest particle spacings, creating high grid points when compared to the modeled free-surface elevation. This inconsistency could produce an artificially higher numerical free-surface elevation in these cases, which would slow the overall flow as indicated in the velocity percent error analysis.

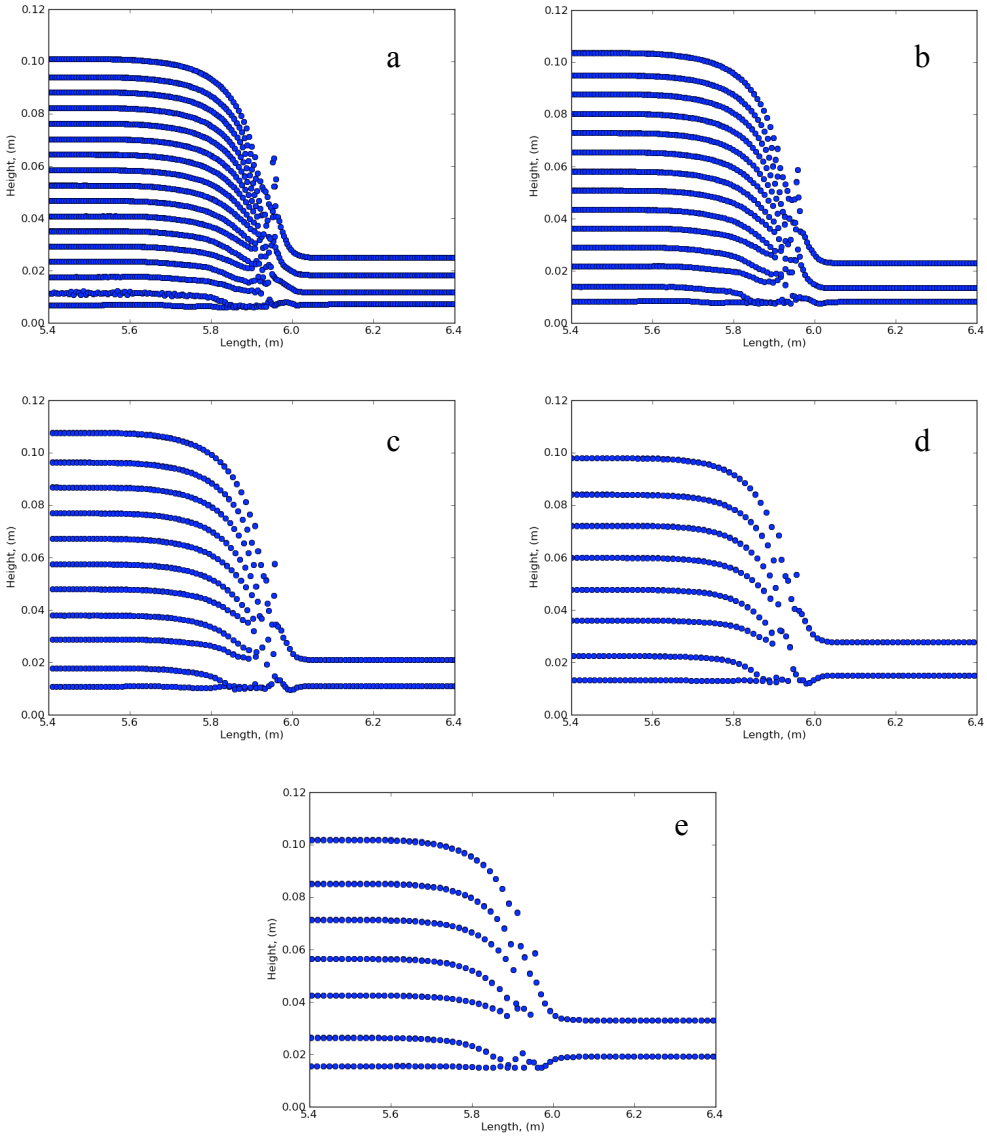

Figure 41. Side views of particle positions 0.1 s after problem initiation with particle spacings of (a) 6.0 x 10^{-3}-m, (b) 7.5 x 10^{-3}-m, (c) 1.00 x 10^{-2}-m, (d) 1.25 x 10^{-2}-m, and (e) 1.50 x 10^{-2} m, vertical axis distorted

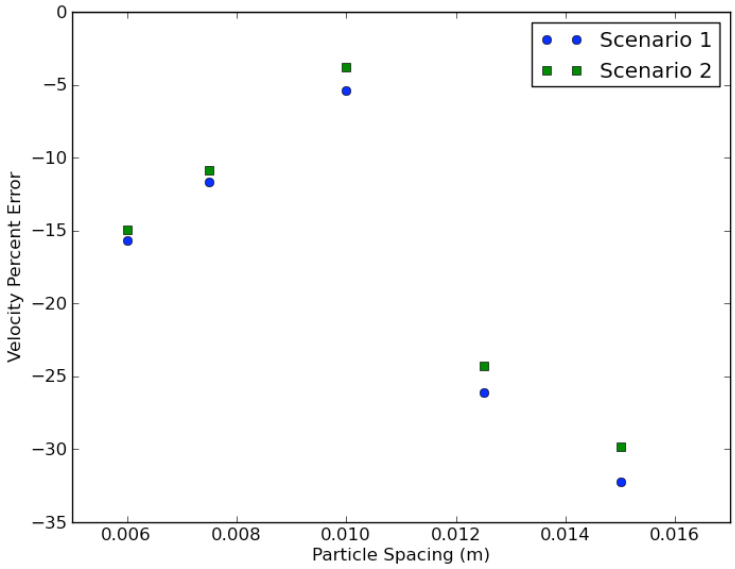

Figure 42. Velocity percent error versus particle spacing for Scenarios 1 and 2 using quadratic kernel and including or excluding the SPS turbulence term, respectively

Table 26. Velocity percent error for Scenario 2

Scenario 2 (Quadratic Kernel, No SPS term)		
Particle Spacing (m)	Velocity Value (m/s)	Percent Error
6.0×10^{-3}	0.47	-14.96
7.5×10^{-3}	0.49	-10.90
1.00×10^{-2}	0.53	-3.81
1.25×10^{-2}	0.42	-24.25
1.50×10^{-2}	0.39	-29.85

Figure 42 shows the velocity percent error results for Scenarios 1 and 2, which compares the inclusion or exclusion of the SPS turbulence term. Table 26 shows the velocity percent error values for Scenario 2. For each of the particle spacings, Scenario 2, the case without the SPS turbulence term, produces better results than Scenario 1. The two scenarios have less of a difference as the particle spacings decrease, with a

difference of 0.7% for the 6.0 x 10^{-3}-m particle spacing and a difference of 2.4% for the 1.50 x 10^{-2}-m particle spacing. These findings show that the SPS turbulence term has a greater influence when the sub-particle scale is larger, as expected. What is not expected is that the SPS turbulence term seems to produce results that are less accurate than the results without the term. While the differences in percent error of these data sets are small, these results may be an indication that the SPS turbulence term is creating artificial turbulence in the bore. As noted in the discussion of DamBreak 1, this artificial turbulence would consist of smaller sub-particle scale eddies that could absorb energy from the system due to the energy cascade effect, which would slow the overall bore velocity as indicated in this figure.

In the analysis for DamBreak 1, it was concluded that the SPS turbulence term did not have an effect on the flow before the flow reached the obstruction. There is no obstruction in DamBreak 2, leading us to believe that the SPS turbulence term should have a similar small impact. The main difference between DamBreak 1 and DamBreak 2 is that DamBreak 2 is conducted in a much longer flume, giving the flow more time and space to create turbulent structures within the velocity bore that the SPS turbulence term would resolve. While the differences between the results of Scenario 1 and the results of Scenario 2 are small, these additionally turbulent structures may explain this trend.

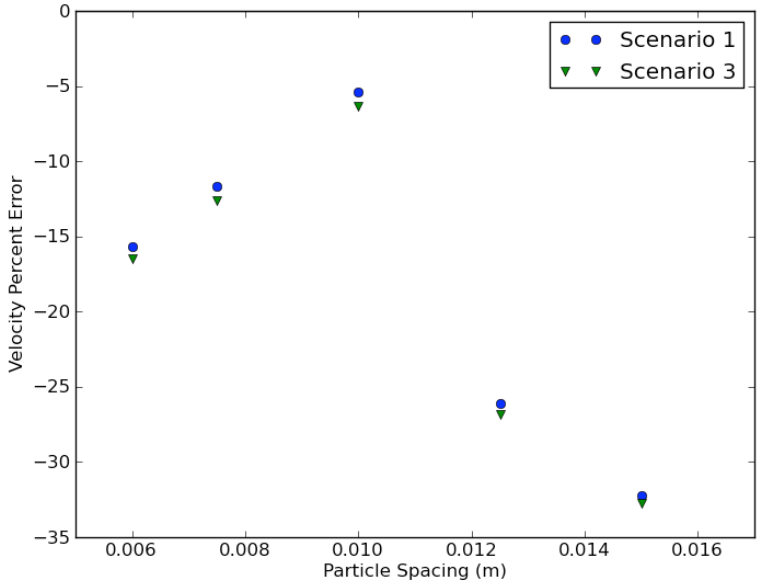

Figure 43. Velocity percent error versus particle spacing for Scenarios 1 and 3 using the SPS turbulence term and the quadratic or cubic spline kernels, respectively

Table 27. Velocity percent error for Scenario 3

Scenario 3 (Cubic Spline Kernel, SPS term)		
Particle Spacing (m)	Velocity Value (m/s)	Percent Error
6.0×10^{-3}	0.46	-16.51
7.5×10^{-3}	0.48	-12.60
1.00×10^{-2}	0.52	-6.36
1.25×10^{-2}	0.40	-26.85
1.50×10^{-2}	0.37	-32.73

Figure 43 shows the same plot of velocity percent error for Scenarios 1 and 3, with the values for Scenario 3 shown in Table 27. The Scenario 1 results are more accurate than the Scenario 3 results for all particle spacings, but the differences in percent error are not large. For these cases, the largest differences in percent error are in

the smaller particle spacing cases and decrease in the larger particle spacing cases, with a 0.8% difference at 6.0 x 10^{-3}-m particle spacing and 0.5% difference at 1.50 x 10^{-2}-m particle spacing. These differences are too small to draw any major conclusions to compare the effects of the quadratic kernel and the cubic spline kernel. This lack of difference is most likely due to the fact that there is no great variation in the flow velocity, like what was seen in DamBreak 1. Once the velocity bore in DamBreak 2 reaches the measurement point, the velocity tends to stay about the same as opposed to the instantaneous deceleration seen in the DamBreak 1 time series. If the velocity is relatively constant throughout, then the kernel function should not have much influence since all the values tend to be about the same.

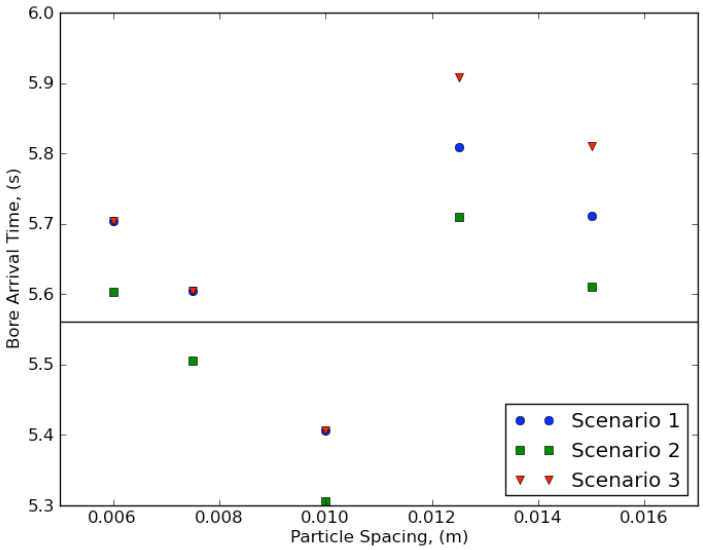

Figure 44. Bore arrival time for Scenarios 1, 2, and 3 for 0.10-m initial higher free-surface elevation

Table 28. Bore arrival time for Scenarios 1, 2, and 3 for 0.10-m initial higher free-surface elevation

Scenario 1 (Quadratic Kernel, SPS term)		Scenario 2 (Quadratic Kernel, No SPS term)		Scenario 3 (Cubic Spline Kernel, SPS term)	
Particle Spacing (m)	Bore Arrival Time (s)	Particle Spacing (m)	Bore Arrival Time (s)	Particle Spacing (m)	Bore Arrival Time (s)
6.0×10^{-3}	5.7	6.0×10^{-3}	5.6	6.0×10^{-3}	5.7
7.5×10^{-3}	5.6	7.5×10^{-3}	5.5	7.5×10^{-3}	5.6
1.00×10^{-2}	5.4	1.00×10^{-2}	5.3	1.00×10^{-2}	5.4
1.25×10^{-2}	5.8	1.25×10^{-2}	5.7	1.25×10^{-2}	5.9
1.50×10^{-2}	5.7	1.50×10^{-2}	5.6	1.50×10^{-2}	5.8

Figure 44 and Table 28 show the bore arrival time, plotted on the ordinate, for each of the scenarios and the arrival time of the experimental bore (solid line). There is no significant difference in arrival times of the experimental and numerical bores and no accurate way to compare these times. Despite this issue, the numerical bore arrival times can be loosely compared relative to each other. These arrival times were determined by recording the time at which there was greatest instantaneous acceleration for each case. It is important to realize that because this data was output at 10 Hz, the arrival times will be accurate only to 0.1 s, which is a low resolution relative to the differences in arrival time. While the bore arrival times for all the cases are within 0.5 s of the experimental bore arrival time and can be considered accurate, the relative timing of the bores are good indicators of how the SPS turbulence term and weighting function affect the flow. The results show that for each particle spacing, the bore in the Scenario 2 case arrived first. For the smallest three particle spacings, the bores for Scenarios 1

and 3 arrived at the same time, while for the largest two particle spacings, the bore for Scenario 1 arrived earlier than the bore for Scenario 3. This trend indicates that the added sub-particle scale turbulence in Scenarios 1 and 3 slows the flow by dissipating energy at the sub-particle scale of this turbulence, which is in agreement of the results discussed in the analysis of DamBreak 1. The weighting kernel type seems to not have an effect for the smaller particle spacings, but the cubic spline kernel found in Scenario 3 tends to dampen the bore velocity. Since this trend is not the same for all the particle spacings, there can be no significant conclusion based on this data.

The 0.10-m initial free-surface elevation case for the DamBreak 2 results show that the 1.00×10^{-2}-m particle spacing results are the most accurate when comparing the numerical velocity with the experimental results. This conclusion is most likely due to the difficulties in modeling the lower free-surface elevation for the 1.25×10^{-2}-m and 1.50×10^{-2}-m particle spacing cases as shown in Figure 41. These inaccurate numerical lower free-surface elevations cannot be resolved at these larger particle spacings, making the overall flow characteristics also inaccurate. The 6.0×10^{-3}-m and 7.5×10^{-3}-m particle spacing cases are most likely influenced by the same single precision errors that affected the most resolute cases in DamBreak 1. These errors occur in the calculations for the millions of particles in the system and are amplified as these particles interact.

The SPS turbulence term was found to have no impact on the higher resolution 0.10-m initial height cases and little impact on the lower resolution cases. As discussed earlier, this is likely due to the longer flume when compared to DamBreak 1 that allows for more time to form sub-particle scale turbulence in the bore. This additional

turbulence dissipates energy from the system causing the Scenario 1 cases to be slightly slower than the Scenario 2 cases. The weighting kernel function was found to have no significant influence on the numerical results for the 0.10-m initial free-surface elevation case. This is due to the absence of significantly varying velocities in the flume, causing both kernel functions to produce the same relative results.

4.3.2 Results for 0.15-m Initial Free-Surface Elevation Case

Now that conclusions have been found regarding the 0.10-m initial free-surface elevation case, a comparison of the 0.15-m initial free-surface elevation case for DamBreak 2 will be completed. For this case we will again compare the particle spacings, inclusion of the SPS turbulence term, and the weighting function.

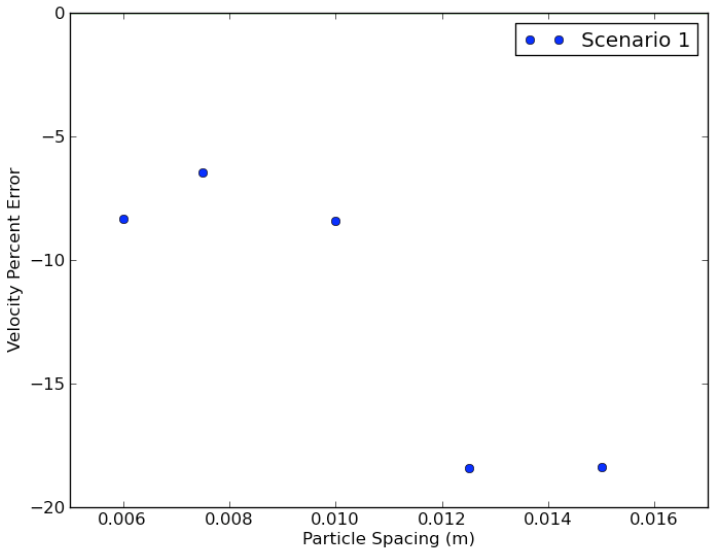

Figure 45. Velocity percent error versus particle spacing for Scenario 1 (quadratic kernel, SPS term)

Table 29. Velocity percent error values for 0.15-m initial free-surface elevation case for Scenario 1

Scenario 1 (Quadratic Kernel, SPS term)		
Particle Spacing (m)	Velocity Value (m/s)	Percent Error
6.0×10^{-3}	0.71	-8.34
7.5×10^{-3}	0.72	-6.45
1.00×10^{-2}	0.71	-8.40
1.25×10^{-2}	0.63	-18.42
1.50×10^{-2}	0.63	-18.38

Figure 45 and Table 29 shows the velocity percent error of with respect to particle spacing for Scenario 1 when compared with the experimental results. Particle spacing is plotted on the abscissa and velocity percent error is indicated on the ordinate. For the 0.15-m initial higher free-surface elevation case, the most accurate velocity occurs when the particle spacing is 7.5×10^{-3}-m. Again, there are two distinct groups of data with the three smaller particle spacings having errors of 8.3%, 6.4%, and 8.4% while the two larger particle spacings both have errors of 18.4%. As shown in Figure 46 that shows the side view of the particle placement after one recording period, the same problem as experienced in the 0.10-m initial free-surface elevation case exists of having particle spacings too large to accurately replicate the lower free-surface elevation in the numerical model. This artificially high numerical lower free-surface elevation could slow the overall flow velocity, creating the percent error results shown.

As shown in all the other velocity percent error analyses in this thesis, there is a hook feature in the curve with respect to particle spacing for the most resolute cases. This interesting aspect about this curve is that it appears to show that the 7.5×10^{-3}-m

particle spacing is the most accurate case as opposed to the 1.00 x 10^{-2}-m particle spacing case in the 0.10-m initial free-surface elevation simulations. When discussing the error of the higher resolution cases, the rounding errors due the single precision of the GPU used is normally considered the source of the error, but this conclusion goes against what is seen in this case. The 0.15-m initial free-surface elevation case should have more particles than the 0.10-m initial free-surface elevation case and thus more error at more resolute cases. Instead, these cases show that the most accurate case for the higher initial free-surface elevation is at a more resolute setting than the case for the lower initial free-surface elevation.

This counterintuitive conclusion may come from the initial setup of the numerical cases. Similar to the issues accurately capturing the lower free-surface elevation, there seems to be a difference in where the top layer of particles fall based on particle spacing. As seen in Figure 46, the setups of particle spacings 1.00 x 10^{-2}-m and 1.25 x 10^{-2}-m may artificially underestimate the initial higher free-surface elevation. This could lead to a slower velocity and less accurate results for the 1.00 x 10^{-2}-m particle spacing.

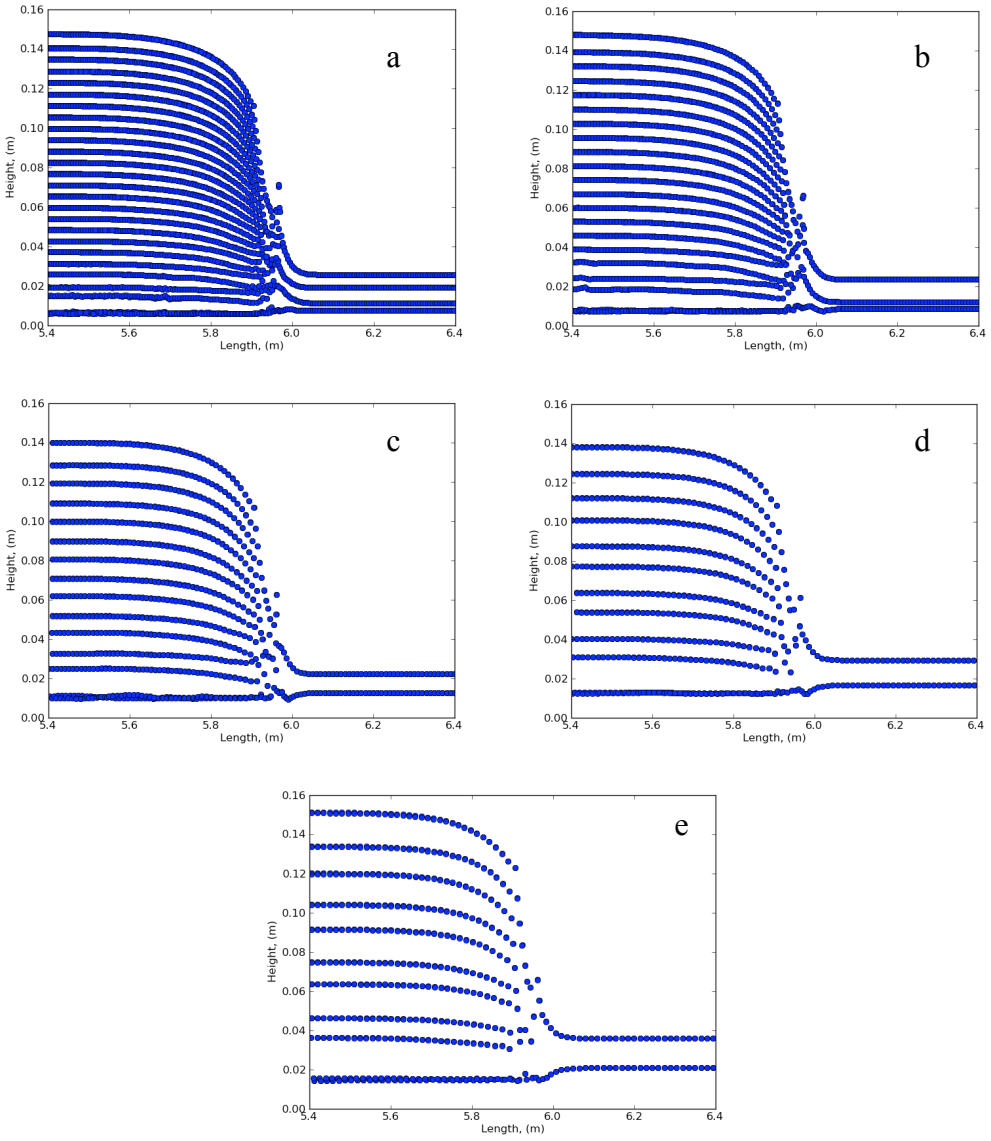

Figure 46. Side views of particle positions 0.1 s after problem initiation with particle spacings of (a) 6.0 x 10^{-3}-m, (b) 7.5 x 10^{-3}-m, (c) 1.00 x 10^{-2}-m, (d) 1.25 x 10^{-2}-m, and (e) 1.50 x 10^{-2} m, vertical axis distorted

Figure 47 compares the velocity percent error for Scenarios 1 and 2, with the values for Scenario 2 shown in Table 30. As in the 0.10-m initial height case, the

Scenario 2 cases are more accurate than the Scenario 1 cases, with the larger differences in the larger particle spacings. The percent error difference is 0.8% for the 6.0 x 10^{-3}-m particle spacing and increases with each spacing to a 2.2% difference in the 1.50 x 10^{-2}-m particle spacing results. These results further confirm that the SPS turbulence term has a greater influence when the particle spacing is larger, creating a larger sub-particle scale to resolve. The figure also shows that these SPS turbulence effects may be artificial as they decrease the accuracy of the velocity results.

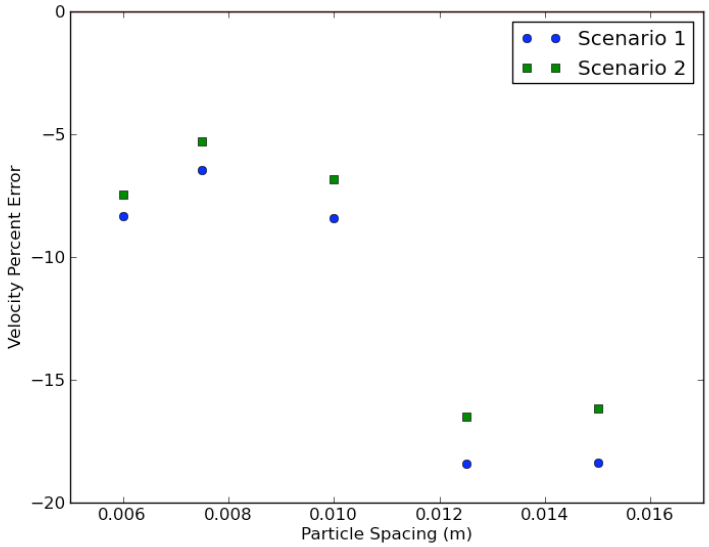

Figure 47. Velocity percent error versus particle spacing for Scenarios 1 and 2 using quadratic kernel and including or excluding the SPS turbulence term, respectively

Table 30. Velocity percent error values for the 0.15-m initial free-surface elevation case for Scenario 2

Scenario 2 (Quadratic Kernel, No SPS term)		
Particle Spacing (m)	Velocity Value (m/s)	Percent Error
6.0×10^{-3}	0.71	-7.48
7.5×10^{-3}	0.73	-5.27
1.00×10^{-2}	0.72	-6.84
1.25×10^{-2}	0.64	-16.51
1.50×10^{-2}	0.65	-16.18

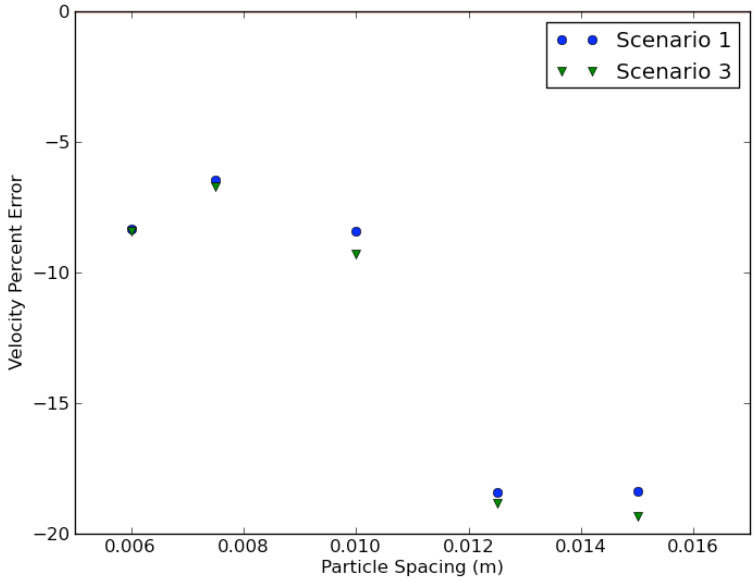

Figure 48. Velocity percent error versus particle spacing for Scenarios 1 and 3 using the SPS turbulence term and the quadratic or cubic spline kernels, respectively

Table 31. Velocity percent error value for 0.15-m initial free-surface elevation case for Scenario 3

Scenario 3 (Cubic Spline Kernel, SPS term)		
Particle Spacing (m)	Velocity Value (m/s)	Percent Error
6.0×10^{-3}	0.71	-8.43
7.5×10^{-3}	0.72	-6.73
1.00×10^{-2}	0.70	-9.31
1.25×10^{-2}	0.62	-18.85
1.50×10^{-2}	0.62	-19.34

Figure 48 and Table 31 compares the velocity percent errors for Scenarios 1 and 3, which shows that all the percent differences are within 1% of each other for each particle spacing. Despite the similarity of the velocity for each of these particle spacings, the figure shows that in each case, the Scenario 1 result is slightly more accurate than the Scenario 3 result. This shows that the quadratic weighting kernel function is slightly more accurate in computing the velocity than the cubic spline weighting kernel function, but the difference is not significant.

Figure 49 and Table 32 show the bore arrival times on the ordinate for the various scenarios and particle spacings and the experimental data (black line), calculated in the same manner as the bore arrival times for an initial free-surface elevation of 0.10-m. This plot shows that all of the cases have a bore arrival time within 0.4 s of the experimental bore arrival time, which is within acceptable limits. All of the particle spacing cases except the 1.25×10^{-2}-m particle spacing case, converges to the 4.4 s and 4.5 s arrival times. All three scenarios for the 1.25×10^{-2}-m particle spacing have a small delayed arrival relative to the other cases. This observation is not a significant

difference, but could be due to the influence of the initial particle grid point placement discussed earlier. For particle spacing 1.25 x 10^{-2}-m, the grid points for the higher water level tend to the low side of the 0.15-m free-surface elevation and tend to the high side for the lower water level of 0.02-m. The combination of these two factors could slow the flow slightly to produce the effect shown here.

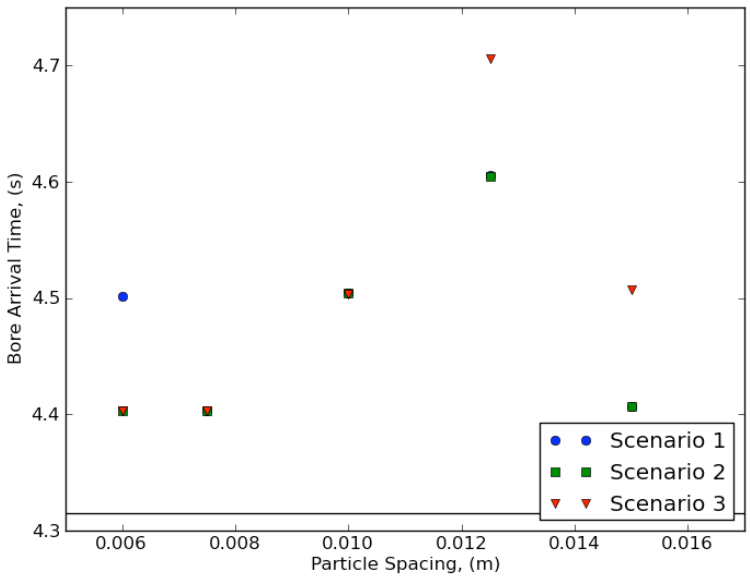

Figure 49. Bore arrival time for Scenarios 1, 2, and 3 for 0.15-m initial higher free-surface elevation

Table 32. Bore arrival time for Scenarios 1, 2, and 3 for 0.15-m initial higher free-surface elevation

Scenario 1 (Quadratic Kernel, SPS term)		Scenario 2 (Quadratic Kernel, No SPS term)		Scenario 3 (Cubic Spline Kernel, SPS term)	
Particle Spacing (m)	Bore Arrival Time (s)	Particle Spacing (m)	Bore Arrival Time (s)	Particle Spacing (m)	Bore Arrival Time (s)
6.0×10^{-3}	4.5	6.0×10^{-3}	4.4	6.0×10^{-3}	4.4
7.5×10^{-3}	4.4	7.5×10^{-3}	4.4	7.5×10^{-3}	4.4
1.00×10^{-2}	4.5	1.00×10^{-2}	4.5	1.00×10^{-2}	4.5
1.25×10^{-2}	4.6	1.25×10^{-2}	4.6	1.25×10^{-2}	4.7
1.50×10^{-2}	4.4	1.50×10^{-2}	4.4	1.50×10^{-2}	4.5

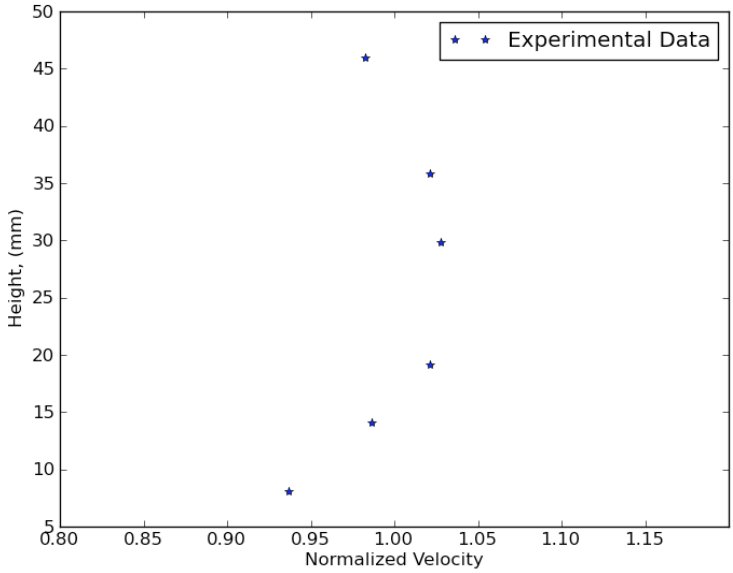

Figure 50. Boundary layer velocities normalized with respect to overall velocity from experimental data

Table 33. Experimental normalized boundary layer velocity values

Experimental Values	
Height (mm)	Normalized Velocity
8.08	0.94
14.14	0.99
19.19	1.02
29.80	1.03
35.86	1.02
45.96	0.98

In addition to the depth averaged velocity at a point, the boundary layer velocity profile is available for the 0.15-m initial height case. Figure 50 and Table 33 show the normalized velocity profile points from the experimental data. The normalized velocity values on the abscissa are plotted against the height above the bottom of the tank on the ordinate. Velocities were calculated from the numerical results using the kernel functions utilized in the simulation. Because various particle spacings and scenarios produced different overall velocities, the velocities at these boundary layer points were normalized with respect to the overall velocities to better compare between the cases by:

$$V_n = \frac{v_b}{v_f} \tag{4.2}$$

where:

V_n is the normalized velocity value

v_b is the boundary layer velocity value

v_f is the overall flow velocity

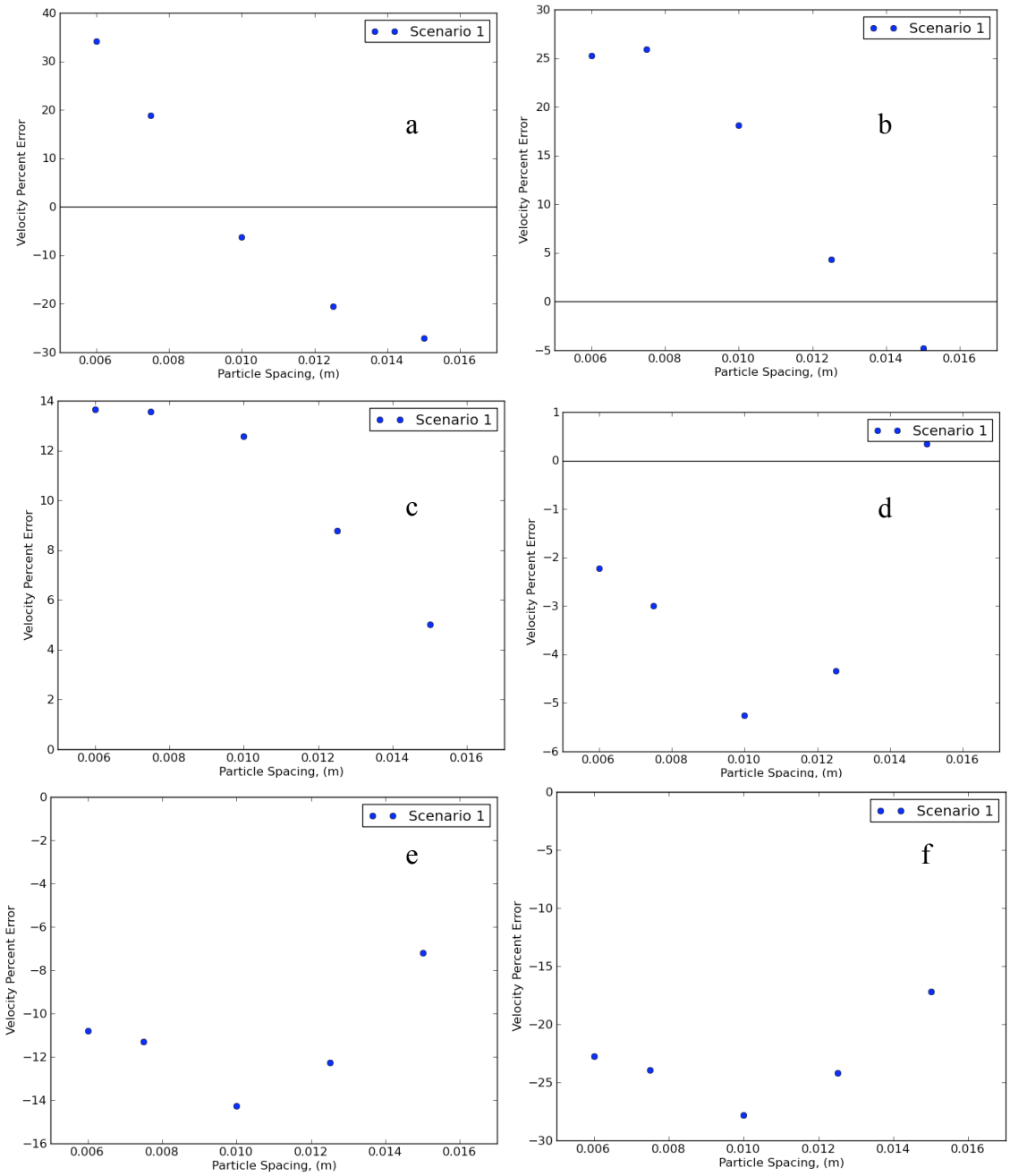

Figure 51. Percent error of boundary layer velocity normalized with respect to overall velocity from profile points at heights of (a) 8.08 mm, (b) 14.14 mm, (c) 19.19 mm, (d) 29.80 mm, (e) 35.86 mm, and (f) 45.96 mm from the bottom for Scenario 1 (quadratic kernel, SPS term)

A percent error analysis was completed on each boundary layer point for each case, as shown in Figure 51 and Table 34 for Scenario 1. While the 7.5 x 10^{-3}-m particle spacing case was the most accurate for the overall flow velocity, this is not necessarily true when comparing the normalized velocities at each point in the boundary layer.

Table 34. Normalized velocity values and percent errors from profile points for Scenario 1

Scenario 1 (Quadratic Kernel, SPS term)					
Point A: 8.08 mm height			Point B: 14.14 mm height		
Particle Spacing (m)	Normalized Velocity	Percent Error	Particle Spacing (m)	Normalized Velocity	Percent Error
6.0 x 10^{-3}	1.26	34.13	6.0 x 10^{-3}	1.24	25.27
7.5 x 10^{-3}	1.11	18.80	7.5 x 10^{-3}	1.24	25.92
1.00 x 10^{-2}	0.88	-6.25	1.00 x 10^{-2}	1.17	18.15
1.25 x 10^{-2}	0.74	-20.53	1.25 x 10^{-2}	1.03	4.33
1.50 x 10^{-2}	0.68	-27.14	1.50 x 10^{-2}	0.94	-4.80
Point C: 19.19 mm height			Point D: 29.80 mm height		
Particle Spacing (m)	Normalized Velocity	Percent Error	Particle Spacing (m)	Normalized Velocity	Percent Error
6.0 x 10^{-3}	1.16	13.64	6.0 x 10^{-3}	1.00	-2.23
7.5 x 10^{-3}	1.16	13.56	7.5 x 10^{-3}	1.00	-2.99
1.00 x 10^{-2}	1.15	12.58	1.00 x 10^{-2}	0.97	-5.25
1.25 x 10^{-2}	1.11	8.77	1.25 x 10^{-2}	0.98	-4.34
1.50 x 10^{-2}	1.07	5.01	1.50 x 10^{-2}	1.03	0.34
Point E: 35.86 mm height			Point F: 45.96 mm height		
Particle Spacing (m)	Normalized Velocity	Percent Error	Particle Spacing (m)	Normalized Velocity	Percent Error
6.0 x 10^{-3}	0.91	-10.81	6.0 x 10^{-3}	0.76	-22.78
7.5 x 10^{-3}	0.91	-11.29	7.5 x 10^{-3}	0.75	-23.95
1.00 x 10^{-2}	0.88	-14.28	1.00 x 10^{-2}	0.71	-27.82
1.25 x 10^{-2}	0.90	-12.28	1.25 x 10^{-2}	0.74	-24.21
1.50 x 10^{-2}	0.95	-7.21	1.50 x 10^{-2}	0.81	-17.19

For the purpose of discussion, the boundary layer points will be referred to as points A through F to correspond to heights from the bottom of the tank of 8.08 mm, 14.14 mm, 19.19 mm, 29.80 mm, 35.86 mm, and 45.96 mm, respectively. For boundary point A, the most accurate result occurs at the 1.00×10^{-2}-m particle spacing with a -6.2% error, meaning that the experimental result is larger than the numerical result. The 7.5×10^{-3}-m and 1.25×10^{-2}-m particle spacings are the next most accurate with errors of 18.8% and -20.5%, respectively. The values in this plot seem to form a curve decreasing with increasing particle spacing absent of the hook like structure found in the other five plots in this figure. This is probably due to the proximity of the measurement location to the bottom of the flume. While boundary layer point A is approximately 8.1×10^{-3} m from the bottom of the flume, the three larger particle spacings of 1.00×10^{-2}-m, 1.25×10^{-2}-m, and 1.50×10^{-2}-m already exceed this value. This means that larger particle spacings will have larger kernel radii that will extend outside the bottom of the flume, producing smaller velocity results. This trend is demonstrated by the continual downward slope in Figure 51 (a).

As the boundary layer points move further away from the bottom of the flume, the hook like shape begins to reappear in the results. Unlike the overall velocity percent error analysis, these hook shapes indicate an optimal particle spacing with the most inaccurate data. The largest particle spacings tend to produce the most accurate results for each of the five remaining boundary layer points. Point B shows that particle spacings of 1.25×10^{-2}-m and 1.50×10^{-2}-m produce errors of 4.3% and -4.8%, respectively. The errors may be low for the larger particle spacings for boundary layer

point B due to the proximity to the bottom of the flume, but at this height, the majority of heavier weighted sections of the kernel is within the flume and should provide a decent result. The smaller particle spacings produce the least accurate results with errors ranging from 18.1% to 25.9%. These errors tend to be excessive in predicting an accurate velocity at this depth.

The plot for boundary layer point C shows that all of the particle spacing cases overestimate the velocity at this point, but the errors range from 5.0% to 13.6%. This error range is not ideal, but it is within acceptable limits. Again, the most accurate result occurs at a particle spacing of 1.50×10^{-2}-m and the least accurate result occurs at particle spacings of 6.0×10^{-3}-m and 7.5×10^{-3}-m. Boundary layer point D has the most accurate numerical results with errors ranging from -5.3% to 0.3%. While the most accurate results occur at a particle spacing of 1.50×10^{-2}-m for this case, the next most accurate results occur at the smallest particle spacings with -2.2% error at 6.0×10^{-3}-m particle spacing and -3.0% error at 7.5×10^{-3}-m particle spacing. This is a change from the results at boundary layer point C where the 7.5×10^{-3}-m particle spacing had the least accurate results. Boundary layer point D also brings a change where most of the results underestimate the experimental result, as opposed to the primarily overestimated results at boundary layer points B and C.

Boundary layer points E and F show a similar trend of relative percent error as boundary layer point D, with the most accurate results occurring at a particle spacing of 1.50×10^{-2}-m and the next most accurate results occurring at particle spacings 6.0×10^{-3}-m and 7.5×10^{-3}-m. For boundary layer point E, the errors for these three particle

spacings are -7.2%, -10.8% and -11.3%, respectively. Similarly, for boundary layer point F, the errors for these particle spacings are -17.2%, -22.8%, and -23.9%.

The overall trends in the velocity percent error of the boundary layer points shows that if the point closest to the bottom is excluded, the largest particle spacing produces the most accurate result and the 1.00×10^{-2}-m particle spacing produces the least accurate results. This is an interesting finding, considering the exact opposite trend occurred when analyzing the overall flow velocity. Another observation from the overall flow velocity trend is that, when excluding point A, the numerical models tend to overestimate the experimental values closest to the bottom of the flume, and then underestimate experimental values further away from the bottom of the flume. These results indicate that there is a fast flow layer near the surface, particularly for the smaller particle spacings. This may be due to the effect of the boundary particle forces lifting the fluid particles away from the boundary, condensing more particles within the kernel range of the boundary layer points B and C. If more particles flowing in the same direction are condensed into the kernel, there are more contributions to the velocity of these particles in the direction of flow, creating a larger velocity value.

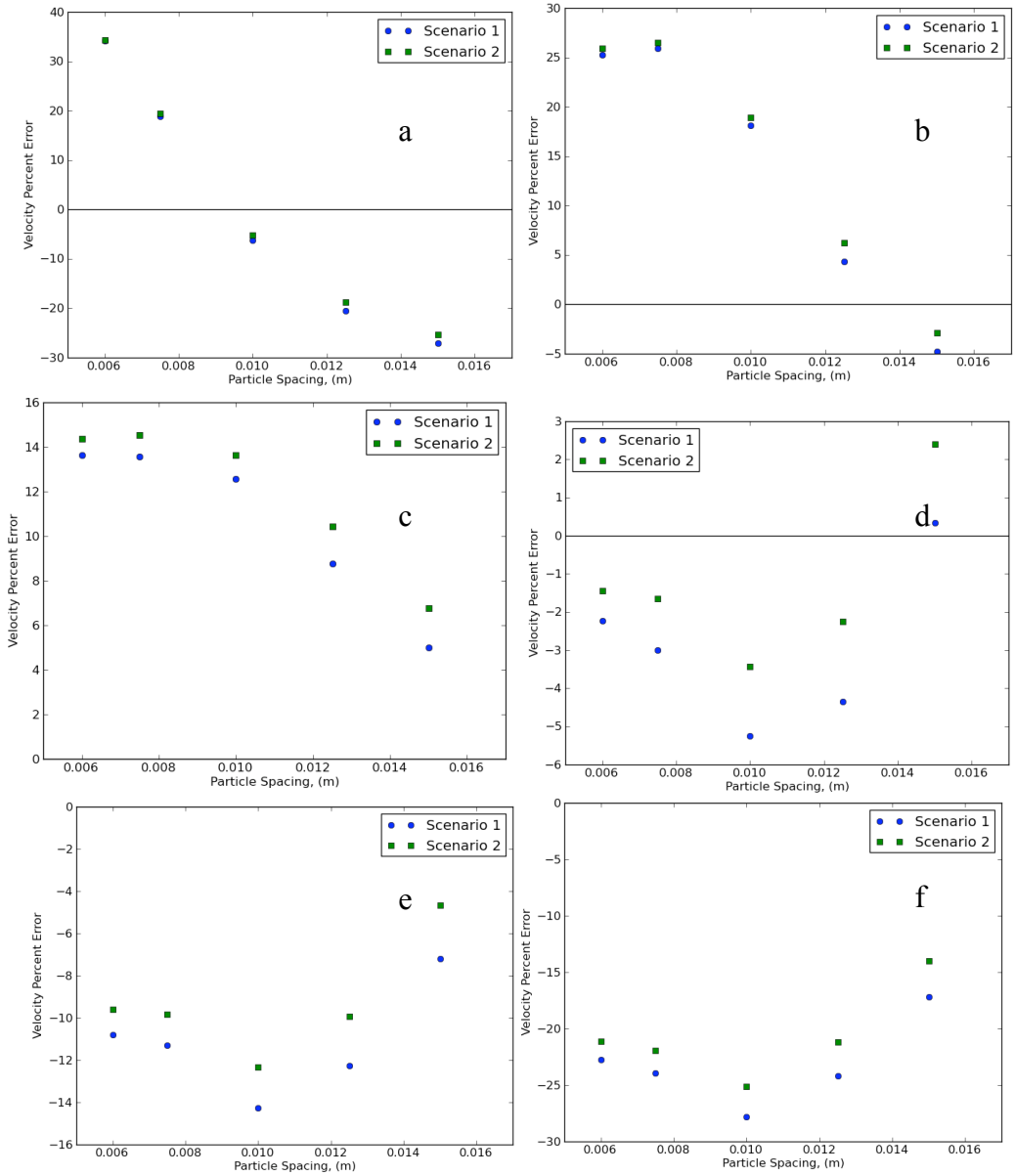

Figure 52. Percent error of boundary layer velocity normalized with respect to overall velocity from profile points at heights of (a) 8.08 mm, (b) 14.14 mm, (c) 19.19 mm, (d) 29.80 mm, (e) 35.86 mm, and (f) 45.96 mm from the bottom for Scenarios 1 and 2 using quadratic kernel and including or excluding the SPS turbulence term, respectively

Table 35. Normalized velocity values and percent errors for profile points for Scenario 2

Scenario 2 (Quadratic Kernel, No SPS term)					
Point A: 8.08 mm height			Point B: 14.14 mm height		
Particle Spacing (m)	Normalized Velocity	Percent Error	Particle Spacing (m)	Normalized Velocity	Percent Error
6.0×10^{-3}	1.26	34.33	6.0×10^{-3}	1.24	25.90
7.5×10^{-3}	1.12	19.39	7.5×10^{-3}	1.25	26.53
1.00×10^{-2}	0.89	-5.27	1.00×10^{-2}	1.17	18.93
1.25×10^{-2}	0.76	-18.78	1.25×10^{-2}	1.05	6.23
1.50×10^{-2}	0.70	-25.28	1.50×10^{-2}	0.96	-2.86
Point C: 19.19 mm height			Point D: 29.80 mm height		
Particle Spacing (m)	Normalized Velocity	Percent Error	Particle Spacing (m)	Normalized Velocity	Percent Error
6.0×10^{-3}	1.17	14.37	6.0×10^{-3}	1.01	-1.44
7.5×10^{-3}	1.17	14.54	7.5×10^{-3}	1.01	-1.65
1.00×10^{-2}	1.16	13.63	1.00×10^{-2}	0.99	-3.42
1.25×10^{-2}	1.13	10.43	1.25×10^{-2}	1.00	-2.25
1.50×10^{-2}	1.09	6.75	1.50×10^{-2}	1.05	2.41
Point E: 35.86 mm height			Point F: 45.96 mm height		
Particle Spacing (m)	Normalized Velocity	Percent Error	Particle Spacing (m)	Normalized Velocity	Percent Error
6.0×10^{-3}	0.92	-9.59	6.0×10^{-3}	0.78	-21.10
7.5×10^{-3}	0.92	-9.84	7.5×10^{-3}	0.77	-21.95
1.00×10^{-2}	0.90	-12.35	1.00×10^{-2}	0.74	-25.14
1.25×10^{-2}	0.92	-9.93	1.25×10^{-2}	0.77	-21.20
1.50×10^{-2}	0.97	-4.66	1.50×10^{-2}	0.85	-13.98

Figure 52 and Table 35 shows these same normalized velocity percent error plots for each boundary layer profile point for Scenarios 1 and 2. The plots show that the differences in percent error between Scenarios 1 and 2 are larger with increasing particle spacing and with increasing distance from the bed. Except for the 6.0×10^{-3}-m particle spacing at boundary layer point A, the Scenario 1 results are always less than the

Scenario 2 results. As discussed in the analysis for the Scenario 1 results, the data at boundary layer point A is more an indication of the effects of the kernel extending outside the flume than an indication of the actual velocity at these points. The percent error differences at boundary layer point B are largest at the largest two particle spacings with values of 1.9% for both. The difference is smallest at 6.0×10^{-3}-m and 7.5×10^{-3}-m particle spacing cases with values of 0.6%. This trend also appears in the results for boundary layer point C, with difference values of 0.7%, 1.0%, 1.1%, 1.7%, and 1.7% for particle spacings 6.0×10^{-3}-m, 7.5×10^{-3}-m, 1.00×10^{-2}-m, 1.25×10^{-2}-m, and 1.50×10^{-2}-m, respectively. The variation in these values is not as large as the variation in the values for boundary layer point B. For boundary layer points D, E, and F, the percent error difference is smallest at the smallest particle spacing and increases as the particle spacing increases. The ranges of velocity percent error difference for boundary layer points D, E, and F are 0.8% to 2.1%, 1.2% to 2.5%, and 1.7% to 3.2%, respectively. These results further verify the conclusions found from the overall flow analysis that the inclusion of the SPS turbulence term has a greater effect at larger particle spacings.

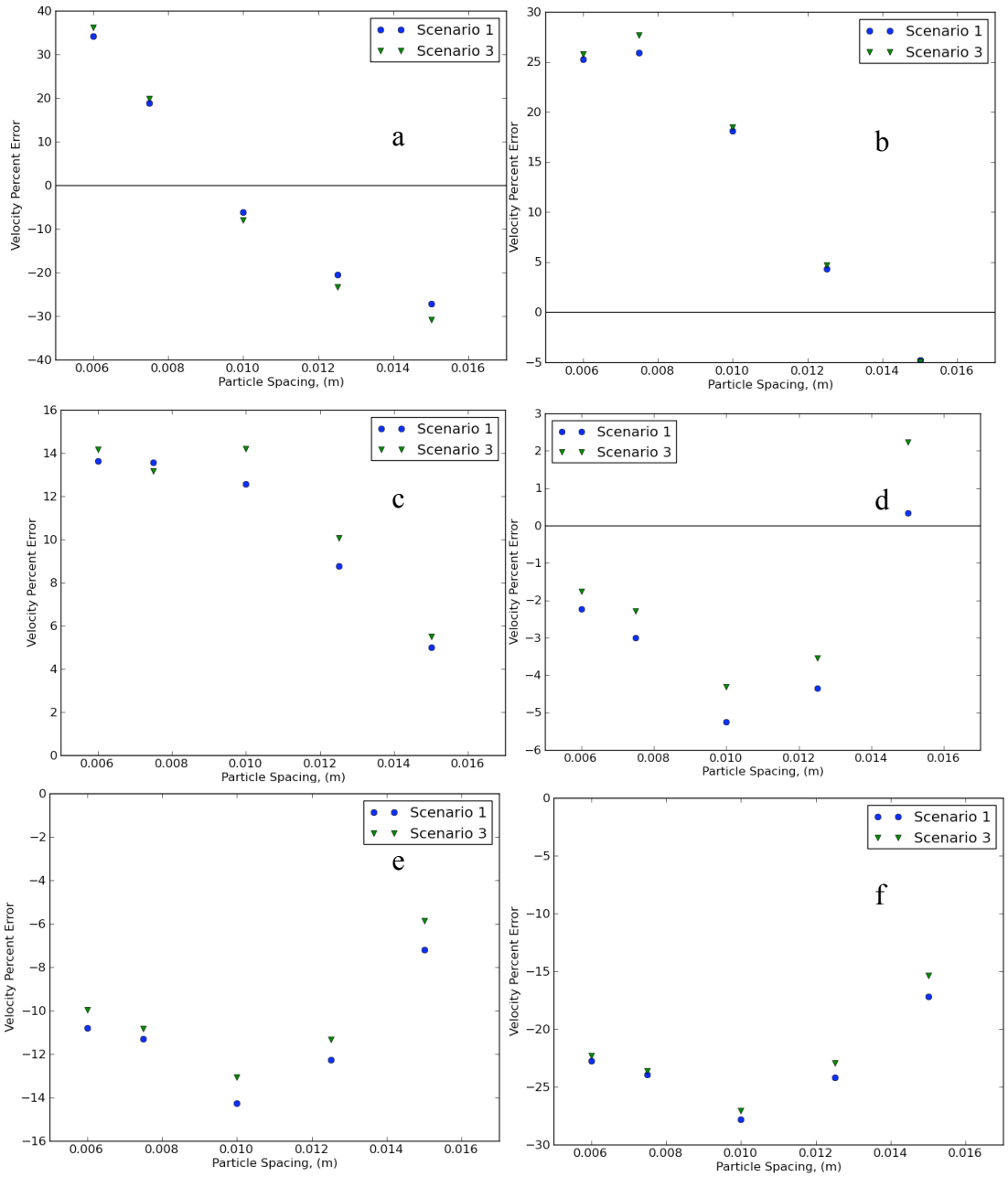

Figure 53. Percent error of boundary layer velocity normalized with respect to overall velocity from profile points at heights of (a) 8.08 mm, (b) 14.14 mm, (c) 19.19 mm, (d) 29.80 mm, (e) 35.86 mm, and (f) 45.96 mm from the bottom for Scenarios 1 and 3

Table 36. Normalized velocity values and percent errors for profile points for Scenario 3

Scenario 3 (Cubic Spline Kernel, SPS term)					
Point A: 8.08 mm height			Point B: 14.14 mm height		
Particle Spacing (m)	Normalized Velocity	Percent Error	Particle Spacing (m)	Normalized Velocity	Percent Error
6.0×10^{-3}	1.28	36.18	6.0×10^{-3}	1.24	25.80
7.5×10^{-3}	1.12	19.88	7.5×10^{-3}	1.26	27.65
1.00×10^{-2}	0.86	-8.03	1.00×10^{-2}	1.17	18.45
1.25×10^{-2}	0.72	-23.33	1.25×10^{-2}	1.03	4.70
1.50×10^{-2}	0.65	-30.81	1.50×10^{-2}	0.94	-4.91
Point C: 19.19 mm height			Point D: 29.80 mm height		
Particle Spacing (m)	Normalized Velocity	Percent Error	Particle Spacing (m)	Normalized Velocity	Percent Error
6.0×10^{-3}	1.17	14.17	6.0×10^{-3}	1.01	-1.76
7.5×10^{-3}	1.16	13.16	7.5×10^{-3}	1.00	-2.29
1.00×10^{-2}	1.17	14.40	1.00×10^{-2}	0.98	-4.31
1.25×10^{-2}	1.12	10.07	1.25×10^{-2}	0.99	-3.55
1.50×10^{-2}	1.08	5.49	1.50×10^{-2}	1.05	2.23
Point E: 35.86 mm height			Point F: 45.96 mm height		
Particle Spacing (m)	Normalized Velocity	Percent Error	Particle Spacing (m)	Normalized Velocity	Percent Error
6.0×10^{-3}	0.92	-9.98	6.0×10^{-3}	0.76	-22.29
7.5×10^{-3}	0.91	-10.84	7.5×10^{-3}	0.75	-23.61
1.00×10^{-2}	0.89	-13.07	1.00×10^{-2}	0.72	-27.05
1.25×10^{-2}	0.91	-11.32	1.25×10^{-2}	0.76	-22.96
1.50×10^{-2}	0.96	-5.86	1.50×10^{-2}	0.83	-15.38

Figure 53 and Table 36 shows the normalized velocity percent error analysis for Scenarios 1 and 3. Except for the three largest particle spacings at boundary layer point A, the Scenario 1 results are less than the Scenario 3 results. For these three cases, the magnitudes of the difference in normalized velocity is large compared to the magnitudes of this difference in the other cases, with values of 1.8%, 2.8%, and 3.7%. These values

can be compared to the other differences that are all under 1.5%, except for three cases that have 1.6%, 1.7%, and 1.8% differences. These last three cases occur at various points in the data for various particle spacings and do not show any trend. The shape of the kernel weighting function and the proximity of boundary layer point A to the bottom of the flume can explain why the three cases at this point have larger differences in the results. As noted earlier, the kernel functions for these cases extend outside the bottom of the tank, meaning the particle have fewer inputs to contribute to their velocity values. The shape of the cubic spline function in Scenario 3 places more emphasis on outer values in this kernel than the quadratic function used in Scenario 1. This means that, for Scenario 3, the values the kernel uses within the flume have a smaller weighting than these same values used in the quadratic kernel.

The lack of large differences elsewhere in the data further agrees with the finding that the kernel function does not have much influence in the results for DamBreak 2 because except for when the bore initially reaches the measurement point, the velocities tend not to varying significantly in space or time. The means that the shape of the kernel function chosen is not significant since the numbers that are averaged will be around the same value throughout the kernel.

The DamBreak 2 case shows that for both the 0.10-m and 0.15-m initial higher free-surface elevation cases, the trend of accuracy with particle spacing is greatly affected by initial placement of the particles in the system. Due to the constraints of having distinct rows of particles at initiation due to the particle spacing, it is difficult to accurately place the initial free-surface elevations, particularly the lower free-surface

elevation. These difficulties can cause inaccurate numerical free-surface elevations that can affect the quantities calculated in the model. Additionally affecting the results with respect to particle spacing is the numerical error due to rounding in the single precision calculations. This is evident in the most resolute cases for both initial free-surface elevations as the velocity values tend to be more erroneous than their slightly less resolute counterparts.

It is difficult to make any clear conclusions due to the boundary layer velocity point analyses. The most accurate particle spacing varies with distance from the bed and may be an indication that it is difficult to resolve accurate boundary layer velocities because there are not enough particles in the system to capture the structure of this flow in fine enough detail.

Analysis of the influence of the SPS turbulence term for the 0.15-m initial free-surface elevation produces the same conclusion drawn from the analysis for the 0.10-m initial free-surface elevation. The differences in velocity values between Scenarios 1 and 2 are not large, but they do increase with increasing particle spacing. The Scenario 2 results are more accurate, indicating that the SPS turbulence term is creating artificial energy dissipating turbulence throughout the length of the flume. Again, the 0.15-m initial free-surface elevation also found that the kernel function chosen has little to no effect on the results.

4.4 Time Required for Simulations

While no times were officially recorded regarding the time required to run the model, it was extremely noticeable that simulations with smaller particle spacings required more time to complete than simulations with larger particle spacings. Additionally, Scenario 2 simulations without the SPS turbulence term completed much more quickly than Scenario 1 and 3 simulations with the SPS turbulence term. Scenarios 1 and 3, which varied the kernel function calculation, had no noticeable difference in completion times. These relative completion times may be important when choosing between different particle spacings that are expected to give similar results.

4.5 Summary of Results

The results from the DamBreak 1 case included a comparison of the numerical results to the experimental velocity and force results. The comparison to the experimental velocity results showed that, for peak velocity, the best results occurred for particle spacings 3.5×10^{-3}-m and 7×10^{-3}-m to 8×10^{-3}-m and, for velocity trend, all cases with particle spacings less than 1.0×10^{-2}-m were within acceptable limits. The SPS turbulence term did not have much influence on the velocity results, but the cubic spline kernel implementation produced more variable results with respect to particle spacing than the quadratic kernel implementation.

The experimental force results comparison showed that the particle spacing cases with the most accurate results occurred between particle spacing cases 9×10^{-3}-m and 1.7×10^{-2}-m. Again, the SPS turbulence term did not have a significant influence on the

results because at the location and time of testing, the flow had not yet experienced much turbulent action. Similar to the velocity results, the cubic spline implementation had more erratic results with respect to particle spacing than the quadratic kernel results.

In addition to comparing the numerical results to the experimental results, the velocity in the area between the sidewall and the obstruction showed that there is a linear trend of increasing maximum velocity with smaller particle spacing. Also, the time difference between when the maximum velocity flow in the forward direction reached the point the time that the maximum velocity flow in the reverse direction reached the point was calculated. This time difference was significantly less for smaller particle spacings. Also, the influence of the SPS turbulence term becomes apparent in the time difference comparison by providing relatively more accurate results for the Scenario 1 case with the SPS turbulence term than the Scenario 2 case without the SPS turbulence term. Again, the cubic spline kernel implementation has more erratic results than the quadratic kernel implementation results.

The plan and three-dimensional views of the three scenarios for the 9×10^{-3}-m particle spacing case and three time steps further confirm that the influence of the SPS turbulence term primarily becomes apparent after the fluid flows past the obstruction and encounters large scale turbulence. The figures show that the cubic spline kernel implementation tends to blend neighboring velocity values more that the quadratic kernel implementation blends these values.

The DamBreak 2 implementation compared the numerical velocity results to the experimental velocity results for both the 0.10-m and 0.15-m initial free-surface

elevation cases. In both cases, the results show that the particle spacing significantly affects the accuracy of the velocity calculations. Much of this influence can be attributed to how the particle spacing contributes to the initial placement of the particles regarding the free-surface elevation due to the model creating a distinct number of particle layers separated by the particle spacing. Additionally, the SPS turbulence term has more influence in the velocity calculation at larger particle spacings, as expected. Also, the kernel function chosen did not have significant influences on the findings.

The boundary layer velocities in the 0.15-m initial free-surface elevation case were compared to the experimental values. No clear conclusions were able to be made based on the boundary values because of the influence of the boundary particle forces and the velocity calculation being influenced by the lack of particles within the kernel function but outside the boundary layer.

5. CONCLUSIONS

5.1 Conclusions for Particle Spacing

The analysis of the DamBreak 1 cases shows that there is a significant impact of particle spacing on the accuracy of the results. This effect is not linear, but instead often shows that the most accurate cases are neither the most resolute nor the least resolute cases. Most often, particle spacings in the range of 8×10^{-3}-m to 1.1×10^{-2}-m produce the most accurate results. For velocity analyses, the most accurate results tend to be in the range of 6×10^{-3}-m to 9×10^{-3}-m and for the force analyses, the most accurate results tend to be in the slightly higher range of 8×10^{-3}-m to 1.2×10^{-2}-m. The exact ranges of most accurate particle spacings vary with the type of analysis completed.

When the lowest particle spacings are erroneous, it tends to be an impact of the single precision calculations on the GPU used for this project. Single precision machines can only keep numbers to a certain decimal place and must round any number more precise than that decimal place. Under normal circumstances, this rounding will not significantly affect the output, but there are millions of particles in the most resolute cases that compound the effect of these errors. These compounded errors tend to produce significant errors in the most resolute cases that are noticeable in the results.

The most resolute cases may also be erroneous due to small radius of the kernel weighting function. For the cases discussed in this thesis, the radius of the kernel weighting function was 2.6 times the particle spacing, where as the physical influence on

a specific particle may come from a larger distance away. Future research may indicate if the kernel radius is a significant influence on the results or possibly instituting a minimum kernel radius.

Higher particle spacings also tend to be erroneous, but for a different reason than the lower particle spacings. Simulations with greater particle spacings often do not have enough particles in the system to accurately capture the flow characteristics. As expected, this error in simulation will produce results containing errored data as can be seen throughout this analysis.

The particle spacing analysis in DamBreak 2 shows the same similar trend of a middle particle spacing having the most accurate results. This similar trend is also due to the factors just discussed, but it is also influenced by the geometry of this setup. Unlike DamBreak 1, the experiment used to model DamBreak 2 had a specified initial lower free-surface elevation. Additionally, the initial higher free-surface elevation was 2.6 to 4 times smaller than the initial higher free-surface elevation in DamBreak 1. The relatively shallow water in DamBreak 2 was difficult to accurately portray using the particle spacings numerically available for the much larger flume. As seen in the analysis the difficulty in modeling the correct free-surface elevations contributed to the inaccuracies of the larger particle spacings.

Based on the conclusions found in both DamBreak 1 and 2, it is recommended to use a particle spacing in the mid-range of the GPU's capabilities if working with a single precision system. This is generally a spacing that implements particles in the range of the high hundred thousands to low millions. Ideally, this particle spacing range will

produce accurate results in an optimal amount of computing time. Double precision GPU may not experience the same issues for the higher resolution cases as outlined in this thesis and cannot be accounted for in this analysis. If this study were to be repeated on double-precision hardware, the most resolute cases are expected to produce significantly different results.

5.2 Conclusions for Inclusion of SPS Turbulence Term

The analysis for the DamBreak 1 case found that the SPS turbulence term has little to no effect on the results when there is not yet large-scale turbulence in the system, as evidenced by the comparisons between the numerical and experimental data. This statement is expected since if there is no turbulence in the system, there should be little to no sub-particle scale turbulence to resolve. The influence of the SPS turbulence term became apparent after the fluid flowed around the obstruction and interacted with the back wall. Velocity images of the data showed distinct whirlpool turbulence structures that were much more evident in the cases with the SPS turbulence term. Additionally, the overall fluid velocity after these structures were formed indicated that the sub-grid scale turbulence in Scenario 1 dissipated energy that was not dissipated in Scenario 2.

The DamBreak 2 results with respect to the SPS turbulence term validate the results for the DamBreak 1 case concerning the flow before large-scale turbulence is introduced. The DamBreak 2 results showed that the SPS turbulence term had little impact on the numerical results because the overall flow did not produce large turbulent structures such as the whirlpools in DamBreak 1. The little influence the SPS turbulence

term did have was most apparent in the larger particle spacings, but produced more erroneous results than the cases without the SPS turbulence term. The errors of these results indicate that the SPS turbulence term may be introducing artificial turbulence in the velocity bore that dissipates the energy and slows the overall flow. This artificial turbulence in the bore was not present in the DamBreak 1 case because the simulation did not have as long of a flume to travel as in the DamBreak 2 case. Based on these results, the SPS turbulence term formulation is accurate, especially for setups that include larger scale turbulence. The drawback of introducing artificial turbulence in relatively turbulent-free flows is comparatively minor to the accurate influence of the term in turbulent flows.

While there are no recorded computational times required to complete the simulations, the cases including the SPS turbulence term took significantly longer to complete than the cases without the SPS turbulence term. In order to produce the most accurate results in the optimal amount of time, it is recommended that the SPS turbulence term be included if turbulence is expected due to the geometry of the system. If turbulence is not expected, it is recommended to ignore the SPS turbulence term to avoid the creation of artificial turbulence and save computational time.

5.3 Conclusions for Kernel Weighting Function

In DamBreak 1, the results of the cases using the quadratic kernel for the weighting function tended to produce smoother and more predictable curves than the results for the cases using the cubic spline kernel for the weighting function when

comparing quantities with respect to particle spacing. When determining the relative accuracy of the two options for a given particle spacing, neither case was predominately correct throughout the analysis. The images of the overall flow structure of the 9 x 10^{-3}-m particle spacing case clearly show that the quadratic kernel creates more distinct boundaries between separate pockets of fluid moving at different velocities. The cubic spline function, which has a more gradually decreasing weight from the center, tends to blend the pockets of flow.

The DamBreak 2 case showed that there was almost no difference in results when comparing the quadratic kernel to the cubic spline kernel. This finding is most likely due to relative uniformity of the flow past the measurement point. If the velocities within the kernel tend to be near the same quantity, the kernel function chosen will not make a difference in the result.

As stated above, the time required to complete these simulations was not recorded, but there was no noticeable difference in time required for completion between these two kernel functions. Additionally, there is no clear indication that either kernel function is better suited for this type of free-surface flow. Because of these conclusions, there is no recommendation concerning the two kernel functions.

5.4 Overall Conclusions and Suggestions for Future Research to Validate GPUSPH

GPUSPH is a viable option to model coastal vegetation fields based on the results of this thesis. Of the three factors studied, particle spacing, SPS turbulence term inclusion, and kernel function, the particle spacing had the most influence on the

accuracy of the results. If the correct particle spacing is chosen based on the size of the setup and available hardware, the results of the numerical study can accurately calculate real-world physical quantities. For a vegetation field, which is expected to produce many turbulent structures, the SPS turbulence term should be included in the implementation to produce more accurate results.

This project is intended to verify and validate the GPUSPH model. While the results discussed in this thesis show that the model can produce accurate data, research is continually needed to improve this and other numerical models. Some suggestions for further research are:

- Analyze the accuracy and impacts of the boundary forces in GPUSPH
- Vary the weighting kernel radius for smaller particle spacings
- Complete some of these analyses on double precision GPU
- Study a case that allows for a flume long enough to create eddies off of an obstruction
- Introduce multiple obstructions into the system

While this study explored fluid flow in a basic flume and around one obstruction, further work on the validation of GPUSPH should produce promising results to further confirm the code's ability to model complicated flow structures through the vegetation. This future work will probably have the ability to prove that GPUSPH can accurately calculate the vegetation's influence on the dissipation of water currents and waves in coastal areas.

REFERENCES

Arnason, H., C. Petroff, and H. Yeh (2009), Tsunami bore impingement onto a vertical column, *Journal of Disaster Research*, *4*(6), 391-403.

Cox, D. T., and J. A. Ortega (2002), Laboratory observations of green water overtopping a fixed deck, *Ocean Engineering*, *29*(14), 1827-1840.

Crespo, A. J. C., M. Gomez-Gesteira, and R. A. Dalrymple (2008), Modeling dam break behavior over a wet bed by a SPH technique, *Journal of Waterway Port Coastal and Ocean Engineering-Asce*, *134*(6), 313-320.

Dalrymple, R. A., and B. D. Rogers (2006), Numerical modeling of water waves with the SPH method, *Coastal Engineering*, *53*(2-3), 141-147.

De Leffe, M., D. Le Touze, and B. Alessandrini (2010), SPH modeling of shallow-water coastal flows, *Journal of Hydraulic Research*, *48*, 118-125.

Gingold, R. A., and J. J. Monaghan (1977), Smoothed particle hydrodynamics: Theory and application to non-spherical stars, *Monthly Notices of the Royal Astronomical Society*, *181*(2), 375-389.

Gomez-Gesteira, M., and R. A. Dalrymple (2004), Using a three-dimensional smoothed particle hydrodynamics method for wave impact on a tall structure, *Journal of Waterway, Port, Coastal, and Ocean Engineering*, *130*, 63-69.

Gomez-Gesteira, M., D. Cerqueiroa, C. Crespoa, and R. A. Dalrymple (2005), Green water overtopping analyzed with a SPH model, *Ocean Engineering*, *32*(2), 223-238.

Gomez-Gesteira, M., B. D. Rogers, R. A. Dalrymple, A. J. C. Crespo, M. Narayanaswamy (2010), *User Guide for the SPHysics Code v2.0*, http://www.sphysics.org

Harada, T., S. Koshizuka, and Y. Kawaguchi (2007), Smoothed particle hydrodynamics on GPUs, *Proc. Comput. Graph. Intl.*, 63-70.

Herault, A., G. Bilotta, and R. A. Dalrymple (2010), SPH on GPU with CUDA, *Journal of Hydraulic Research*, *48*(Special Issue), 74-79.

Herault, A., G. Bilotta, and R. A. Dalrymple (2011), *GPUSPH Users Manual*. http://www.ce.jhu.edu/dalrymple/GPU/GPUSPH/Home.html

Hughes, J. P., and D. I. Graham (2010), Comparison of incompressible and weakly-compressible SPH models for free-surface water flows, *Journal of Hydraulic Research*, *48*(Special Issue), 105-117.

Kirk, D., and W. Hwu (2010), *Programming Massively Parallel Processors: A Hands-on Approach*, Morgan Kauffmann Publishers, Burlington, MA.

Kundu, P. K., and I. M. Cohen (2008), *Fluid Mechanics*, 4th ed., Elsevier Inc., Burlington, MA.

Liu, M. B., and G. R. Liu (2010), Smoothed particle hydrodynamics (SPH): An overview and recent developments, *Archives of Computational Methods in Engineering*, *17*(1), 25-76.

McCarn, D. W., and J. R. Carr (1992), Influence of numerical precision and equation solution algorithm on computation of kriging weights, *Computers & Geosciences*, *18*(9), 1127-1167.

Monaghan, J. (1994), Simulating free-surface flows with SPH, *Journal of Computational Physics*, *110*, 399-399.

Monaghan, J. J., and J. B. Kajtar (2009), SPH particle boundary forces for arbitrary boundaries, *Computer Physics Communications*, *180*(10), 1811-1820.

NVIDIA (2010), *Tesla C1060 datasheet*, NVIDIA Corporation, Santa Clara, CA.

Pope, S. B. (2010), *Turbulent Flows*, 7th ed., Cambridge University Press, New York.

Raad, P. Mitigation of Local Tsunami Effects, edited <http://lyle.smu.edu/waves/mitigation.html>, Accessed 26 January 2011.

Stoesser, T., G. P. Salvador, W. Rodi, and P. Diplas (2009), Large eddy simulation of turbulent flow through submerged vegetation, *Transport in Porous Media*, *78*(3), 347-365.

Vaughan, G. L. (2009), The SPH equations for fluids, *International Journal for Numerical Methods in Engineering*, *79*(11), 1392-1418.

APPENDIX A

COMPARISON OF NEWER AND OLDER VERSIONS OF GPUSPH

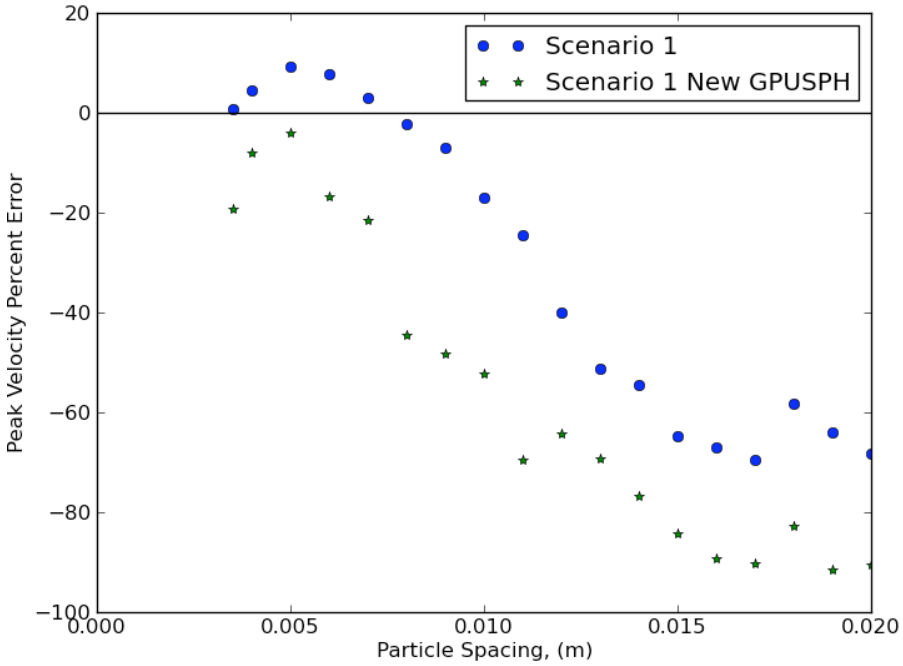

Peak velocity percent error versus particle spacing for Scenario 1 in newer and older versions of GPUSPH

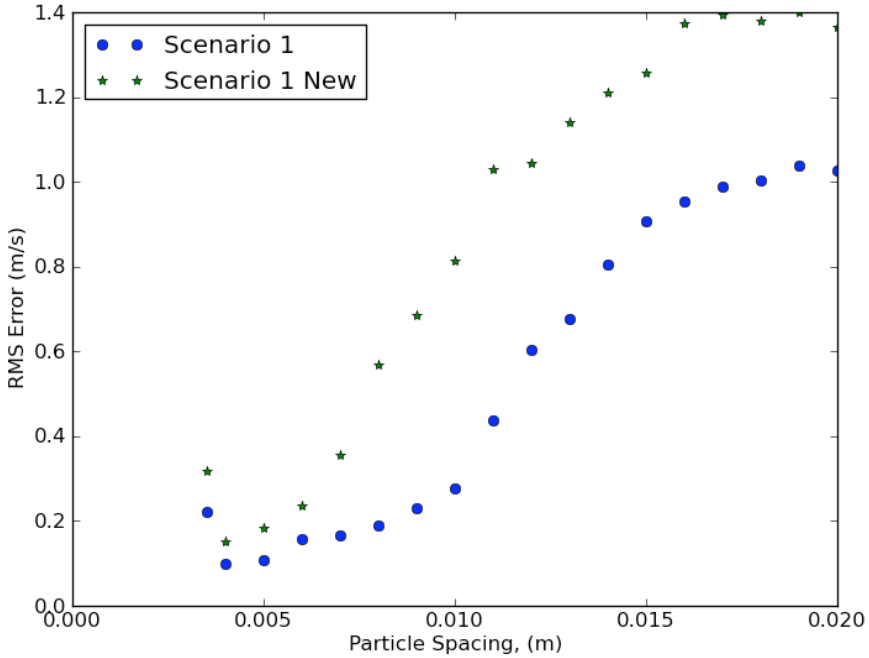

RMS analysis error of velocity versus particle spacing for Scenario 1 in newer and older versions of GPUSPH

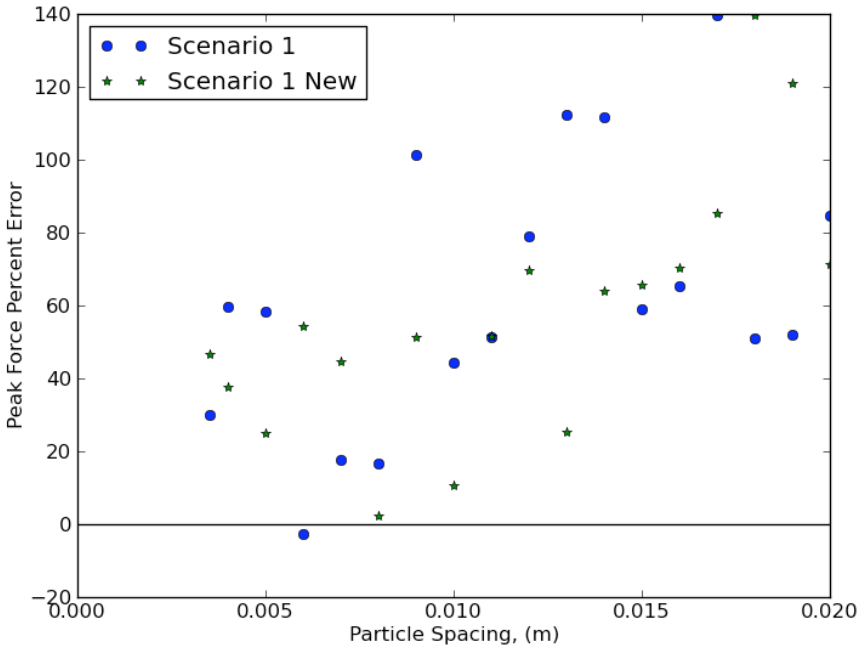

Peak force at the obstruction percent error versus particle spacing for Scenario 1 in newer and older versions of GPUSPH

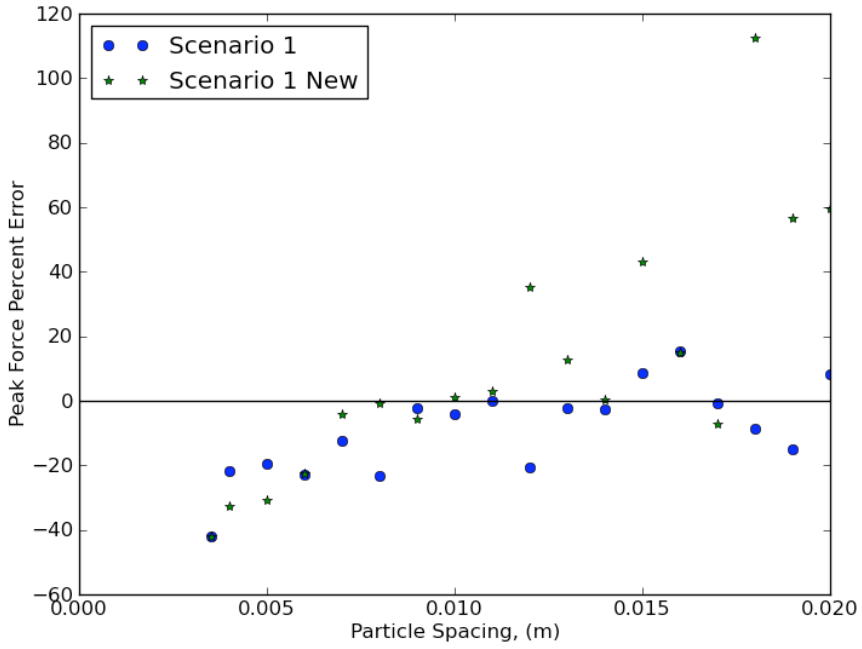

Peak force 0.06 m away from the obstruction percent error versus particle spacing for Scenario 1 in newer and older versions of GPUSPH

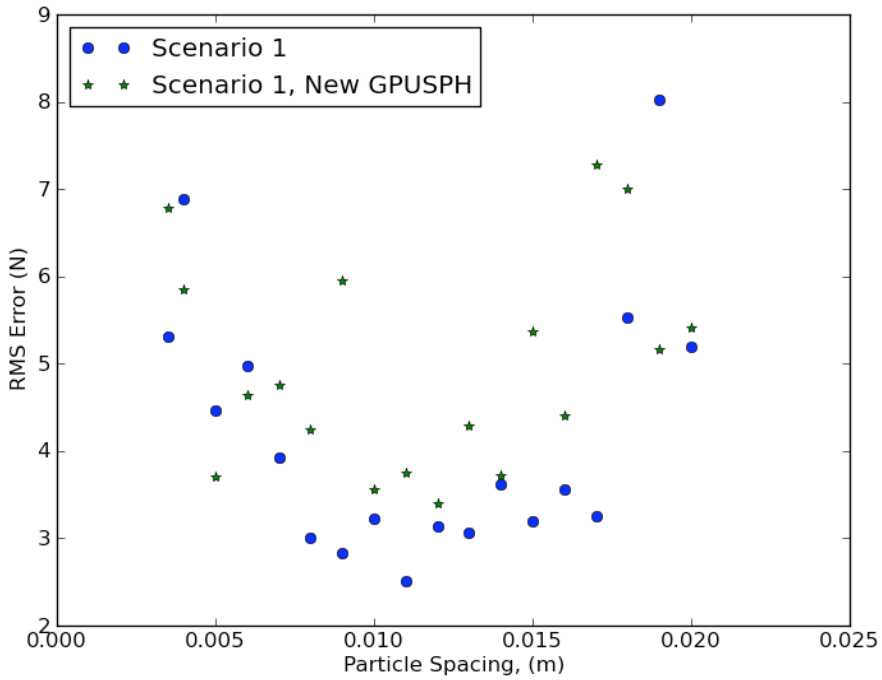

RMS analysis error of numerical force results versus particle spacing for Scenario 1 in newer and older versions of GPUSPH

VITA

Name: Erin Ann Rooney

Email Address: erin.ann.rooney@gmail.com

Mailing Address: Department of Civil Engineering
Ocean Engineering Program
c/o Dr. Jennifer Irish
3136 TAMU
College Station, TX 77843-3136

Education: B.S., Civil Engineering, Virginia Polytechnic Institute and State University, 2009

M.S., Civil Engineering, Texas A&M University, 2011